7-11-2022

Analysis of growth and decay in neutrally stable flows

Colin Huber
cmh7271@rit.edu

Analysis of growth and decay in neutrally stable flows

by

Colin Huber

A Dissertation Submitted in Partial Fulfillment of the Requirements

for a PhD in Mathematical Modeling

School of Mathematical Sciences,

College of Science

Rochester Institute of Technology

Rochester, NY

July 11, 2022

Committee Approval:

R·I·T
College of
Science

Steve Weinstein, PhD Date

School of Mathematical Sciences and Kate

Gleason College of Engineering

Rochester Institute of Technology

Thesis Advisor

Nate Barlow, PhD Date

School of Mathematical Sciences

Rochester Institute of Technology

Thesis Advisor

Michael Schertzer, PhD Date

Kate Gleason College of Engineering

Rochester Institute of Technology

Committee Chair

Kara Maki, PhD Date

School of Mathematical Sciences

Rochester Institute of Technology

Committee Member

Brian Helenbrook, PhD Date

Coulter School of Engineering

Clarkson University

Committee Member

Nathan Cahill, PhD Date

School of Mathematical Sciences

Rochester Institute of Technology

Director of Graduate Program

Abstract

The stability of linearized partial differential equations (PDEs) governing disturbance propagation in a one-dimensional medium, such as a perturbed fluid-fluid interface, is traditionally deduced by examining the growth of exponential modes of the form $h_k = A_k e^{i(kx-\omega t)}$*, where* h_k *is a mode associated with the height of the perturbed interface,* A_k *is its amplitude,* k *is a real wave number,* ω *is a complex frequency,* x *is the spatial direction, and* t *is time. It is assumed that these modes may be superimposed to construct the solution,* h*, to any response, and thus, if any of these modes grow in time, the operator admits growing solutions, i.e. unstable. In previous work, King et al. (Stability of algebraically unstable dispersive flows, Phys. Rev. Fluids, 1(073604), 2016) report the breakdown in this stability classification when* $Im[\omega] = 0$ *for all* k *values. While this result classically indicates that solution responses neither grow nor decay in time, King et al. find, instead, that responses grow algebraically as* $h \sim t^s$ *where* s *is a positive fractional power. This result is deduced through an asymptotic analysis of the Fourier integral that invokes the continuous superposition of an infinite number of modes. In this work, we explore — through a sequence of three related problems — the response behavior of linear operators that exhibit a similar breakdown in stability classification. First, we study the rectilinear, Newtonian, thin-film flow of a liquid down an inclined plane. In contrast to the structure of King et al, at neutral stability (based on traditional mode characterization discussed above) the operator yields a single mode having* $Im[\omega] = 0$ *for* $k = 0$*, and* $Im[\omega] < 0$ *for* $k > 0$*. As in King et al., we utilize a Fourier-Laplace approach and conclude that the response amplitude is not constant at neutral stability, and in fact decays in time as* $t^{-1/2}$ *— this is yet another breakdown in the traditional classical stability conclusion based on exponential modes. Next, two operators that demonstrate algebraic growth as* $t^{1/2}$ *in one dimension (1D) studied by King et al. (Phys. Rev. Fluids, 1, 2016, 073604:1-19) and Huber et al. (IMA J. Appl. Math., 85, 2020, 309-340) are extended to two dimensions (2D) and propagation characteristics are examined. We find that the*

increase in dimension leads to a reduction of 1D response magnitude by a factor of $t^{1/2}$ compared with the 1D cases. Thus, peaks which grew in 1D have a constant height in 2D, and regions which decay (algebraically or exponentially) do so faster in 2D. We also find that both operators admit long-time solutions that are functions of similarity variables, which contract space and time. Lastly, we examine the effect of a local oscillatory forcing on the previously examined operator studied by King et al. — this is referred to as the signaling problem. Whereas signaling has been studied with operators that admit exponential growth and decay, we examine, for the first time, the morphology of the solution response for an operator that admits algebraic growth. As in exponentially growing systems, we find that critical velocities can be determined that observably delineate the response into distinct regions. However, the response is distinctly different from exponentially growing cases, owing to the neutrally stable character of its component modes. The superposition of such modes via Fourier integral analysis reveals a rich structure having broad regions with distinct bounding amplitudes. Overall, the three problems examined provide new insights into the nature of neutral stability and the solution of PDEs under such conditions.

Acknowledgments:

I would like to thank my advisors, Dr. Steven Weinstein and Dr. Nathaniel Barlow, for their help and support over my undergraduate and graduate career at RIT. They helped inspire me to continue my studies past my bachelors degree, publish my first papers, and get through the complex math and analysis of my dissertation.

I would also like to thank my thesis committee for their thoughtful feedback on my dissertation and defence.

Furthermore, I am also thankful to the faculty and staff of the School of Mathematical Sciences for their support and for working to keep everything running smoothly, with specific thanks to current program director Dr. Nathan Cahill, former program director Dr. Elizabeth Cherry, and administrative assistant Kathleen Koch.

Finally, I would like to thank my friends and family for their support throughout the years, specifically my parents and my sister, and the current and former members of the RIT Improv Club.

Contents

Chapter I

Introduction

The ability to determine how fluid systems respond to disturbances is important to a wide variety of manufacturing processes. Whether such disturbances grow or decay when initiated — the so-called stability of the flow — is crucial to that assessment. For example, unstable fluid flows assure that droplets are formed in liquid fuel atomizers [1, 2, 3]. Alternatively, stable fluid flows are desirable in high-precision coating processes used to manufacture uniform liquid films — these are used, for example, to produce ink jet and copier paper, printed electronics, and liquid crystal display screens [4, 5]. If a system is stable, then the response to any disturbance will damp out with time, while if it is unstable, the disturbance will magnify in time. This work focuses on stability analyses relevant to thin-film coating processes. In these flows, the tight product constraints (on the order of 1%) mean that *linearized* governing equations provide accurate predictions of disturbance propagation, as the product would be rendered unsalable before the assumptions of linearization are violated [6].

In order to determine if responses to a disturbance grow or decay, classical stability analysis is utilized. Introduced originally in 1880 by Lord Rayleigh [7], classical stability analysis serves as the basis for much of the hydrodynamic literature [8, 9, 10, 11]. In order to apply the method to a linear operator, the response is expressed as an infinite sum of modes, h_k, each of the form

$$h_k(x,t) = A_k e^{i(kx-\omega t)} = A_k e^{(\omega_i t)} e^{i(kx-\omega_r)t}. \tag{I.1}$$

In (I.1), A_k is the amplitude of the mode as a function of wave number, k is the real wave number, ω_r is the real and ω_i the imaginary part of the complex frequency $\omega(k)$, x is the spatial direction, and t is time.

In the superposition of exponential modes used to construct any disturbance, the fastest growing (or slowest decaying) mode, defined by $\omega_{i,\max} \equiv \max(\mathrm{Im}[\omega(k)])$, will dominate the overall response as time goes to infinity as

$$h_{\max} \sim A_{\max} e^{\omega_{i\max} t} \quad \text{as} \quad t \to \infty, \tag{I.2}$$

where $A_{\max}$ is the A_k for the relevant mode. In (I.2), the sign of $\omega_{i,\max}$ is used to determine the stability for a given set of conditions as follows [8, 12, 9]:

$$\omega_{i,\max} < 0: \quad \text{The system is stable,} \tag{I.3a}$$

$$\omega_{i,\max} = 0: \quad \text{The system is neutrally stable,} \tag{I.3b}$$

$$\omega_{i,\max} > 0: \quad \text{The system is unstable.} \tag{I.3c}$$

According to this classification, if $\omega_{i,\max} > 0$ the response to an arbitrary disturbance will grow exponentially in time, and if $\omega_{i,\max} < 0$, the response will decay exponentially in time. The method indicates that if $\omega_{i,\max} = 0$ the response will neither grow nor decay.

This is not, however, always the case. In the case of water waves, all values of ω_i are zero, and disturbances *decay* algebraically as $t^{-1/2}$ [13, 14]. In King et al. [15], an operator that governs varicose perturbations in a curtain flow is analyzed and is shown to permit solutions that *grow* algebraically as $t^{1/2}$, despite all values of ω_i being zero. As such, additional linear stability methodology is needed to supplement the classical theory to allow one to accurately determine the behavior of neutrally stable flows.

The objective of this research is to provide case studies of neutrally stable flows where classical stability analysis breaks down. While not intended to be an exhaustive study, the goal is to examine the representative behavior of various simplified operators. These operators, although simple in nature, allow us to draw conclusions in an accessible way which rounds out our understanding of neutral stability. Below is a table (Table I.1) of the operators examined in this thesis. Each operator contains the minimum structure needed to explore aspects of neutral stability not disclosed before, as summarized in Table I.2. In this regard, they may be considered benchmark problems.

Table I.1: Operators at neutral stability

Operator name	Previous area of study	New area of study
1D-Inc. plane flow	N/A	Stability and response
1D-Signaling	Stability and response to initial disturbance	Response to oscillatory disturbance
2D-KRK	1D stability and response	2D stability and response
2D-CMH	1D stability and response	2D stability and response

Table I.2: Summary of operators examined

Operator name	Equation	Original source	Included in	Description
1D-Inc. plane flow	Equation II.6	From Section 4 of [16]	Chapter II	One mode neutrally stable, all others damped
1D-Signaling	Equation III.8	Adapted from [15]	Chapter III	All modes neutrally stable
2D-KRK	Equation IV.4	Adapted from [15]	Section IV.2	All modes Neutrally stable
2D-CMH	Equation IV.22	Adapted from Section 3 of [16]	Section IV.3	One mode neurally stable, all others damped

In what follows, Chapter II provides a model for thin-film flow down an inclined plane under conditions of neutral stability. This work was published in the IMA Journal of Applied Mathematics [16] and is reproduced here with permission. The one-dimensional operator from King et al. [15] is examined in Chapter III with the addition of an oscillatory forcing function to — for the first time — examine the so-called "signaling problem" at neutral stability. The problem demonstrates how the response to forcing, which persists for all time, evolves through the passage of a transient wave response. The contents of Chapter III are in preparation for submission. In Chapter IV, we take two one-dimensional linear operators that exhibit growth/decay at neutral stability, previously examined by King et al. [15] and Huber et al. [16], and extend them to higher spatial dimensions, in order to show — for the first time — the effect of dimensionality on algebraic instability. Chapter IV is replicated from the manuscript that has been submitted for publication [17]. Chapter V presents the overall conclusions of the research. Note that, since Chapters II-IV are kept in the form of prepared journal manuscripts, each chapter is intended to stand alone. As such, there is some repetition of introductory material in these chapters.

Chapter II

On the stability of waves in classically neutral flows

This section was taken directly from the publication "On the stability of waves in classically neutral flows" [16] with the exception of adjustments to the flow and references.

II.1. Introduction

The current work is motivated by the need to characterize fluid flows involved in the manufacture of a variety of products. All flow processes are subjected to time-varying disturbances induced from their surroundings, while product quality typically necessitates the requirement of time invariance. In particular, each product has a manufacturing tolerance to perturbations that requires accurate characterization. Mathematical models that relate disturbances to system responses are commonly used in industry to enable

guided experiments, and once validated, can be accurate enough to replace experiments. An essential feature of disturbance modeling is whether the underlying fluid system is stable or unstable, i.e. whether a response to disturbances grows or decays. If the fluid system is stable, then product specifications may be met by minimizing the magnitude of process disturbances; if the system is not, control of the process is much more complex, and in some cases, impossible. The characterization of fluid flow stability then, is motivated by practical need. Within stable fluid systems, tight product tolerances often dictate that perturbations be small and lie in a linear regime – a product often becomes unsalable well within the dictates of linearity. Thus, a corresponding linear operator may be used to model the fluid system response. The characterization of the stability of such a linear operator, then, is of paramount importance to develop sustainable operating parameters that meet product specifications.

If a flowing liquid system in a manufacturing process is unstable, i.e., initiated disturbances are magnified, the flow can often easily be disrupted away from a uniform state. This could be a desired outcome, as is the case for liquid fuel atomizers [1, 2, 3] where instability leads to the breakup of a liquid sheet into droplets, or in the case of instability-driven turbulence to enhance mixing processes [18]. Instability is unwelcome in other situations where layer uniformity is essential, such as in the thin films used to coat ink jet and copier papers, printed electronics, and liquid crystal display screens [4, 5]. Thus, it is important for practitioners to control the parameters that influence fluid instability in order to produce a salable product. The most widely used stability assessment, referred to here as classical stability theory, provides the basis for much of the hydrodynamic literature [8, 12, 9, 10, 11].

Classical stability theory is built on the following ideas. Typically, the analysis starts with a full nonlinear operator and boundary conditions, which are linearized about a base fluid flow (oftentimes exact) whose stability is to be assessed. The resulting linear partial differential equation (PDE) system may be expressed in terms of an operator, L, and flow response, $h(x,t)$, as $Lh = 0$, where x and t are respective space and time variables. Note that forcing and initial conditions are neglected when examining the PDE system, as the general homogeneous response characterizes the classical stability of the medium. A solution of this equation on an unbounded domain ($-\infty < x < \infty$) may be expressed as

$$h = Ae^{i(kx-\omega t)}, \tag{II.1}$$

where k is a real wavenumber, ω is a complex frequency, and A is an amplitude. It is assumed that the fundamental responses (II.1) for each value of k, henceforth called modes, may be superimposed to represent the flow response to any disturbance; furthermore, it is assumed that the stability of a complex flow response may be characterized by the stability of its constituent modes. Substitution of (II.1) into the linearized PDE system leads to a dispersion relation of the form

$$D(k,\omega) = 0, \quad \text{also written } \omega = \omega(k), \tag{II.2}$$

that assures a nontrivial solution of the equation $Lh = 0$. In classical stability theory, the complex-valued $\omega(k) = \omega_r(k) + i\omega_i(k)$ is examined, where the function $\omega_i(k)$ determines the exponential growth in time of a mode. The maximum growth rate over the range of $k \in (-\infty, \infty)$, denoted as $\omega_{i,\max}$, is used to characterize the stability of the flow. At large times, the exponential nature of the responses (II.1) dictate that growth rates at other

wavenumbers are subdominant, and the system thus grows as

$$h \sim Ae^{\omega_{i,\max} t} \text{ as } t \to \infty, \tag{II.3a}$$

where A is a constant. Thus, once $\omega = \omega(k)$ is established from (II.2), the linear (exponential) stability is determined as follows [8, 12, 9]:

$$\omega_{i,\max} < 0\text{: the flow is linearly stable,} \tag{II.3b}$$

$$\omega_{i,\max} > 0\text{: the flow is linearly unstable,} \tag{II.3c}$$

$$\omega_{i,\max} = 0\text{: the flow is neutrally stable.} \tag{II.3d}$$

The classification (II.3) was used by [7], and this classical stability theory has been further developed over the last 100+ years. We note here that the focus of this work lies in the context of laminar flows, such as in coating processes. In contrast to problems in which stability conclusions are affected by nonlinear perturbations to the base flow [19], such nonlinear effects are not generally relevant to precision coating operations having tight tolerances on layer uniformity; in these applications, products are typically unsalable even when responses lie within the linear regime, as stated above and in [6].

The focus of this chapter is the classification of neutral stability according to (II.3d), and is motivated by [15], henceforth referred to as KRK (the acronym for its first author). In that work, the classical stability of a fluid flow system yields modes that are neutrally stable for all values of k, i.e., $\omega_{i,\max} = 0$ for all wave numbers. While the classical stability assessment (II.3d) indicates there will be no growth or decay in a system response, KRK demonstrates both numerically and analytically that disturbances can grow algebraically. Algebraic growth is defined as a system response that obeys $h \sim Ct^s$, where C is a constant

and the exponent s is a positive rational number. It should be noted that algebraic decay of disturbances ($s < 0$) has also been identified in previous work when exponential modes are neutrally stable for all real k, having both integer [20] and non-integer [13, 14, 21] character. It is apparent that the classification of neutral stability via classical means is deficient and warrants further study.

As is evident in the work of KRK and many earlier studies [22, 23] (see KRK for a comprehensive literature review), algebraic growth in linear PDE operators may be examined via a spatio-temporal formulation involving both Fourier and Laplace transforms. When the inverse Laplace transform is taken first, the resulting Fourier inversion integral has an integrand with an exponential term identical to (II.1) with $\omega = \omega(k)$ according to the dispersion relation (II.2). As such, the connection between classical stability analysis and a spatio-temporal analysis is made — the assumption being that the growth characteristics of the superposition of modes of the form (II.1) invoked via integration mimic exactly that of the individual modes (II.1) when taken separately. In fact, KRK shows that this is not always the case. When the exponent s in $h \sim Ct^s$ is fractional, algebraic growth can only be deduced via a superposition of modes via integration, and is thus in fact non-modal. An additional important feature of systems exhibiting algebraic growth is their sensitivity to the type of perturbations to the system. KRK shows that if perturbations in initial velocity and forcing are invoked, a system response may grow algebraically; however, if the same system is perturbed in location, the system response can decay algebraically. The sensitivity to initial conditions makes it imperative to consider a broad set of perturbations to a system when establishing system stability, especially so when examining the possibility of algebraic

growth. A historical review of long-time algebraic instability is provided in [15].

KRK focuses on a breakdown in classical stability theory for a dispersion relation (II.2) in which all modes exhibit neutral stability, yet growth or decay is actually predicted. The more typical situation in which neutral stability arises in the literature is where a single mode is neutrally stable, and modes corresponding to all other real wavenumbers exhibit damping according to the form (II.1) with dispersion relation (II.2). It is widely held in prior literature [8, 24, 11, 10] that flows exist in a state that is neither stable nor unstable at a neutral stability boundary from classical theory. A question arises as to whether the breakdown in classical stability theory (II.3) reported by KRK extends to the situations shown in Figure II.1 when only one wavenumber mode is neutrally stable.

Figure II.1a is a schematic showing a scenario where this neutral stability configuration occurs (see, for example [25, 26]); here, as a parameter (B) is varied through its critical value, the flow changes from stable, to neutral, to unstable in accordance with the characterization (II.3). The features of such a transition is considered in Section 2 of [16]. Figure II.1b shows another type of transition that occurs in the well-studied stability of a single layer Newtonian fluid flowing down an inclined plane, where the critical parameter is the Reynolds number, Re, defined in Section II.2. As indicated in Figure II.1b, unstable flows for $Re > Re_c$ have a maximum modal growth rate at finite wave number, and as $Re \to Re_c$ this maximum growth rate diminishes to zero and its associated wavenumber simultaneous approaches $k = 0$. For $Re \leq Re_c$, the $k = 0$ mode is neutrally stable, and all other modes are damped — in this case, there is not a true transition from instability to stability based on a classical stability analysis, but rather a transition from instability to

neutral stability. This latter assessment has not been explored in prior literature, as it is widely accepted that when $Re < Re_c$, inclined plane flow is stable [27, 28]. It is possible that the $k = 0$ wavenumber is neglected in prior stability work because it coincides with an interfacial perturbation that is flat, and thus may be viewed as degenerate. The objective of this paper is to consider the prospect of algebraic growth and decay for the classically neutral stability configurations shown in Figures II.1a and II.1b (at $B = B_c$ and $Re = Re_c$, respectively)[1].

The chapter is organized as follows: Section II.2 introduces the well-known incline plane flow studied by [27], where it is shown that algebraic decay can occur on the threshold of neutral stability. In Section II.2, the governing PDE is derived in non-dimensional form. In Section II.3, the classical stability analysis is reviewed and key elements are extracted regarding the neutral stability threshold. In Section II.4, the integral solution is examined via asymptotic analysis and the algebraic decay rate is deduced. A summary of our results and concluding remarks are given in Section II.5.

II.2. Governing equations valid for small interfacial slope

We consider a Newtonian liquid of constant density, ρ, and constant viscosity, μ, flowing under the influence of gravity, g, along a solid surface inclined to horizontal with angle θ as shown in Figure II.2. The liquid layer is exposed to air having a constant atmospheric pressure, and the air-liquid interface has a constant surface tension, σ. Under ideal

[1]Figure II.1a is relevant to the operator in Chapter IV and Figure II.1b is relevant to Chapter II

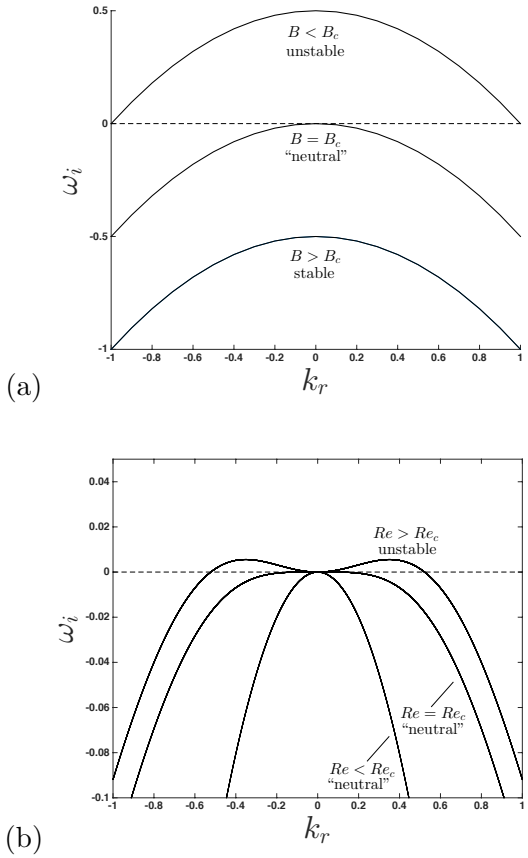

Figure II.1: Classical stability curves for two illustrative problems where transition occurs due to the variation of a critical parameter: (a) The transition from exponential growth to exponential decay for the model problem in Section 2 of [16] as the parameter B is varied. The curves (top to bottom) correspond to $B = -1$, 0, and 1, (b) The effect of Reynolds number (defined in Section II.2) on the stability transition for flow down an inclined plane. The curves (top to bottom) correspond to $Re = 1.1 \cot\theta$, $\cot\theta$, and $0.5 \cot\theta$ where (for all curves) the incline angle is $\theta = \pi/4$ and the nondimensional Weber number is 0.1.

conditions, the liquid flows with a steady-state constant thickness H_0 (Figure II.2) and constant volumetric flow rate per unit width, Q_0. The film is perturbed away from uniform due to external disturbances (to be specified later) while remaining invariant in the Z direction (out of Figure II.2, and the total film thickness deviates from H_0 in accordance with the parameterization $Y = H_0 h(X, T)$, where h is a dimensionless multiplier, Y is the distance perpendicular to the wall into the fluid domain, X is the distance down the incline, and T is time. The dynamics of the air are neglected and the external pressure remains atmospheric for all time.

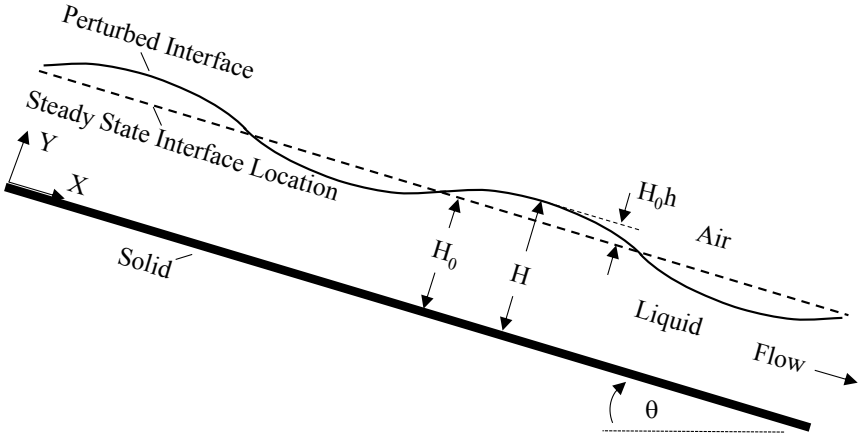

Figure II.2: Schematic of flow of a thin film along an inclined solid. The flow is invariant in the Z direction, oriented into and out of the figure. The steady state interface location is denoted as H_0, the perturbed interface location denoted as H, and the perturbation magnitude given as h, a fraction of H_0.

A set of approximate dynamical equations that govern this configuration may be developed as follows [29, 6]: it is assumed that the slope of the perturbed air-liquid interface and underlying fluid trajectories are small. However, in contrast to lubrication theory that utilizes such assumptions, inertial effects are retained since the flow may be rapid. The

simplified time-dependent Navier-Stokes equations and continuity equation are integrated across the film thickness H, and boundary conditions at the wall (no slip and kinematic conditions), and interface (dynamic condition simplified for small slope, kinematic condition) are applied. The result is an integral equation equivalent to the simplified system of equations and boundary conditions. Following the approach pioneered by Von Karmen/Polhausen in their treatment of boundary layer theories [30, 31, 24], a velocity profile parabolic in Y (see coordinate system in Figure II.2) is assumed that satisfies the wall boundary conditions, a no shear condition at the unknown interface location $H(X,T)$, and integrates to yield the local volumetric flow per width, $Q(X,T)$. The resulting system of equations may be written in dimensionless form as [29]:

$$\frac{\partial \bar{Q}}{\partial x} + \frac{\partial \bar{H}}{\partial t} = 0 \tag{II.4a}$$

$$\frac{\partial \bar{Q}}{\partial t} + \frac{6}{5}\frac{\partial}{\partial x}\left(\frac{\bar{Q}^2}{\bar{H}}\right) = \frac{3}{Re}\left(\bar{H} - \frac{\bar{Q}}{\bar{H}^2} - \bar{H}\frac{\partial \bar{H}}{\partial x}\cot\theta\right) + \frac{1}{We}\bar{H}\frac{\partial^3 \bar{H}}{\partial x^3}, \tag{II.4b}$$

where:

$$\bar{H} = \frac{H}{H_0},\ \bar{Q} = \frac{Q}{Q_0},\ x = \frac{X}{H_0},\ t = \frac{TQ_0}{{H_0}^2},\ Re = \frac{\rho Q_0}{\mu},\ We = \frac{\rho {Q_0}^2}{\sigma H_0}. \tag{II.4c}$$

Note that H_0 and Q_0 are not independent and are related as follows

$$H_0 = \left(\frac{3Q_0\mu}{\rho g \sin\theta}\right)^{1/3}, \tag{II.4d}$$

where H_0 is the exact expression for the steady-state thickness for film flow calculated from the Navier-Stokes equations [32].

The nonlinear system (II.4) can further be simplified by restricting attention to small interfacial perturbations, which is justified in practical applications where highly uniform films are desired [6].

The following forms are assumed:

$$\bar{H} \sim 1 + h(x,t),\ \bar{Q} \sim 1 + q(x,t),\ h << 1 \text{ and } q << 1. \tag{II.5}$$

Equation (II.5) is substituted into the system (II.4) and terms quadratic or higher in the perturbation quantities h and q are neglected. The two linearized equations corresponding to (II.4a) and (II.4b) are combined into a single equation to yield:

$$\frac{\partial^2 h}{\partial t^2} + \frac{3}{Re}\frac{\partial h}{\partial t} + \frac{12}{5}\frac{\partial^2 h}{\partial x \partial t} + \frac{1}{We}\frac{\partial^4 h}{\partial x^4} + \left(\frac{6}{5} - \frac{3\cot\theta}{Re}\right)\frac{\partial^2 h}{\partial x^2} + \frac{9}{Re}\frac{\partial h}{\partial x} = 0. \tag{II.6a}$$

This is the desired governing equation that will be examined in what follows. In accordance with the geometry in Figure II.2, the spatial domain that will be considered is $-\infty < x < \infty$, and the following boundary conditions and initial conditions are applied:

$$h = h_0\delta(x),\ \frac{\partial h}{\partial t} = u_0\delta(x) \text{ at } t = 0, \tag{II.6b}$$

$$h \to 0 \text{ as } x \to \pm\infty. \tag{II.6c}$$

In (II.6b), h_0 and u_0 are constants and $\delta(x)$ is the Dirac delta function. The system (II.6) is well posed to solve for the response $h(x,t)$. Note that, although (II.6a) is homogeneous, including an impulsive pressure forcing of $f_0\delta(x)\delta(t)$ would have the same response as the initial velocity condition imposed in (II.6b) as seen for the problem of Section 2 from [16]; thus, we have not incorporated it here.

II.3. Classical stability analysis

We now proceed to examine the classical stability of equation (II.6a). To do so, the conditions (II.6b) and (II.6c) are neglected, and the following disturbance form is assumed:

$$h = Ae^{i(kx-\omega t)}. \tag{II.7}$$

In (II.7), k is a real wavenumber, $\omega = \omega_r + i\omega_i$ is a generally complex frequency, and A is a constant. Substituting (II.7) into (II.6a) and rearranging to assure a non-trivial solution leads to the following:

$$\omega^2 + i\beta\omega - \gamma = 0, \tag{II.8a}$$

$$\beta = \left(\frac{3}{Re} + \frac{12i}{5}k\right),\ \gamma = \frac{k^4}{We} - k^2\left(\frac{6}{5} - \frac{3\cot\theta}{Re}\right) + \frac{9ik}{Re}. \tag{II.8b}$$

As shown by [27], the neutral stability condition may be deduced by examining the long wavelength limit as a perturbation series about $k \to 0$ holding $c = \omega/k$ fixed, which assures that the speed of any disturbance given by the real part of c is finite. Equation (II.8) is first rewritten for fixed c by inserting $\omega = ck$, and the following expansion is inserted into the result:

$$c \sim c_0 + c_1 k + c_2 k^2 + c_3 k^3 + O(k^4) \text{ as } k \to 0,\ c = \omega/k \text{ fixed} \tag{II.9}$$

where equating like powers leads to

$$c_0 = 3, \tag{II.10a}$$

$$c_1 = i\left(Re - \cot\theta\right), \tag{II.10b}$$

$$c_2 = \frac{6}{5}Re\left(\cot\theta - Re\right), \tag{II.10c}$$

$$c_3 = i\left[\frac{36}{25}Re^2\left(\cot\theta - Re\right) - \frac{12}{5}Re^3\left(\cot\theta - Re\right)^2 - \frac{Re}{3We}\right]. \tag{II.10d}$$

Finally, the results (II.10) can be rewritten using the definition of c in (II.9) to obtain the final form of ω as:

$$\begin{aligned}\omega \sim & 3k + i(Re - \cot\theta)k^2 + \frac{6}{5}Re\left(\cot\theta - Re\right)k^3 \\ & + i\left[\frac{36}{25}Re^2\left(\cot\theta - Re\right) - \frac{12}{5}Re^3\left(\cot\theta - Re\right)^2 - \frac{Re}{3We}\right]k^4 + O(k^5) \text{ as } k \to 0.\end{aligned} \tag{II.11}$$

According to the form (II.7), the response grows exponentially if $\omega_i > 0$, and thus according to (II.11) for $k \neq 0$, there is growth when $Re > \cot\theta$. The approximate nature of equation (II.6) is revealed here, for when the full linearized Navier-Stokes system is analyzed in the long wavelength limit, the exact result from [27] is that instabilities arise for $Re > {}^{5}/_{6}\cot\theta$; apart from the coefficient difference, the interpretation of instability is identical to that of the approximate analysis. Note that, to make his stability assessment, Yih only retained terms to order k^2 in (II.11) (i.e., $O(k)$ in (II.9)). While the additional terms in (II.11) do not alter the above stability conclusions, they are required to enable the analysis in Section II.4.

The classical interpretation of exponential growth in the long wavelength limit warrants additional discussion relevant to the current work. In particular, equation (II.11) indicates that $\omega_i = 0$ when $k = 0$, and thus equation (II.7) shows that this wavenumber exhibits a neutrally stable condition. Figure II.3 provides a schematic of the growth rate, ω_i, as a function of k, for $k \geq 0$, based on solutions of the Orr-Somerfeld equations (see, for example [33, 28]). As indicated in curve (a), for $Re > \cot\theta$, waves exponentially grow over a range of k, with the maximum wave growth occurring at finite k. For smaller Re that satisfies $Re > \cot\theta$ given by curve (b), the wavenumber associated with maximum growth is reduced, until at the neutral condition shown by curve (c), this wavenumber becomes coincident with $k = 0$; for all $k \neq 0$, modes damp exponentially in accordance with (II.7). This same structure persists for $Re < \cot\theta$. For all curves shown in Figure II.3, note that $k = 0$ is in fact a wavenumber that exibits neither growth nor decay, from the classical characterization.

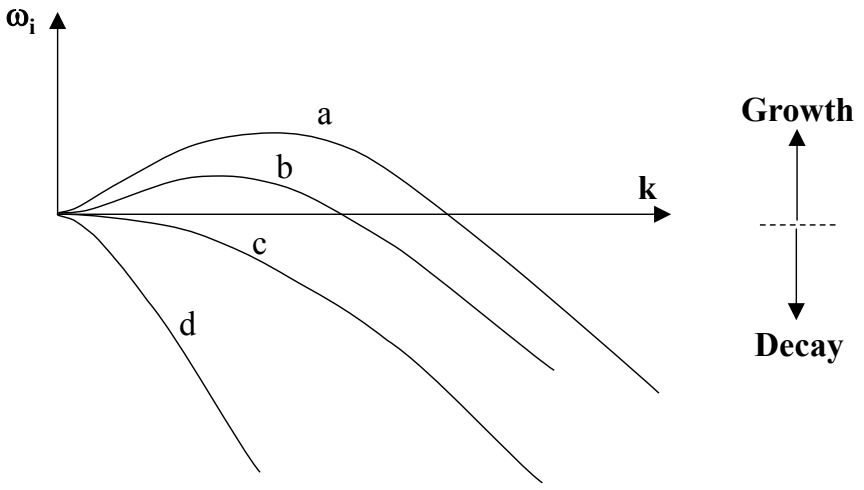

[Figure]

Figure II.3: Qualitative plot of growth rate, ω_i, vs real wavenumber, k, for various values of Re. In the $k \to 0$ limit, ω_i is given by equation (II.11). Curve a): $Re > \cot\theta$, an unstable condition. Note that the maximum growth rate occurs at a finite wavenumber. Curve b): Smaller Re than curve a, but still satisfying $Re > \cot\theta$. Note that the maximum growth rate is reduced and has shifted to smaller wavenumber. Curve c): The first condition at which there is no growth as Re is lowered is $Re = \cot\theta$. Curve d): $Re < \cot\theta$. For curves c) and d) Modes exponentially damp for all $k \neq 0$, and $k = 0$ is the wavenumber of maximum (but zero) growth.

The Orr-Somerfeld solutions in Figure II.3 show why a stability assessment for $Re > \cot\theta$ may be made based on the $k \to 0$ limit. Although the maximum growth in this parameter range generally occurs at a finite value of k, the concavity of the asymptotic solution (II.11) is always positive when there is growth; this enables positive concavity in the $k \to 0$ limit to assure instability. For situations where $Re = \cot\theta$ or $Re < \cot\theta$, the concavity of (II.11) is zero or negative, respectively. For these cases, however, the $k = 0$ wavenumber precludes a stability conclusion (as pointed out by [27]), since $k = 0$ corresponds to the wavenumber

of maximum (zero) growth. We set out to make this assessment in the analysis to follow, where we explicitly examine the system response for cases where $Re \leq \cot\theta$ via asymptotic analysis.

II.4. Integral solution and long-time asymptotic behavior

We now proceed to solve the system (II.6) and examine its stability features, following the process discussed in Section 2.2 of [16]. The Fourier transform is defined as

$$\hat{h}(k,t) = \int_{-\infty}^{\infty} h(x,t)e^{-ikx}dx, \tag{II.12a}$$

$$h(x,t) = \frac{1}{2\pi}\int_{-\infty}^{\infty} \hat{h}(k,t)e^{ikx}dk. \tag{II.12b}$$

Taking the transform of equation (II.6) yields

$$\frac{d^2\hat{h}}{dt^2} + \beta\frac{d\hat{h}}{dt} + \gamma\hat{h} = 0. \tag{II.13a}$$

It is implicit in the use of the Fourier transform that equation (II.6c) is satisfied. The associated initial conditions (II.6b) become:

$$\hat{h} = h_0,\ \frac{\partial\hat{h}}{\partial t} = u_0 \text{ at } t = 0. \tag{II.13b}$$

The ordinary differential system (II.13) is solved to yield

$$\hat{h} = C_1(k)e^{-i\omega_1(k)t} + C_2e^{-i\omega_2(k)t}, \tag{II.14}$$

where $\omega_1(k)$ and $\omega_2(k)$ are the two roots of the quadratic equation (II.8) given as

$$\omega_1(k) = -\frac{i}{2}\left(\beta - \sqrt{\beta^2 - 4\gamma}\right),\ \omega_2(k) = -\frac{i}{2}\left(\beta + \sqrt{\beta^2 - 4\gamma}\right) \tag{II.15a}$$

and

$$C_1(k) = \frac{\omega_2 h_0 - i u_0}{\omega_2 - \omega_1},\ C_2(k) = \frac{i u_0 - \omega_1 h_0}{\omega_2 - \omega_1} \tag{II.15b}$$

The final solution for $h(x,t)$ may be obtained by utilizing the inverse Fourier Transform (II.12b) to obtain

$$h\left(x,t\right) = \frac{1}{2\pi} \int\limits_{-\infty}^{\infty} \left[C_1(k) e^{\phi_1(k)t} + C_2(k) e^{\phi_2(k)t} \right] dk, \tag{II.15c}$$

where

$$\phi_1(k) = i\left[k\frac{x}{t} - \omega_1(k) \right],\ \phi_2(k) = i\left[k\frac{x}{t} - \omega_2(k) \right]. \tag{II.15d}$$

The result (II.15) provides the integral solution to the system (II.6), where β and γ are given in (II.8b).

The long time asymptotic behavior of (II.15) for $Re \leq \cot(\theta)$ may be used to establish the stability of the flow system governed by equation (II.6). In Appendix A.1, it is shown that the second term in (II.15c) damps faster than the first as $t \to \infty$ for all k, and so we may recast (II.15c) as

$$h\left(x,t\right) \sim \frac{1}{2\pi} \int\limits_{-\infty}^{\infty} C_1(k) e^{\phi_1(k)t} dk,\ t \to \infty,\ Re \leq \cot(\theta). \tag{II.16}$$

Although we cannot determine a closed-form solution for the Fourier integral in (II.16), it can be evaluated via the method of steepest descent [34], where we allow $k = k_r + i k_i$ to be complex and look for a closed integration path (in the complex k-plane) that includes the real line and passes through a saddle point of (II.15d); this enables the use of Cauchy's theorem. An n^{th} order saddle k_s of ϕ_1 is defined by

$$\left.\frac{d\phi_1}{dk}\right|_{k_s} = \cdots = \left.\frac{d^{n-1}\phi_1}{dk^{n-1}}\right|_{k_s} = 0,\ \ \left.\frac{d^n\phi_1}{dk^n}\right|_{k_s} \neq 0,\ n > 1. \tag{II.17}$$

Note that, depending on the direction of approach, saddle points can describe where Real$[\phi_1]$ reaches a maximum *or* minimum. The deformed integration path of steepest descent moves through the saddle such that the imaginary part of $\phi_1(k)$ is constant and real part of $\phi_1(k)$ attains its *maximum* value at the saddle. This enables an asymptotic expansion about the saddle point, which can be used to deduce the dominant behavior as t becomes large. The path of ascent, where a minimum of Real$[\phi_1]$ is reached at the saddle, is not useful in the long-time evaluation of Fourier integrals such as (II.16). Note that (II.16) contains branch points when $\beta^2 = 4\gamma$ and so care must be taken such that the aforementioned path does not enclose such points, as this would violate Cauchy's theorem.

Substituting (II.15d) into (II.17) leads to the relations for $\omega(k) = \omega_r(k) + i\omega_i(k)$

$$\left.\frac{d\omega_r}{dk_r}\right|_{k_s} = \frac{x}{t}, \tag{II.18a}$$

$$\left.\frac{d\omega_i}{dk_r}\right|_{k_s} = 0. \tag{II.18b}$$

Equation (II.18) highlights that each saddle point k_s is paired with an x/t ray; it provides a simultaneous set of equations to solve for the real and imaginary parts of k_s for a given x/t. We may deduce the long-time behavior of (II.16) along specific x/t values by expanding $\phi_1(k)$ about the corresponding saddles. Using this expansion within the method of steepest descent outlined above (see Appendix A.2), we arrive at the following long-time behavior for (II.16)

$$h\left(x,t\right)|_{\frac{x}{t}=3} \sim \frac{h_0 + u_0\ Re/3}{2\sqrt{\pi\left[\cot(\theta) - Re\right]}}\ t^{-\frac{1}{2}}, \quad Re < \cot(\theta), \tag{II.19a}$$

$$h\left(x,t\right)|_{\frac{x}{t}=3} \sim \frac{1}{4\pi}\Gamma\left(\frac{1}{4}\right)\left[\frac{3\ We}{Re}\right]^{\frac{1}{4}}\left(h_0 + u_0\ Re/3\right)\ t^{-\frac{1}{4}}, \quad Re = \cot(\theta), \tag{II.19b}$$

$$h\left(x,t\right)|_{\frac{x}{t}\neq 3} \sim f_1 t^{-\frac{1}{2}} e^{f_2 t}\cos\left(f_3 t + f_4\right), \quad c_2 < 0,\ Re \leq \cot(\theta), \tag{II.19c}$$

where the real-valued parameters f_1, f_2, f_3, and f_4 are functions of x/t. A more specific form of (II.19c) for direct use is given by (A.24) in Appendix A.2. Note that there is a structural change for $x/t = 3$ and $x/t \neq 3$ (for all $Re \leq \cot(\theta)$). For any Re, $x/t = 3$ is the least damped ray, only exhibiting algebraic decay, while all other rays damp exponentially at $t \to \infty$. There is also a structural change for $Re < \cot(\theta)$ and $Re = \cot(\theta)$ along the ray $x/t = 3$. For $Re < \cot(\theta)$, the peak of the wave packet (at $x/t = 3$) decays like $t^{-1/2}$. For $Re = \cot(\theta)$, the peak of the wave packet decays like $t^{-1/4}$. This is a ramification of the saddle point being 2^{nd}-order for the former and 4^{th}-order for the latter, as shown in Appendix A.2; this change of order can also be seen in (II.11), setting $Re = \cot(\theta)$. Here, we have deduced the stability of the system (II.6) for $Re \leq \cot(\theta)$, in a parameter space where classical stability analysis is inconclusive.

The Fourier series solution to (II.6) is shown in Figure II.4, where the peak is seen to decay in accordance with the asymptotic solution given by (II.19b) along $x/t = 3$, as indicated by a black line in the figure. Away from the peak (for $x/t \neq 3$) the series solution approaches the asymptotic solution given by (II.19c), as indicated in Figure II.5.

II.5. Conclusions

Flow transition from stability to instability is examined in which a single mode (i.e., for one value of wavenumber) indicates classical neutral stability. It is found that fluid flows characterized as being neutrally stable via exponential modes in fact may exhibit either algebraic growth or decay. A partial differential equation system is examined, one that has been constructed to model the well-studied problem of rectilinear Newtonian flow down an

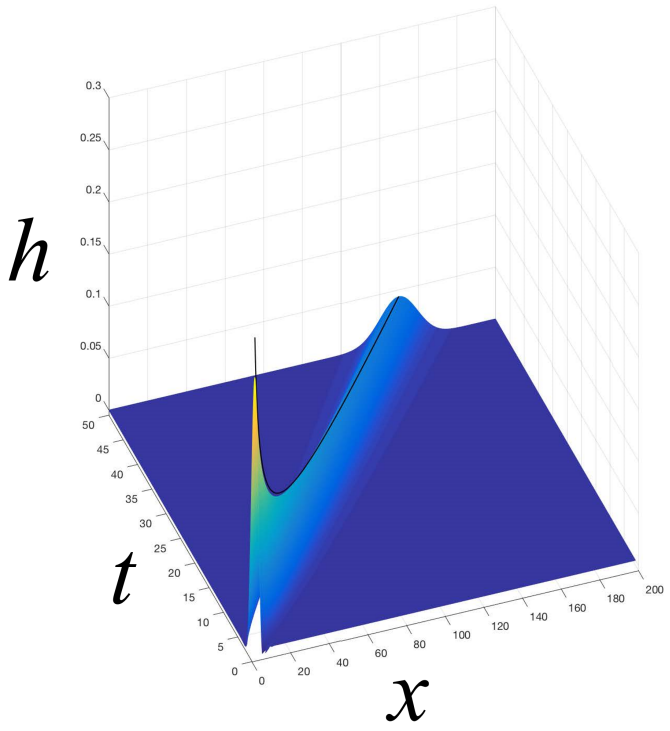

Figure II.4: Fourier series solution (shaded surface) to (II.6) compared with (II.19b) (black curve) along the line $x/t = 3$. $Re = \cot(\theta)$, $h_0 = u_0 = 1$, $\theta = \pi/4$, and $We = 0.1$.

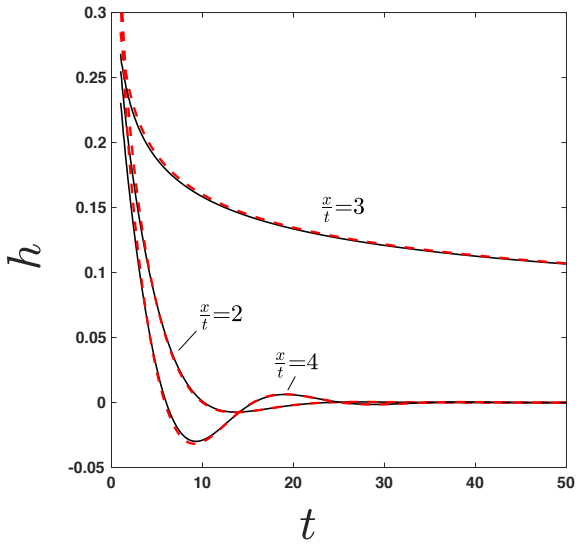

Figure II.5: Fourier series solution (solid curves) to (II.6) along specific x/t rays, compared with the long-time asymptotic solution given by (II.19) (dashed curves) for $Re = \cot(\theta)$, $h_0 = u_0 = 1$, $\theta = \pi/4$, and $We = 0.1$.

inclined plane. In this case, algebraic decay occurs both at and below the critical Reynolds number.

For the problem reported here, exponential growth occurs above a critical Reynolds number. In his own work [27], Yih also reached the conclusion that the flow is unstable above the critical value, but could not reach a conclusion for when the Reynolds number was below the critical value. The discovery of algebraic stability below the critical Reynolds number carries with it the danger that the flow will not be as stable as it would be if all values of ω_i were negative and disturbances damped exponentially. In the context of coating operations that utilize an inclined plane-flow geometry to form liquid films, our results show that disturbances to a process, even if damped, will damp out more slowly than expected in the physical domain. It is possible that, given larger disturbances, even a damped response

may lead to unacceptable perturbations in coated liquid films.

Chapter III

On the response of neutrally stable flows to oscillatory forcing with application to liquid sheets

III.1. Introduction

Many liquid film coating processes have tight product specifications and require precise control over process conditions. Such processes are used, for example, to produce printed electronics, liquid display screens, high quality papers used for printing, and more [4, 5]. Industrial processes are inevitably subject to ambient disturbances, some impulsive such as those from the sudden repositioning of equipment, and some repetitive from vibrations due to pumps and fans. Perhaps the simplest model for the response of fluid flows to repetitive

disturbances is the so-called "signaling" problem, defined in one dimension (1D) as

$$Lh = A_f e^{i\omega_f t}\delta(x), \tag{III.1}$$

where L is a linear governing operator, t is time, A_f is the forcing amplitude, ω_f is the forcing frequency, $\delta(x)$ is the Dirac delta function, and $x \in (-\infty, \infty)$. Equation (III.1) is subject to constraints to make the problem well-posed; the number of constraints is determined from the number of spatial and time derivatives in L. The signaling problem admits two components of the solution, the transient behavior due to the start-up of the disturbance and the long-time signaling behavior due to the oscillatory forcing. While most real-world disturbances occur over multiple frequencies and locations, (III.1) provides a simple model from which the responses to arbitrary forcing functions can be constructed via superposition and the method of Green's functions; these are afforded by the linearity of the operator.

The motivation of this chapter lies in the need to characterize how the response to signaling from inevitable disturbances in manufacturing flows will propagate; this includes a characterization of both the breadth (how much of the product will be affected) and the amplitude of the response (how badly will the product be affected).

In order to characterize the response of (III.1), a first step is to examine the stability of the unforced medium itself by assessing response behavior of the homogeneous form $Lh = 0$; this approach, known as classical stability analysis, is used extensively in the hydrodynamic literature [8, 9, 10, 11]. The solution to the homogeneous equation is expressed as an infinite

sum of complex modes,

$$h(x,t) = \sum h_k(x,t) = \sum A_k e^{i(k_r x - \omega t)} \tag{III.2}$$

with complex amplitude, A_k, real wave number, k_r, and complex frequency, $\omega = \omega_r + i\omega_i$. The form (III.2) is substituted into the homogeneous operator without constraints, and nontrivial solutions are obtained that enable A_k to be arbitrary. The result is a dispersion relation of the form $\omega = \omega(k_r)$. Notably, the assumed modal form, h_k, can be rewritten as an exponential term times an oscillatory term,

$$h_k = A_k e^{(\omega_i t)} e^{i(k_r x - \omega_r)t}. \tag{III.3}$$

In the summation (III.2), the mode (or modes) that grows the fastest or decays the slowest will dominate the overall response as time goes to infinity. Therefore, we can express the magnitude of h for $\omega_{i,\max} \equiv \mathrm{Im}[\omega]$ and with the associated A_k value $A_{\max}$ as

$$|h_{\max}| \sim \left| A_{\max} e^{\omega_{i\max} t} \right| \quad \text{as} \quad t \to \infty. \tag{III.4}$$

In (III.4), the sign of $\omega_{i,\max}$ is used to determine the classical stability for a given set of conditions as follows [8, 12, 9]:

$$\omega_{i,\max} < 0: \quad \text{The system is stable,} \tag{III.5a}$$

$$\omega_{i,\max} = 0: \quad \text{The system is neutrally stable,} \tag{III.5b}$$

$$\omega_{i,\max} > 0: \quad \text{The system is unstable.} \tag{III.5c}$$

However, the method fails to properly classify neutrally stable (III.5b) cases where the maximum value (or all values) of ω_i is zero. Such cases can lead to emergent algebraic behavior, as seen in [15, 16] (and the references therein), where the solution magnitude

goes as t raised to a fractional power, such as $t^{1/2}$ or $t^{-1/2}$. Such behavior is fascinating because it arises from the summation of modes and cannot be deduced from any individual exponential mode or finite set of modes as in classically stable or unstable systems.

As shown in previous literature [35, 36, 37], the spatio-temporal stability of the underlying medium itself (deduced from the homogeneous governing equation (III.1)) is central to the relevance of signaling. In fact, transients are carried by the homogeneous solution, and these are initiated at $t = 0$ in any system through initial conditions. Previous work on signaling in spatio-temporal systems has focused on systems having exponential growth or decay in time according to (III.4) and (III.5). If a flow is temporally stable, then the effects of transients damp exponentially with time and the response to the forcing in (III.1) persists as the dominant solution. Alternatively, if a flow is temporally unstable but convective, transients will propagate away from the source even as they grow exponentially with time, and once again, the response to forcing in (III.1) remains in any finite domain after the transient passes through. In this case, then, the processes can be controlled by minimizing disturbances and adjusting the rate at which exponential growth occurs through the choice of process conditions[1], so that the response magnitude remains sufficiently small over a given finite domain. If a flow is absolutely unstable, however, transients remain in the domain, never dissipate as they grow exponentially with time, and overwhelm the effect of forcing in (III.1); therefore, the forcing solution in this case is subdominant to the transients at large times and thus is not of practical importance. Absolutely unstable processes cannot be controlled by minimizing process disturbances, as responses remain in the domain as

[1] In fluid systems, this can include viscosity, flow rate, etc.

they grow. As a result, it is impossible to maintain a high-precision process in absolutely unstable systems as products are pushed out of specifications.

Thus far, the solution response governed by linear operators that admit algebraic growth has only been studied for impulsive forcings [15, 16]. In this work, we elucidate the structure of the response of a neutrally stable flow to a localized oscillatory forcing (i.e., the signaling problem (III.1)).

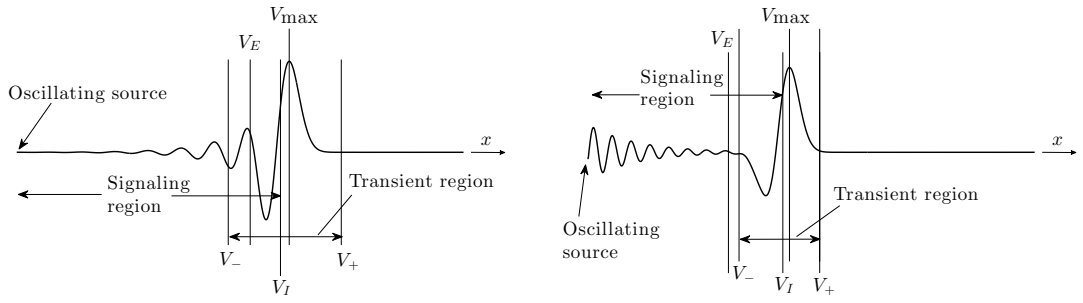

III.1a III.1b

Figure III.1: Schematics of exponentially unstable signaling problems studied by Barlow et al. [36] replicated here with permission. Figure III.1a is spatially unstable and Figure III.1b is spatially stable. The velocities V_+ and V_- are the bounds of the transient growth envelope around the peak $V_{\max}$, the velocities V_I are the farthest downstream locations where the oscillating source affects the solution (the signaling region), and the velocity V_E marks the point where the growth rate of waves generated by the oscillatory forcing are is the same as those of the transient solution.

It is useful to examine the closely-related signaling problem for operators that admit exponential growth and decay; see Barlow et al. [36] and references contained therein for an extensive review. Figure III.1 provides a schematic of the signaling response in such cases. As indicated, the structure of the solution is delineated by well-defined velocities;

these velocities are extracted naturally from the long-time behavior using the method of steepest descent [34]. In particular, one can readily extract the bounding envelope of the transient (V_+,V_-) from the asymptotic expressions where the growth rate of the transient is zero, the farthest extent of the so-called signaling region (V_I) from pole inclusion in the relevant contour integrations, and the velocity (V_E) from the equality of the transient and forced oscillation response amplitudes. We demonstrate herein that the structure of the signaling response in a system that admits algebraic growth also has critical velocities, but the structure is markedly different. The neutrally stable system studied in this chapter only has two types of velocities relevant to the overall structure: Those that correspond to the peak of the transient (of the type $V_{\max}$ in Figure III.1) and those due to the inclusion of poles (of the type V_I in Figure III.1). While our approach is analogous to the studies that map the regions of interaction between exponentially growing waves (in space and time) in a classically unstable signaling problem [35, 36, 37], the signaling problem examined here has a distinctly different structure that is explored through careful asymptotic analysis.

The chapter is organized as follows: In Section III.2, we pose the signaling problem that governs varicose waves in an inviscid planar liquid sheet at neutral stability. The governing linear operator here admits algebraic growth of waves when initiated by an impulse disturbance, as shown by King et al. [15]. In the subsequent sections, the signaling response is fully characterized through Fourier analysis and asymptotic methods. This examination begins in Section III.3, where the Fourier integral solution is provided. In Section III.3.1, critical velocities are determined that delineate regions of the signaling response — this parallels the structure found in responses that exhibit exponential growth

or decay as discussed above. Section III.3.2 describes the method to extract the bounding amplitudes of the oscillatory signaling response via analytical means. In Section III.4, results showing the structure of the signaling response are provided, and Section III.5 provides more insight. The results are discussed in Section III.6; this section also includes discussion which contrasts signaling in systems that admit algebraic and exponential growth. Concluding remarks are provided in Section III.7.

III.2. Formulation: The signaling problem

To uncover key features of signaling in a neutrally stable flow, we introduce localized oscillatory forcing to the model of King et al. [15] as,

$$\frac{\partial^2 H}{\partial t^2} + c^2\frac{\partial^2 H}{\partial x^2} + 2c\frac{\partial^2 H}{\partial x \partial t} + B^2\frac{\partial^4 H}{\partial x^4} = A_f e^{(i\omega_f t)}\delta(x), \tag{III.6a}$$

$$H(x,0) = H_0\delta(x), \qquad \frac{\partial H}{\partial t}(x,0) = U_0\delta(x), \qquad H \to 0 \quad as \quad x \to \pm\infty, \tag{III.6b}$$

where H is the system response (given physical context in the discussion below), H_0 is the real amplitude of the impulsive perturbation in initial height, U_0 is the real amplitude of the impulsive perturbation in initial surface velocity, and the parameters B and c are real-valued coefficients. In order to study different phases of sinusoidal forcing, A_f is taken to be complex. Note that in King et. al., $\delta(t)$ is used instead of $e^{i\omega_f t}$ in the right-hand side of (III.6a), as the focus of that work was the response of the operator to impulsive disturbances [15].

Physically, the linear operator in (III.6) governs the propagation of long varicose waves in an inviscid planar liquid sheet in the absence of ambient gas once the identifications

$B = We^{-1/2}$ and $c = 1$ [2] are made. In this context, $We = \frac{\rho_l u^2 h_0}{\sigma}$ is the dimensionless Weber number, where ρ_l is the liquid density, u is the liquid velocity in the sheet, h_0 is the half-sheet thickness, and σ is the surface tension; a schematic is provided in Figure III.2. This flow has long been known to be neutrally stable [2, 22] in accordance with (III.5) and exhibits algebraic instability [15, 23] when U_0 is nonzero. In the context of varicose waves in liquid sheets, the oscillatory forcing introduced here has only been studied for responses, taken in *the presence of ambient gas*, that admit exponential growth [37] and are governed by a different operator than (III.6). In the following sections, we uncover, for the first time, the structure that arises when signaling is imposed on a neutrally stable flow.

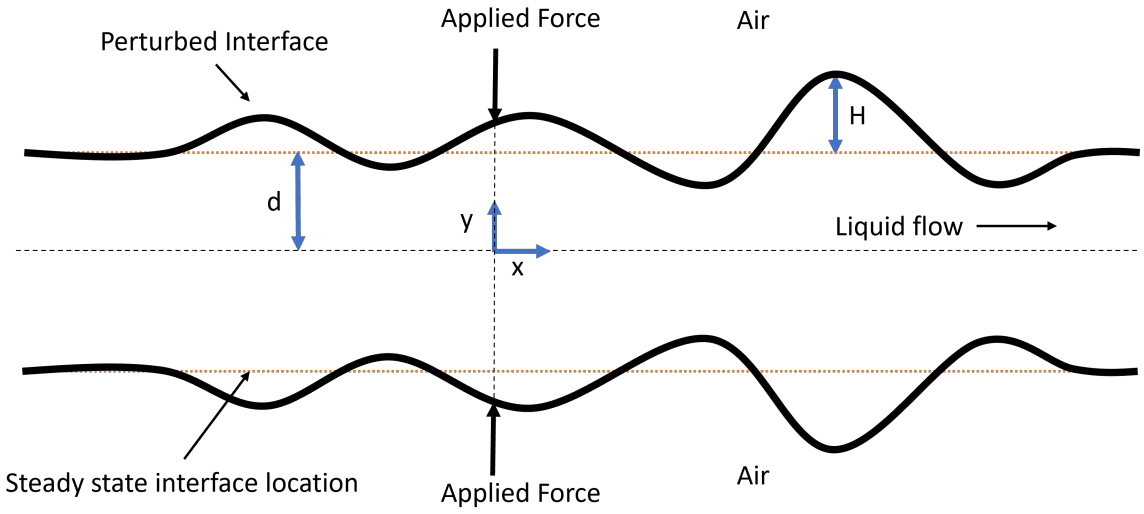

Figure III.2: Schematic of varicose waves in a planar liquid sheet. The flow is invariant in the z direction, which is oriented into and out of the page. The non-dimensional steady state half-sheet thickness is d, and the perturbations from it are given by height H. Note that the indicated response H has been exaggerated for clarity, H must be much smaller than d to be consistent with the linearity assumption.

Because the partial differential equation (PDE) in (III.6) is linear, the dependent variable,

H, can be expressed by superposition as follows:

$$H(x,t) = g(x,t) + h(x,t),$$

where g and h are expressed as

$$\frac{\partial^2 g}{\partial t^2} + c^2\frac{\partial^2 g}{\partial x^2} + 2c\frac{\partial^2 g}{\partial x \partial t} + B^2\frac{\partial^4 g}{\partial x^4} = 0, \tag{III.7a}$$

$$g(x,0) = H_0\delta(x), \qquad \frac{\partial g}{\partial t}(x,0) = U_0\delta(x), \qquad g \to 0 \quad as \quad x \to \pm\infty, \tag{III.7b}$$

and

$$\frac{\partial^2 h}{\partial t^2} + c^2\frac{\partial^2 h}{\partial x^2} + 2c\frac{\partial^2 h}{\partial x \partial t} + B^2\frac{\partial^4 h}{\partial x^4} = A_f e^{(i\omega_f t)}\delta(x), \tag{III.8a}$$

$$h(x,0) = 0, \qquad \frac{\partial h}{\partial t}(x,0) = 0, \qquad h \to 0 \quad as \quad x \to \pm\infty. \tag{III.8b}$$

The split between (III.7) and (III.8) allows us to study the effect of the forcing on (III.8) without repeating the work done by King et al. [15]. Note that equation (III.7) omits the impulsive forcing ($A\delta(x)\delta(t)$) present in King et al. as it can be shown that it is equivalent to a disturbance in the initial surface velocity with $A = U_0$ in (III.7). King et al. find that, for nonzero U_0, the solution propagates and grows as $t^{1/2}$ along the single velocity $x/t = c$; however, a nonzero displacement H_0 in (III.7b) yields a damped solution. The superposition above allows us to focus specifically on the response to the oscillatory forcing in (III.8), and how the long-time response to the forcing (i.e., signaling) evolves past the transients invoked by the start-up.

III.3. Fourier Integral Solution

The solution to (III.8) is found by taking the Fourier transform in x, solving the resulting ordinary differential equation in time, and setting up the Fourier inversion integral (see

Appendix B.2 for additional details). The inversion integral is broken into two integrals, $\tilde{I}$ and $\hat{I}$ as

$$h = \frac{\tilde{I} + \hat{I}}{2\pi}, \tag{III.9a}$$

$$\tilde{I} = \int_{-\infty}^{\infty} \frac{-\frac{A_f e^{i(\omega_f)t}}{B^2} e^{i(kV)t} \left(e^{iB(k-k_2)(k-k_3)t} - 1 \right)}{(k-k_0)(k-k_1)(k-k_2)(k-k_3)} dk, \tag{III.9b}$$

$$\hat{I} = \int_{-\infty}^{\infty} \frac{iA_f \sin(Bk^2 t) e^{i(kV-kc)t}}{k^2 B^2 (k-k_0)(k-k_1)} dk, \tag{III.9c}$$

$$\begin{aligned} k_0 &= \frac{-c - \sqrt{c^2 - 4B\omega_f}}{2B}, \qquad k_1 = \frac{-c + \sqrt{c^2 - 4B\omega_f}}{2B}, \\ k_2 &= \frac{c - \sqrt{c^2 + 4B\omega_f}}{2B}, \qquad k_3 = \frac{c + \sqrt{c^2 + 4B\omega_f}}{2B}, \end{aligned} \tag{III.9d}$$

where $V \equiv x/t$ is taken to be a fixed velocity at which we evaluate the integral. Note that the introduction of V as a fixed parameter naturally arises through analysis of the long-time asymptotics of the integral. Furthermore, from prior work discussed in Section III.1, structural changes in the solution are naturally characterized by different values of V.

A key feature of the integrals in (III.9) are the poles k_0 through k_3 which arise from the forcing function. When we evaluate (III.9b) and (III.9c) through complex contour integration, the location of the poles determines whether they have an effect on the solution; contours are examined in Supplmental Materials Sections B.7 and B.8. A significant change occurs in the structure based on the sign of square root discriminants in (III.9d). The critical value of forcing frequency, denoted as ω_c, arises when the discriminants of k_0 and k_1 are zero, i.e.

$$\omega_c = \frac{c^2}{4B}. \tag{III.10}$$

When the system is forced at a frequency higher than the critical value ($\omega_f > \omega_c$), all four poles lie on the real k axis, as shown in Figure III.3. When the system is forced at a frequency lower than the critical value ($\omega_f < \omega_c$), poles k_0 and k_1 (III.9d) lie off of the real k axis and poles k_2 and k_3 (III.9d) lie on the real k axis, as shown in Figure III.4. In what follows, we will explore the structure arising from values of $\omega_f < \omega_c$ and $\omega_f > \omega_c$. The case of $\omega_f = \omega_c$ is examined using the FSS(Appendix B.1.1) of (III.8) and addressed at the end of Section III.5.

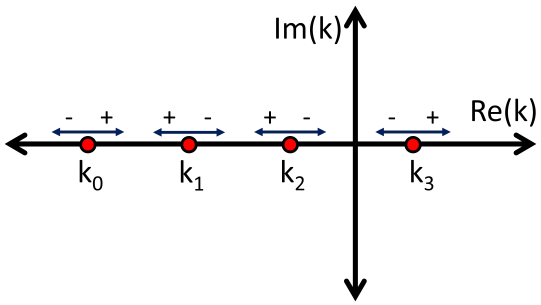

Figure III.3: $\omega_f < \omega_c$: General schematic showing the movement of the poles with small increases (+) and decreases (−) in the forcing frequency, ω_f, for $\omega_f < \omega_c$. Note that all four poles lie on the real k axis.

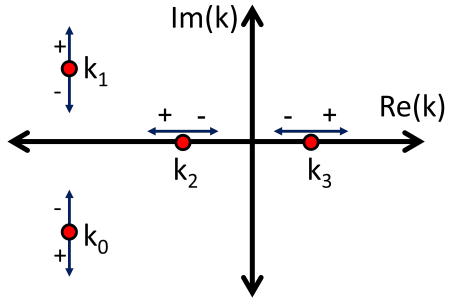

Figure III.4: $\omega_f > \omega_c$: General schematic showing the movement of the poles with small increases (+) and decreases (−) in the forcing frequency, ω_f, for $\omega_f > \omega_c$. Note that k_0 and k_1 lie off of the real axis, and k_2 and k_3 lie on the real axis.

The two cases ($\omega_f < \omega_c$ and $\omega_f > \omega_c$) are handled separately in the analysis due to the difference in pole structure shown in Figures III.3 and III.4. As ω_f is varied within these regions, poles translate in the complex k-plane, indicated by the arrows emanating from

each pole. As shall be seen in Appendix B.2, the location of these poles is crucial to the asymptotic evaluation of the Fourier integral solution (III.9) in the limit as $t \to \infty$.

One key detail of the analysis is that contour integration is used to evaluate the integrals in (III.9), and the position of the contour in the complex plane is a function of the velocity V in (III.9). This means that, for a fixed set of parameters, the velocity at which the integral is being evaluated determines the poles that are enclosed, and this, in turn, changes the structure of the solution. The details of the asymptotic evaluation of the inversion integrals is provided in Appendix B.2.

III.3.1 Approach to determine critical velocities

Critical velocities examined in spatio-temporal problems have been used to delineate structural changes in solution responses having exponential growth or decay [9] as shown in Figure III.1. However, many of the critical velocities in such systems are based on transitions between exponentially growing and decaying portions of the solution response [35, 36, 37]. Thus, many of the "bounding velocities" and associated structural changes are different when an operator that admits algebraic growth is considered.

Here, we define *critical velocities* as those which — based on pole, saddle, and contour orientation — delineate *possible* structural changes in the solution. The analysis of the structure begins by extracting all possible critical velocities. Of these critical velocities, there are two categories, observable and non-observable. While both categories are associated with structural changes in the solution, only those associated with the observable critical velocities persist and delineate distinct regions of the solution response in the long-time limit.

The distinction between these regions, as well as their width, is crucial to understanding how disturbances propagate in a forced neutral flow such as (III.8).

Although observable critical velocities may be approximated by inspection from a numerical or FSS (Appendix B.1.1), analytical expressions for these velocities emerge from the long-time asymptotic solution. All of the critical velocities can be extracted early in the process of the asymptotic analysis, but require more work to definitively determine those that lead to observable changes in solution response (observable critical velocities) and those that do not (non-observable critical velocities).

Two critical velocities can be identified immediately without additional analysis. The zero velocity, $V = 0$, delineates the upstream and downstream directions and is the location of the imposed oscillatory disturbance. The peak velocity, $V = c$, is extracted from the homogeneous form of the equation by King et al. [15] and provides the velocity of the algebraically growing peak.

In order to determine the critical velocities relevant to the signaling problem, we note that the Fourier integrals in (III.9) are of similar form, and can be written generally as:

$$Integral = \int_{-\infty}^{\infty} \frac{1}{f(k)} e^{\phi(k)t} dk. \tag{III.11}$$

In (III.11), there are a finite number of simple poles, k_i, where $f(k_i) = 0$ and some value of $k_s(V)$, which is an n^{th} order saddle point of $\phi(k)$, such that $\frac{d^{n-1}}{dk^{n-1}}(\phi)\Big|_{k_s} = 0$ and $\frac{d^n}{dk^n}(\phi)\Big|_{k_s} \neq 0$. The behavior of the integral near saddle points is relevant to the long-time asymptotic behavior via the method of steepest descents [34]. The location of the saddle point is a function of V (i.e., $k_s = k_s(V)$), indicating that any given velocity

corresponds to a saddle point. Each saddle point leads to a different arrangement of the complex contours used in the asymptotic analysis (see Appendix B.2). For a given velocity and set of parameters, the poles are either enclosed, not enclosed, or intersected by the contour. Critical velocities are extracted by finding all the real values of V where a pole of $f(k)$ intersects a contour. The simplest critical velocities to determine through are those associated with the poles that lie on the locus of saddle points, as it is simply a matter of setting $k_s(V) = k_i$ and solving for V. The velocities associated with poles that lie off the locus of saddles are more difficult to find, as they require establishing how the contours sweep through the complex k plane as shown in Appendix B.2. Note that, for (III.8), the locus of saddles lies along the entirety of the real k axis. In what follows, no distinction will be made between the "locus of saddles" and "real k axis".

Overall, then, every critical velocity (besides $V = 0$ and $V = c$) corresponds to either: (i) a change in whether a given pole is enclosed or not within a contour (going from not enclosed to enclosed or vice versa) or (ii) the situation where a saddle point and pole are coincident. As defined earlier, these velocities indicate where structural changes in the solution *could* occur at long times. Once all the critical velocities are found, they can be overlaid on a numerical solution to visually determine those which yield significant changes in the solution without having to undertake a full asymptotic analysis.

If a term in the asymptotic form associated with a critical velocity decays exponentially in time when active, then it will not have any lingering structural effect on the solution response at large times. These velocities correspond to the off-axis pole locations in Figure III.4 and are non-observable. The only observable critical velocities, then, are those associated

with the coincidence of a pole and saddle along the real k axis. In fact, it is the difference in the number of on-axis poles that accounts for the differences in the solution structure associated with the cases $\omega_f < \omega_c$ and $\omega_f > \omega_c$ configurations as will be seen.

Note that observable critical velocities are important as they delineate regions of the response where there are significant structural changes in the asymptotic response at long times. As such, observable critical velocities bound upstream and downstream regions of the response, and it is possible to identify portions of the response corresponding to transients and the oscillatory forcing. In light of comments made in the introduction regarding damage to thin film coatings, the breadth of these regions, as well as the amplitude of the response within them, is of practical relevance.

III.3.2 Approach to determine bounding amplitudes

Within each region delineated by the critical velocities of Section III.3.1, there are three potential outcomes; the disturbance grows, decays, or oscillates with a constant amplitude. At large times, the spatial resolution needed to accurately predict features of the solution is quite large (see Appendix B.1.2 for more details). As the solution has an oscillatory character in each region, a bounding amplitude enables us to determine the maximum damage to the liquid sheet without needing to obtain the full solution to the required resolution. The bounding amplitude can most certainly be extracted numerically by looking at the solution response, although this must be done individually for every set of parameters. Bounding amplitudes can be extracted analytically using the long-time asymptotic solutions and, as such, this section will provide a higher level discussion about how such amplitudes

are extracted.

To extract the amplitude of the solution within a single region between two adjacent critical velocities V_n and V_m, we note that the asymptotic solution is expressed as a sum of one or more distinct exponentials with different phases (see Sections III.3.3 and III.3.4). The general form of the asymptotic solution is written as

$$Real[h(x,t)] \sim Real\left[\sum_{n=1}^{N} \alpha_n e^{i\beta_n(V)t}\right] \quad V \in [V_n, V_m] \quad \text{as} \quad t \to \infty, \tag{III.12}$$

where α_n is some complex constant. The maximum possible amplitude ($\mathcal{A}$) of (III.12) (see Appendix B.5) can be expressed as

$$\left|Real[h(x,t)]\right| \lesssim \mathcal{A} = \sum_{n=1}^{N} \left|\alpha_n\right| \qquad V \in [V_n, V_m] \qquad \text{as} \qquad t \to \infty. \tag{III.13}$$

Using (III.13), the extracted amplitudes are obtained and reported in Sections III.3.3 and III.3.4. Note that the algebraic growth, which can occur at the velocity of $V = c$, is not considered when determining the bounding amplitudes.

III.3.3 Long-time asymptotic solution for $\omega_f < \omega_c$

Following the approach of Barlow et al. [21], a Fourier Series Solution (FSS) is used to generate Figure III.5, which provides a typical solution response for a case where $\omega_f < \omega_c$; see Appendix B.1.1 for details. Note that the large number of oscillations in the solution are not caused by numerical noise or aliasing — the solution indeed responds in this way, and when magnified in any region, is entirely smooth (see Appendix B.1.2 for additional details on resolving oscillations). Figure III.5 is presented in terms of the velocity $V \equiv {}^{x}/_{t}$

as we will see this domain provides critical insight into the structure of the solution. Note that at any time t, the V domain may be interpreted as being simply a rescaling of x; the V domain has the advantage that the structural features are kept stationary in time for a fixed V domain.

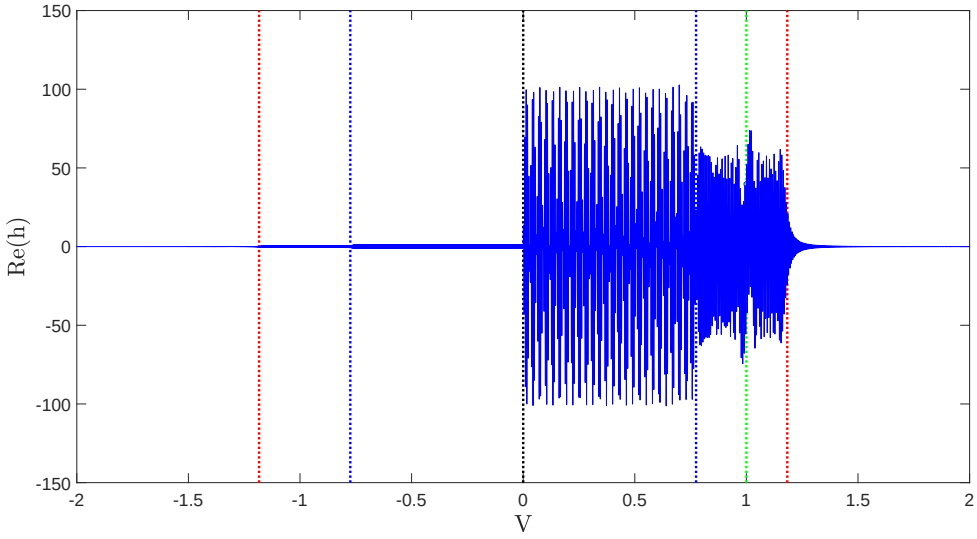

Figure III.5: Fourier Series Solution (Appendix B.1.1) for $\omega_f < \omega_c$ and $t = 10000$ with $A_f = 1$, $\omega_f = 0.1$, $B = 1$, $c = 1$, and $L = N = 100000$. Observable critical velocities are marked with dotted vertical lines (see Section III.3.1 for more details). Results are plotted against V in order to capture the critical velocities and separate regions.

When viewing the solution in terms of V, the frequencies of the oscillations increase with time; as more and more wave cycles are crammed into a fixed range of V, the density of the wave cycles increases, leading to solutions which appear to be rectangular blocks (Figures III.5 and III.7). It is important to remember, however, that the region between any two velocities V_n and V_m at time t covers a spatial distance of $(V_m - V_n)t$ and thus expands with time. If we look at a fixed value of t, V is a direct scaling of x for the entire

domain. If we look at a fixed point in x, however, the point will move towards smaller and smaller V values as time progresses. For any non-zero x location, small times correspond to large magnitudes of V. As t increases, the magnitude of V decreases until the x location sees a change in structure at an observable critical velocity. As t continues to increase and approaches infinity, the magnitude of V approaches zero for the x location. Therefore, the long-time solution for any finite x value may be deduced based on the behavior of the solution near $V = 0$ where there are no further transitions in structure across critical velocities.

Applying the methodology from Sections III.3.1 and III.3.2 to the long-time asymptotic solution (see Appendix B.3) leads to analytical expressions for the solution response, bounding amplitudes of each region, and the associated critical velocities that separate them. The results are:

$$V_1 = -\sqrt{c^2 + 4B\omega_f}, \quad V_2 = -\sqrt{c^2 - 4B\omega_f},$$

$$V_3 = \sqrt{c^2 - 4B\omega_f}, \quad V_4 = \sqrt{c^2 + 4B\omega_f}. \tag{III.14}$$

For the $\omega_f < \omega_c$ case, the leading-order behaviors within each of the six regions are as follows:

$\underline{-\infty < V < V_1 \qquad t \to \infty}$:

$$h \sim O\left(t^{-\frac{1}{2}}\right),$$

$$\mathcal{A}_{(\omega_f < \omega_c)} = 0. \tag{III.15a}$$

$\underline{V_1 < V < V_2 \qquad t \to \infty:}$

$$h \sim -i\frac{A_f}{B^2}\frac{e^{i\omega_f t}e^{ik_3 Vt}}{(k_3-k_0)(k_3-k_1)(k_3-k_2)},$$

$$\mathcal{A}_{(\omega_f<\omega_c)} = \frac{A_f}{B^2}\left|\frac{1}{(k_3-k_0)(k_3-k_1)(k_3-k_2)}\right|. \tag{III.15b}$$

$\underline{V_2 < V < 0 \qquad t \to \infty:}$

$$h \sim -i\frac{A_f}{B^2}\frac{e^{i\omega_f t}e^{ik_3 Vt}}{(k_3-k_0)(k_3-k_1)(k_3-k_2)} - i\frac{A_f}{B^2}\frac{e^{i\omega_f t}e^{ik_0 Vt}}{(k_0-k_1)(k_0-k_2)(k_0-k_3)},$$

$$\mathcal{A}_{(\omega_f<\omega_c)} = \frac{A_f}{B^2}\left[\left|\frac{1}{(k_3-k_0)(k_3-k_1)(k_3-k_2)}\right| + \left|\frac{1}{(k_0-k_1)(k_0-k_2)(k_0-k_3)}\right|\right]. \tag{III.15c}$$

$\underline{0 < V < V_3 \qquad t \to \infty:}$

$$h \sim i\frac{A_f}{B^2}\frac{e^{i\omega_f t}e^{ik_2 Vt}}{(k_2-k_0)(k_2-k_1)(k_2-k_3)} - i\frac{A_f}{B^2}\frac{e^{i\omega_f t}e^{ik_1 Vt}}{(k_1-k_0)(k_1-k_2)(k_1-k_3)},$$

$$\mathcal{A}_{(\omega_f<\omega_c)} = \frac{A_f}{B^2}\left[\left|\frac{1}{(k_2-k_0)(k_2-k_1)(k_2-k_3)}\right| + \left|\frac{1}{(k_1-k_0)(k_1-k_2)(k_1-k_3)}\right|\right]. \tag{III.15d}$$

$\underline{V_3 < V < V_4 \qquad t \to \infty:}$

$$h \sim i\frac{A_f}{B^2}\frac{e^{i\omega_f t}e^{ik_2 Vt}}{(k_2-k_0)(k_2-k_1)(k_2-k_3)},$$

$$\mathcal{A}_{(\omega_f<\omega_c)} = \frac{A_f}{B^2}\left|\frac{1}{(k_2-k_0)(k_2-k_1)(k_2-k_3)}\right|. \tag{III.15e}$$

$\underline{V_4 < V < \infty \qquad t \to \infty:}$

$$h \sim O\left(t^{-\frac{1}{2}}\right),$$

$$\mathcal{A}_{(\omega_f<\omega_c)} = 0. \tag{III.15f}$$

Higher order asymptotic corrections to (III.15) can be found in Appendix B.3, and the poles k_0 through k_3 are defined in (III.9d). A detailed examination of the precise response in each region (i.e., the solutions for h in (III.15)) is provided in Section III.4.1 to follow.

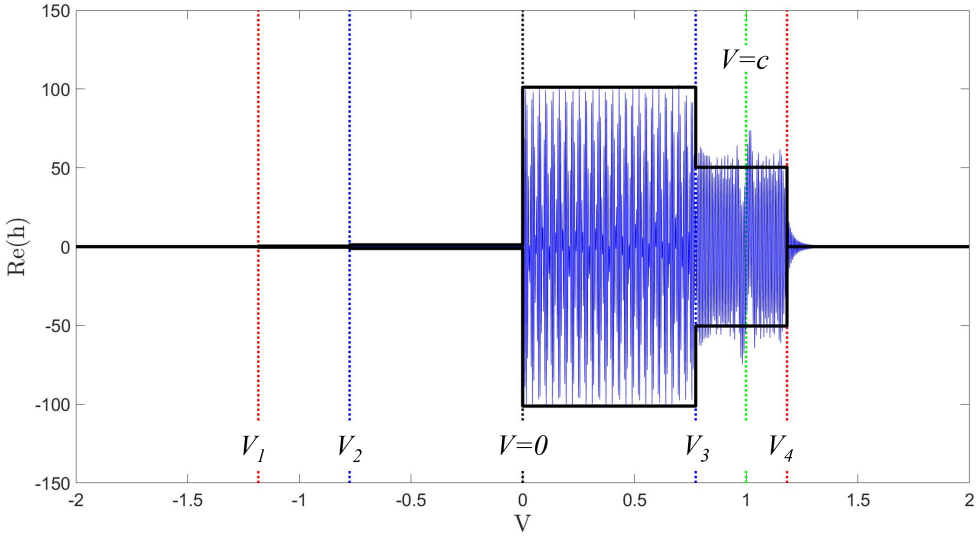

Figure III.6: Bounding amplitudes overlaid on the Fourier series solution in Figure III.5. Critical velocities are marked with dotted vertical lines. The observable critical velocities from (III.14) are labeled.

Figure III.6 overlays the amplitude/critical-velocity asymptotic results on Figure III.5. As indicated, the bounding amplitudes and delineated regions agree well with the FSS (Appendix B.1.1) results except near $V = c = 1$ and near the critical velocities. This discrepancy is due to the data being generated for finite times and nonuniform asymptotic limits as will be discussed in Section III.4 below. This agreement is seen over a wide range of analogous plots. Thus, we conclude that the amplitude and breadth of each region is well-represented by the asymptotically extracted results. Note that, if A_f is chosen to be purely real, as it is in Figures III.5 and III.6, there is no algebraic growth at $V = c$. The algebraic growth

occurs only in the imaginary part of h, which can only be accessed in the real part of the solution is A_f is complex (see the end of Appendix B.3).

III.3.4 Long-time asymptotic solution for $\omega_f > \omega_c$

The FSS (Appendix B.1.1) is used to generate Figure III.7 which provides a typical solution response for a case where $\omega_f > \omega_c$. More so than the $\omega_f < \omega_c$ case just considered, there are a large number of oscillations present in the solution. At large times, in fact, the solution appears to be a solid block as indicated, but the solution is completely smooth and oscillatory upon magnification. There are four regions of distinctly different amplitudes, and the observable critical velocities derived using the above-described algorithm delineate discrete regions. As discussed in Section III.3.3, Figure III.7 is presented in terms of V instead of x to better capture the long-time behavior.

Applying the methodology from Sections III.3.1 and III.3.2 to the results from Appendix B.4 leads to a solution for each region of the solution. The regions are separated by the critical velocities

$$V_1 = -\sqrt{c^2 + 4B\omega_f}, \quad V_4 = \sqrt{c^2 + 4B\omega_f}, \tag{III.16}$$

which are precisely the same as for V_1 and V_4 in the $\omega_f < \omega_c$ case in III.14. The velocities V_2 and V_3 correspond to the poles k_0 and k_1 in Figure III.4, but do not contribute to the long-time behavior — the off-axis poles add contributions that damp with time. The poles lying off the real k axis accounts for the change in number of regions between the $\omega_f < \omega_c$ and $\omega_f > \omega_c$ cases.

The leading-order asymptotic behaviors within each of the four regions are as follows:

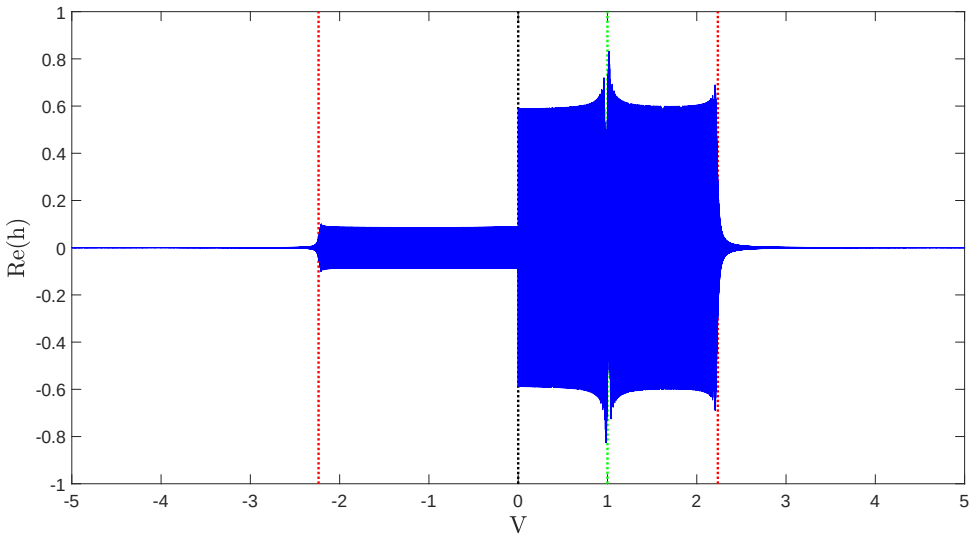

Figure III.7: Fourier series solution (Appendix B.1.1) for $\omega_f > \omega_c$ and $t = 10000$ with $A_f = 1$, $\omega_f = 1$, $B = 1$, $c = 1$, and $L = N = 100000$. Critical velocities are marked with dotted vertical lines. Results are plotted against V in order to capture the critical velocities and separate regions.

$-\infty < V < V_1 \qquad t \to \infty$:

$$h \sim O\left(t^{-\frac{1}{2}}\right),$$

$$\mathcal{A}_{(\omega_f > \omega_c)} = 0. \tag{III.17a}$$

$V_1 < V < 0 \qquad t \to \infty$:

$$h \sim -i\frac{A_f}{B^2}\frac{e^{i\omega_f t}e^{ik_3 Vt}}{(k_3-k_0)(k_3-k_1)(k_3-k_2)},$$

$$\mathcal{A}_{(\omega_f > \omega_c)} = \frac{A_f}{B^2}\left|\frac{1}{(k_3-k_0)(k_3-k_1)(k_3-k_2)}\right|. \tag{III.17b}$$

$0 < V < V_4 \qquad t \to \infty$:

$$h \sim i\frac{A_f}{B^2}\frac{e^{i\omega_f t}e^{ik_2 Vt}}{(k_2-k_0)(k_2-k_1)(k_2-k_3)},$$

$$\mathcal{A}_{(\omega_f>\omega_c)} = \frac{A_f}{B^2}\left|\frac{1}{(k_2-k_0)(k_2-k_1)(k_2-k_3)}\right|. \tag{III.17c}$$

$V_4 < V < \infty$ and as $t \to \infty$:

$$h \sim O\left(t^{-\frac{1}{2}}\right),$$

$$\mathcal{A}_{(\omega_f>\omega_c)} = 0. \tag{III.17d}$$

Higher order corrections to (III.17) can be found in Appendix B.4, and the poles k_0 through k_3 are defined in (III.9d). A detailed examination of the precise response in each region (i.e., the solutions for h in (III.17)) is given Section III.4.2.

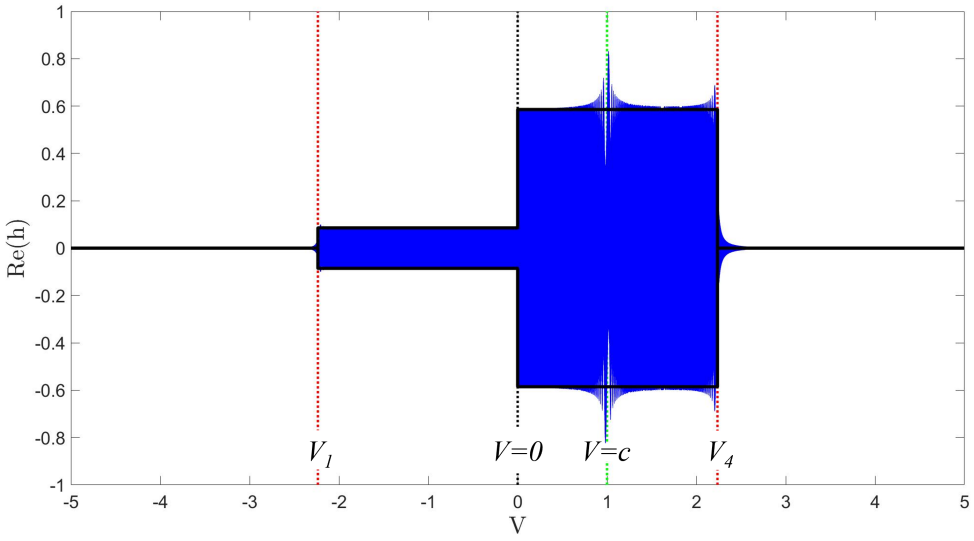

Figure III.8: Bounding amplitudes overlaid on the Fourier series solution (Appendix B.1.1) in Figure III.7. Critical velocities are marked with dotted vertical lines. The observable critical velocities from (III.16) are labeled.

Figure III.8 overlays the amplitude/critical-velocity asymptotic results on Figure III.7. As with the previous case of $\omega_f < \omega_c$, the bounding amplitudes and delineated regions agree

well with the numerical results except near $V = c = 1$ and near the critical velocities (these discrepancies will be discussed in Section III.4). Thus, we conclude that the amplitude and breadth of each region is well-represented by the asymptotically extracted results. As with the $\omega_f < \omega_c$ case previously considered, if A_f is chosen to be purely real, as it is in Figures III.7 and III.8, there is no algebraic growth at $V = c$. The algebraic growth occurs only in the imaginary part of h as shown at the end of Appendix B.4. A complex A_f is needed to access growth in the real solution.

III.4. Results

In the what follows, we present the results for the $\omega_f < \omega_c$ and $\omega_f > \omega_c$ cases. Just as with Figures III.6 and III.8, the V domain is used instead of x as discussed in Section III.3.3. Note that the qualitative features shown in Figures III.6 and III.8 are observed for all surveyed parameter values (see Appendix B.5 for parameter ranges). Although the exact amplitudes and critical velocities can vary, the amplitude proportions are maintained. Although the quantitative ratio of heights between regions may change, the fact that one region has a larger (or smaller) amplitude than another never does.

III.4.1 Details of solution response for $\omega_f < \omega_c$

Thus far, we have examined the efficacy of critical velocities and bounding amplitudes in characterizing the solution response provided in Figure III.6. We now examine the details of the solution response for $\omega_f < \omega_c$ given by (III.10), specifically focusing on the wave forms in each delineated region. To this end, the apparent distinct regions of the response delineated

by amplitudes/critical-velocities in Figure III.6 are labeled for reference in Figure III.9. The labeling convention is chosen to aid in the comparison to the $\omega_c > \omega_f$ case later. Upstream ($V < 0$) and downstream ($V > 0$) of the disturbance location ($V = 0$), regions are grouped into pairs which exhibit similar behavior. These groups are the *Asymptotically Undisturbed Regions* (A and D), the *Forced Regions* (B and C), and the *Additionally Forced Regions* (B_2 and C_2).

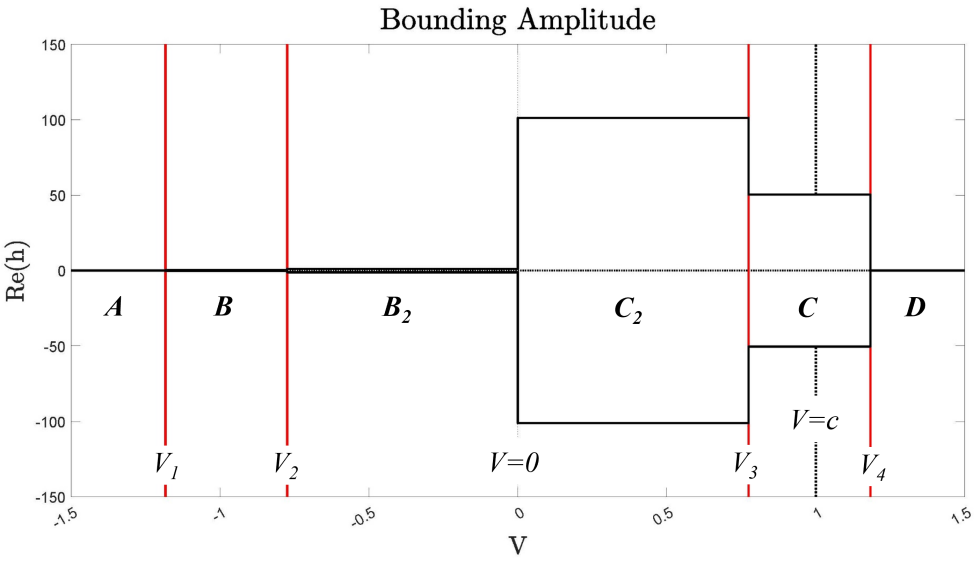

Figure III.9: Infinite-time bounding amplitude of the solution, $h(x,t)$, plotted against the velocity for $\omega_f < \omega_c$. The velocities V_2 and V_4 are the *Leading Edges of the Forced Solution*. The velocities V_2 and V_4 are the *Leading Edges of the Additionally Forced Solutions*. Regions A and B are the *Asymptotically Undisturbed Regions*, B and C are the *Forced Regions*, and B_2 and C_2 are the *Additionally Forced Regions*. The data was generated using $\omega_f = 0.1$, $A_f = 1$, $B = 1$, and $c = 1$. The vertical line at $V = c = 1$ represents the location of the algebraically growing peak, if one were to occur. The observable critical velocities, V_1 through V_4 are given by (III.14).

The results are presented from the outermost regions to the innermost regions. This order

is consistent with the physical response as it sweeps through the domain, as it is the order in which any point fixed in x will move through the regions. In particular, for any x at small time, the magnitude of V is large, but as time goes on, the magnitude of V gets smaller. Note from (III.15) that the upstream and downstream solutions have similar forms. As such, the distinction between upstream and downstream is largely ignored except for the case of $V = c$ which is addressed in Section III.4.1.7.

III.4.1.1 *Asymptotically Undisturbed Regions* (Regions A and D in Figure III.9)

The *Asymptotically Undisturbed Regions*, labeled A and D in Figure III.9, are magnified in Figure III.10. These regions are in advance of any structural features brought about by the forcing which persist at long time. There are transient responses in the region which decay in time (III.15a)(III.15f), but there no persistent oscillatory behavior induced by the forcing function (none of the poles indicated in Figure III.3 are enclosed in relevant contours — see Appendix B.3).

In Figure III.10 it is worth noting that, while the numerical solution (○) matches the asymptotic solution (blue lines), neither one has reached the long-time amplitude of zero (solid horizontal lines in the sub-plots). The indicated solutions are shown at a time of $t = 10000$; the solution does tend towards zero as time goes off to infinity in accordance with the bounding amplitudes and asymptotic behaviors in (III.15).

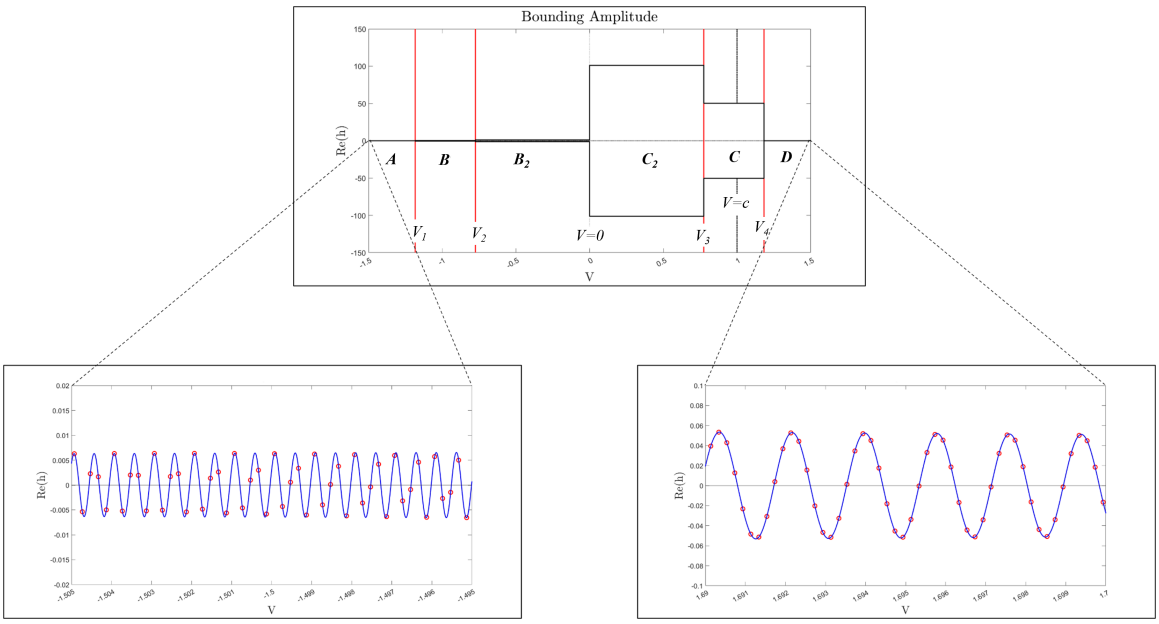

Figure III.10: Magnified view of the response in the *asymptotically undisturbed regions* A (left) and D (right) of Figure III.9 at $t = 10000$ with $\omega_f = 0.1$, $B = 1$, $c = 1$, $L = 50000$, and $N = 10000$. The FSS (Appendix B.1.1) (○) agrees with the long-time asymptotic solution (Appendix B.3) (blue curve). Bounding amplitudes and leading order asymptotic solutions are given in (III.15)

III.4.1.2 *Leading Edges of the Forced Solution* (V_1 and V_4 in Figure III.9)

The critical velocities V_1 and V_4 in Figure III.9 represent the leading edges of the forcing's effect in the upstream and downstream directions at long times, respectively; these regions are magnified in Figure III.11. There is a non-zero bounding amplitude according to Equations (III.15b) and (III.15e) for $V_1 < V < V_3$ and $V_2 < V < V_4$. These velocities mark where the poles k_2 and k_3 (Figure III.3) are enclosed in the integration contours (see Appendix B.3).

As indicated in Figure III.11, the FSS (Appendix B.1.1) is continuous across V_1 and V_4, but

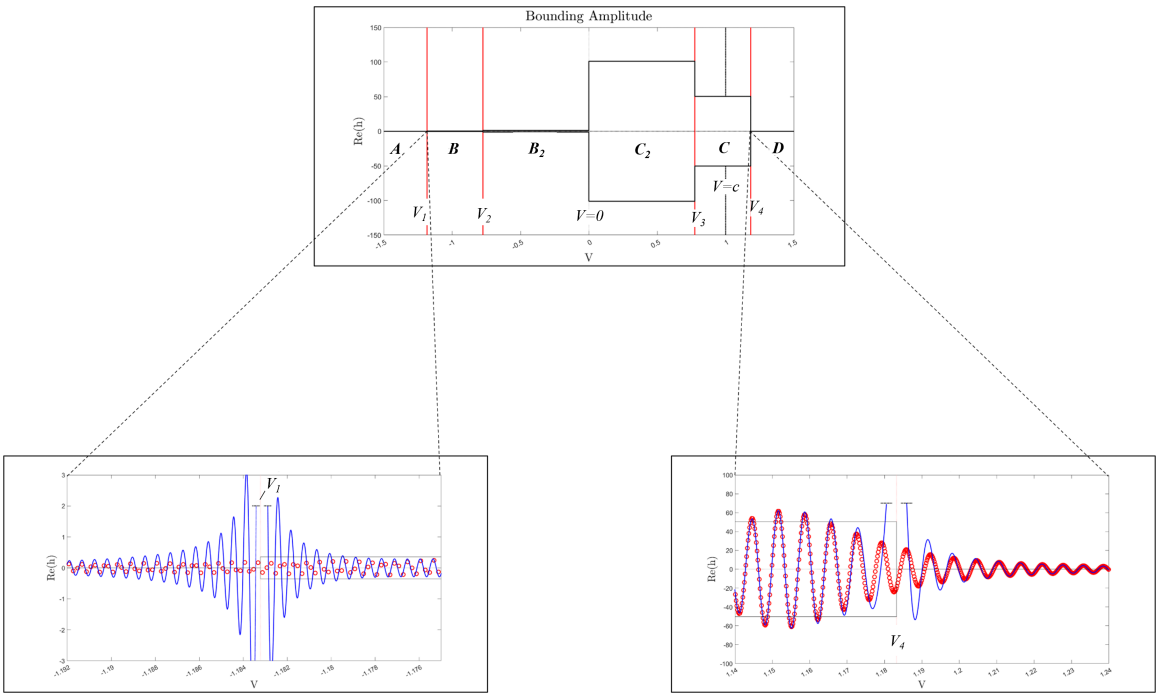

Figure III.11: Magnified view of the response near the *Leading Edge of the Forced Solution* of Figure III.9 at $t = 10000$ with $\omega_f = 0.1$, $B = 1$, $c = 1$, $L = 50000$, and $N = 10000$. The FSS (Appendix B.1.1) (○) agrees with the long-time asymptotic solution (Appendix B.3) (blue curve) away from the discontinuities located at the critical velocities. Note that this data was generated with the full asymptotic form from Appendix B.3, not the leading order form given by (III.15). Bounding amplitudes and leading order asymptotic solutions are given in (III.15)

the asymptotic solution diverges. This is consistent with the residual singularities present in the asymptotic results (III.15). Away from the critical velocity, the long-time asymptotic solution (III.15) agrees well with the numerical solution. The tapered shape of the curve is due to the data being generated at a finite time. As time goes on, the transition becomes more pronounced (not picture here) as the amplitudes of the *Asymptotically Undisturbed Regions* (A and D) go to zero and the amplitudes of the *Forced Regions* (B and C) tend to

the long-time bounding amplitude (black lines).

III.4.1.3 *Forced Regions* (Regions B and C in Figure III.9)

Regions B and C in Figure III.9 are each influenced by the contributions of a single pole each (see (III.15b) and (III.15e)). Magnifications of these regions are provided in Figure III.12. In these regions, any point in the x domain will be reside in either region for only a finite time interval, as $V \equiv x/t$ continues to be reduced in time for a fixed x. The sampling frequency of the numerical solution appears lower in the upstream sub-plot of Figure III.12, but that is because the V axis scale is magnified further than for the other sub-plot in order to resolve the high frequency oscillations.

The two lower sub-plots within Figure III.12 show the response within the downstream *Forced Region* on either side of and away from the critical velocity $V = c$. That velocity is always contained within region C because $V_3 = \sqrt{c^2 + 4B\omega_f} > c$ and $V_4 = \sqrt{c^2 - 4B\omega_f} < c$. Other than $V = c$, the asymptotic solution (III.15) matches the FSS (Appendix B.1.1). Because the solutions are shown for a time of $t = 10000$, their amplitudes do not precisely match the predicted long-time amplitude (the solid black lines) from (III.15b); however, they approach the predicted bounding values as time goes to infinity.

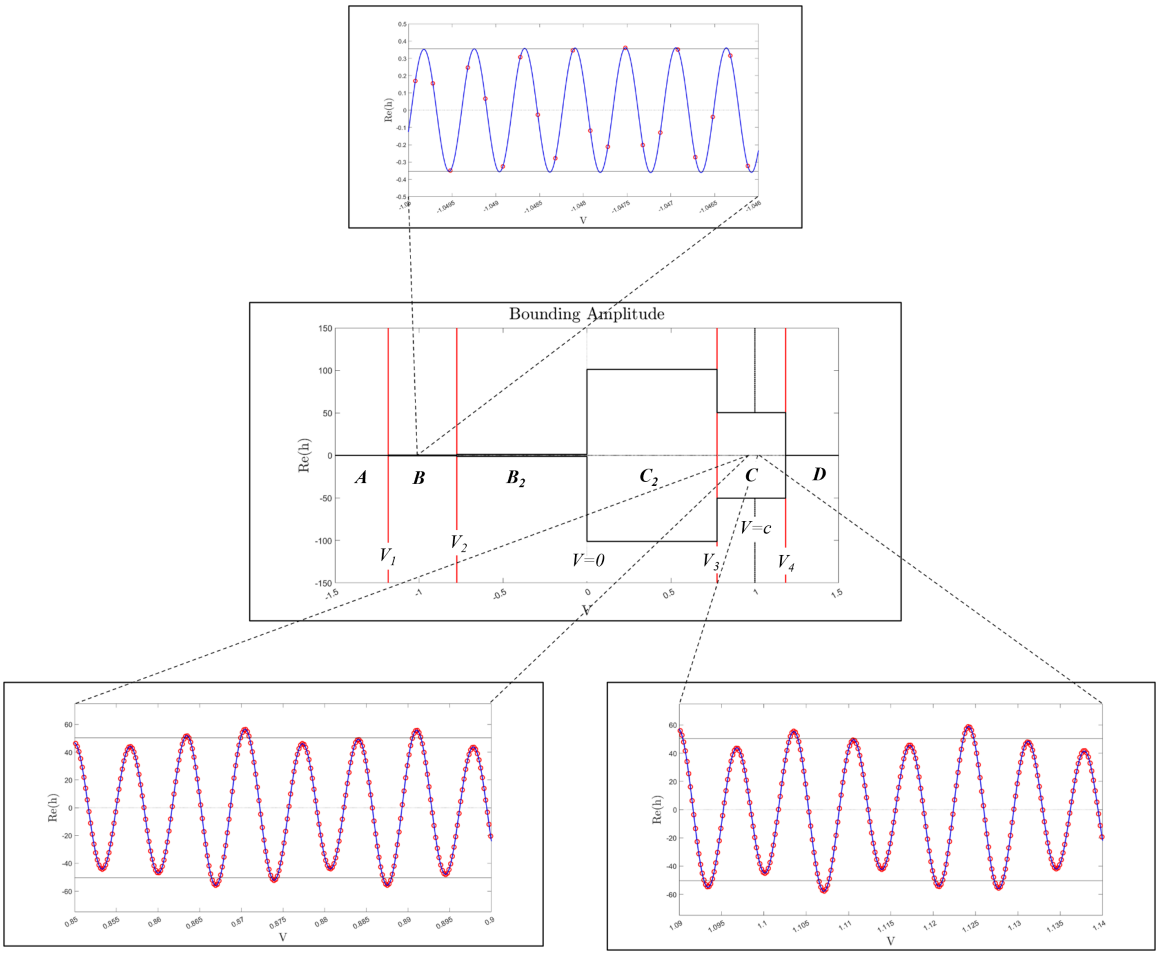

Figure III.12: Magnified view of the response in the *Forced Regions* B (top) and C (bottom) of Figure III.9 at $t = 10000$ with $\omega_f = 0.1$, $B = 1$, $c = 1$, $L = 50000$, and $N = 10000$. The FSS (Appendix B.1.1) (○) agrees with the long-time asymptotic solution (Appendix B.3) (blue curve). For the downstream behavior, the two sub-plots show the response on either side of $V = c$, which is the velocity of the growing peak if one were to occur for complex A_f as show in Appendix B.3. All the FSS data were generated with the same sampling frequency in V; the apparent difference in the plots arises because the upstream sub-plot is magnified further to resolve the waveform. Bounding amplitudes and leading order asymptotic solutions are given in (III.15).

III.4.1.4 *Leading Edges of the Additionally Forcing Regions* (V_2 and V_3 in Figure III.9)

The critical velocities V_2 and V_3 in Figure III.9 mark the *Leading Edges of the Additional Forcing Regions*; these transitions are magnified in Figure III.13. This boundary also represents the leading edge of the long-time solution over any finite physical domain (in x), that is to say the effect of the other regions has swept through, leaving only oscillations from the forcing.

As mentioned previously, the long-time asymptotic solution diverges near the critical velocities due to residual singularities in terms which decay in time (see Appendix B.3 for this case and Appendix B.4 for the $\omega_f > \omega_c$ case). On either side of these discontinuities, the FSS and asymptotic solutions match well. Again, any discrepancies between the bounding amplitudes, indicated on the plots, disappear as t gets larger. The high frequency of oscillations upstream make the comparison between the long-time asymptotic solution (III.15) and the FSS (Appendix B.1.1) difficult to resolve on a single plot.

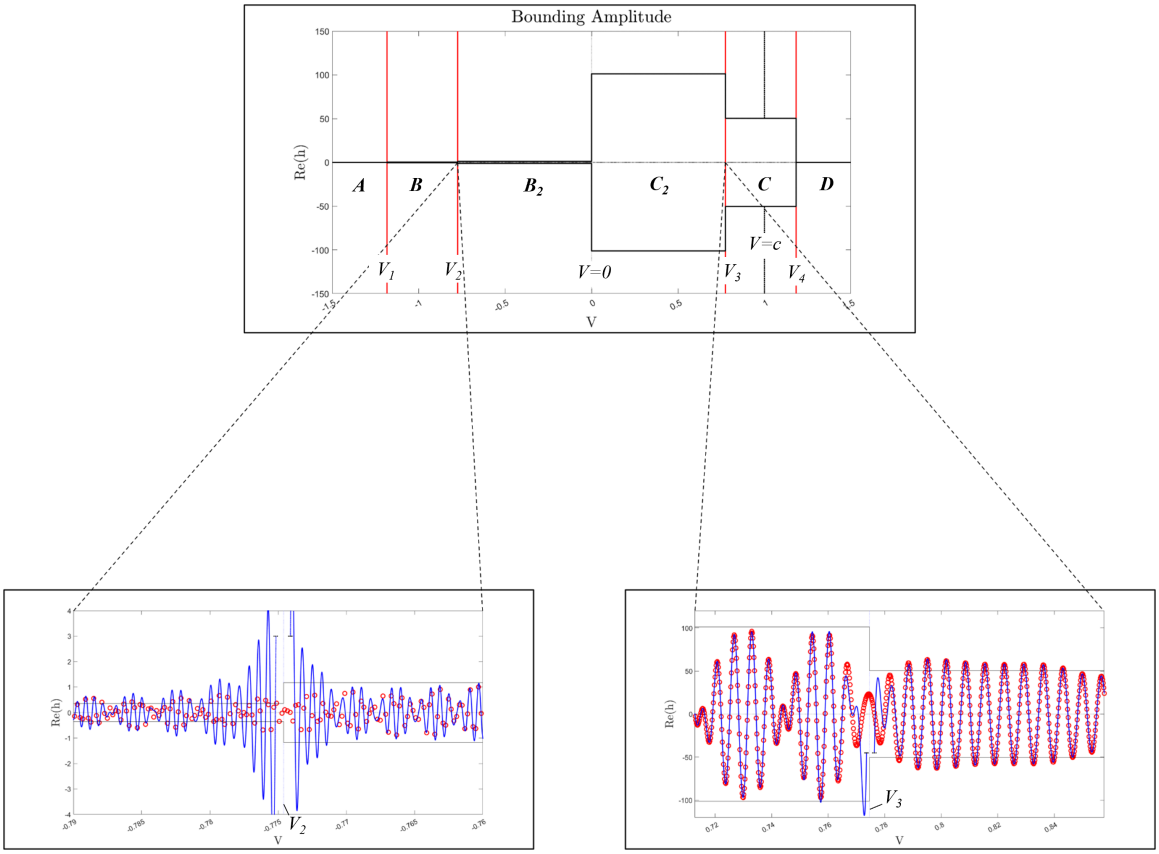

Figure III.13: Magnified view of the response near the *Leading Edges of the Additional Forcing Regions* of Figure III.9 at $t = 10000$ with $\omega_f = 0.1$, $B = 1$, $c = 1$, $L = 50000$, and $N = 10000$. The FSS (Appendix B.1.1) (○) agrees with the long-time asymptotic solution (Appendix B.3) (blue curve) away from the discontinuity directly at the critical velocity. Note that this data was generated with the full asymptotic form from Appendix B.3, not the leading order form given by (III.15). Bounding amplitudes and leading order asymptotic solutions are given in (III.15)

III.4.1.5 *Additionally Forced Regions* (Regions B_2 and C_2 in Figure III.9)

The regions B_2 and C_2 in Figure III.9 are the *Additionally Forced Regions* of the solution and represent the long-time response over any finite x domain; given enough time, any point

in the x domain will be affected by one of the two, as there are no further structural changes in solution possible as V approaches zero in Figure III.9 (as t goes to infinity for a fixed x, V goes to zero). Figure III.14 shows the agreement between the long-time asymptotic solution (III.15) and the FSS (Appendix B.1.1) away from the bounding velocities V_2 and V_3 from (III.14) discussed in Section III.4.1.4 and $V = 0$ discussed in Section III.4.1.6.

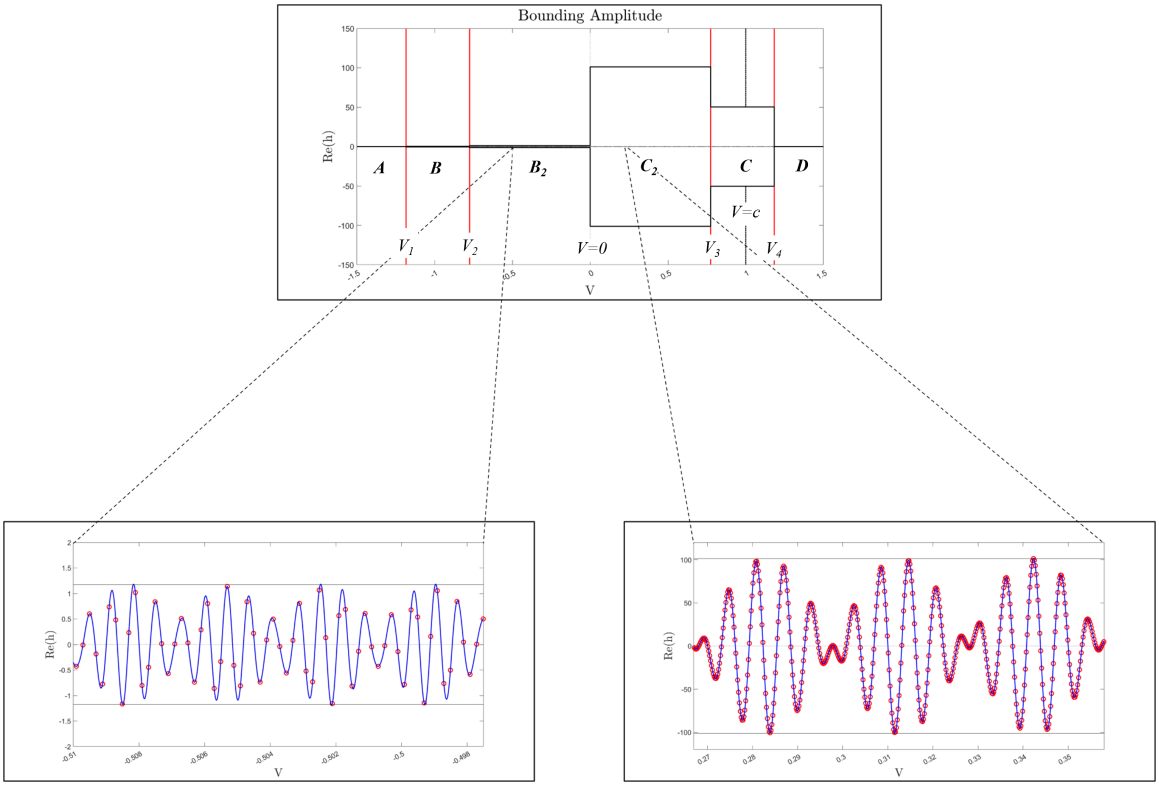

Figure III.14: Magnified view of the response in the *Long-Time Forced Regions* B_F (left) and C_f (right) of Figure III.9 at $t = 10000$ with $\omega_f = 0.1$, $B = 1$, $c = 1$, $L = 50000$, and $N = 10000$. The FSS (Appendix B.1.1) (○) agrees with the long-time asymptotic solution (Appendix B.3)(blue curve). All the FSS data were generated with the same sampling frequency in V. Note that the upstream (left) sub-plot is magnified more than the downstream sub-plot in order to resolve the waveform. Bounding amplitudes and leading order asymptotic solutions are given in (III.15)

Region B and B_2 are both influenced by the pole k_3 (see (III.15b) and (III.15c)), but B_2 also contains the influence of the pole k_0. The same holds true for C and C_2 and the poles k_2 and k_1. The overall structure of the solution in regions B_2 and C_2 is that of two oscillatory modes with different frequencies which travel at two different speeds.

Within the regions B_2 and C_2, the asymptotic solution agrees with the FSS. The velocity sampling frequency of both plots are the same (data points per velocity range). Region B has much higher frequency oscillations, so it requires much higher magnification to resolve. The vertical scales differ between the sub-plots by two orders of magnitude. Both regions demonstrate a beat-like structure with a much lower frequency.

It is important to differentiate here between the long-time solution in V and the long-time solution in x. To determine the overall behavior, all values of V are studied as they are relevant to the structure of the solution. However, for any finite x domain, regions B_2 and C_2 represent the final signaling response as they will persist for all time at any given x (i.e., V approaches zero in Figure III.9).

III.4.1.6 *Upstream/Downstream Division* ($V = 0$ in Figure III.9)

The critical velocity $V = 0$ separates the upstream and downstream behavior of the response. It is the only critical velocity across which the long-time asymptotic solution (III.15) is continuous. As with all the other transitions in the various regions of Figure III.9, the FSS (Appendix B.1.1) is continuous. The region near this velocity is magnified in Figure III.15.

As shown in Section III.4.1.5, the response in the upstream and downstream forced regions

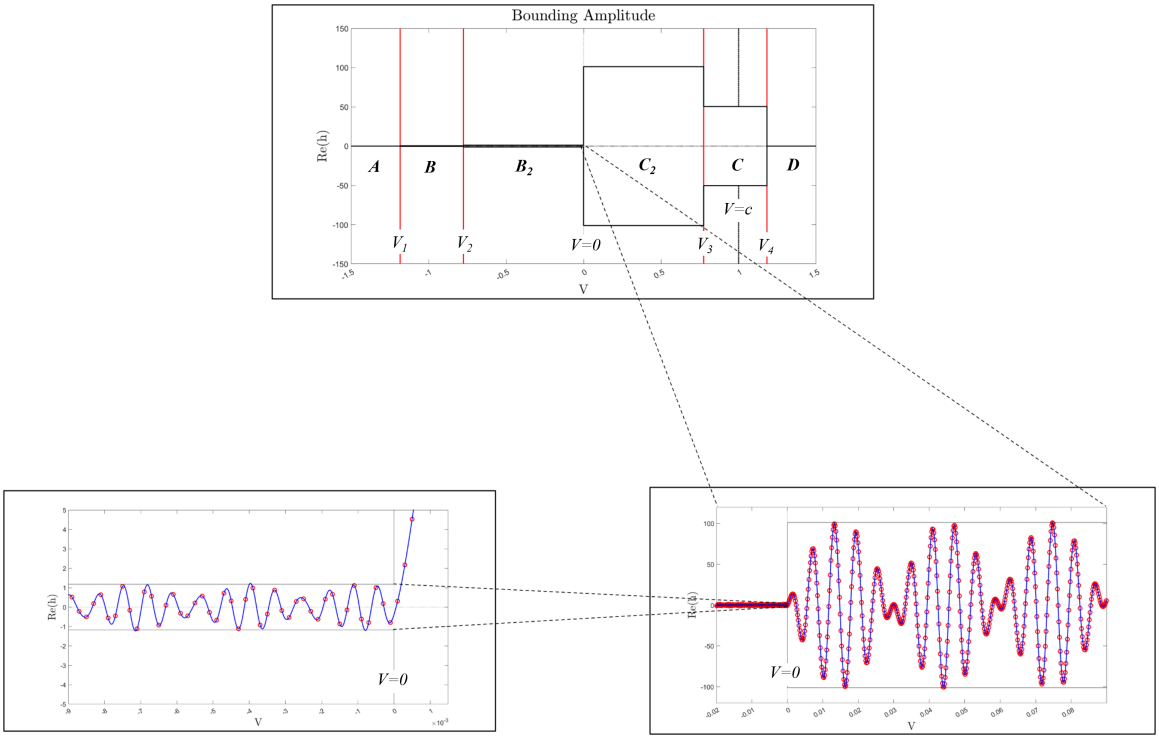

Figure III.15: Magnified view of the response at the *Upstream/Downstream Division* of Figure III.9 at $t = 10000$ with $\omega_f = 0.1$, $B = 1$, $c = 1$, $L = 50000$, and $N = 10000$. The FSS (Appendix B.1.1) (○) agrees with the long-time asymptotic solution (Appendix B.3) (blue curve). Note that this data was generated with the full asymptotic form from Appendix B.2, not the simplified form given by (III.15). All the FSS data were generated with the same sampling frequency in V; the apparent difference in the plots (the spread in the circles for FSS data points) arises because the upstream sub-plot is magnified much further to resolve the waveform. Due to a significant difference in amplitudes, the sub-plot for the upstream response is a further magnification from the downstream sub-plot. Bounding amplitudes and leading order asymptotic solutions are given in (III.15)

have the same structure, albeit at vastly different scales. The disparities in amplitude and frequency make it impossible to plot the responses of both regions on a single scale. As such, Figure III.15 includes two levels of magnification levels, one to show the downstream behavior (right) and another to show the upstream behavior (left).

III.4.1.7 Velocity of algebraic growth ($V = c$ in Figure III.9)

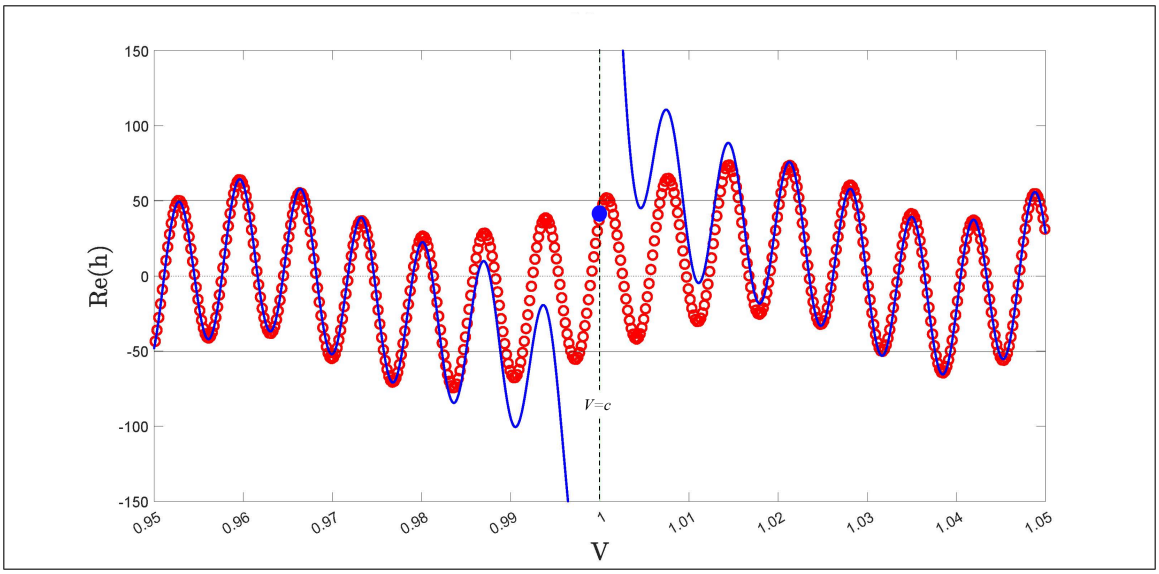

Figure III.16: Magnified view of the response near $V = c$ at $t = 10000$ with $\omega_f = 0.1$, $B = 1$, $c = 1$, $L = 50000$, and $N = 10000$. The FSS (Appendix B.1.1) (○) agrees with the long-time asymptotic solution (Appendix B.3) (blue curve) away from the discontinuity directly at the critical velocity. Note that this data was generated with the full asymptotic form from Appendix B.2, not the simplified form given by (III.15). Unlike for the other critical velocities, there is an exact solution (●) for $V = c$. Bounding amplitudes and leading order asymptotic solutions are given in (III.15)

Near the critical velocity of $V = c$, the long-time asymptotic solution (III.15) diverges from

the FSS (Appendix B.1.1). This divergence arises from the non-uniform limit taken in the asymptotic expansion, which is expressed as $(V-c)t$ goes to infinity instead of just t going to infinity. As such, longer and longer times are needed to properly resolve the behavior near $V=c$. The integrals which cause the divergence are solvable in closed form at $V=c$, leading to a non divergent solution, marked in Figure III.16 at $V=1$. On either side of the critical velocity, the asymptotic solution agrees with the FSS, as shown in the plots in Figure III.12.

The structure of the solution at $V=c$ depends on the phase of the initial disturbance. This dependence is analogous to that found by King et al. [15] where the growth occurs if the initial surface velocity is perturbed but not when the initial surface height is perturbed. In the forced problem, the phase of the growth is controlled by the phase of the forcing amplitude, A_f. Choosing A_f to be real keeps all the growth out of the real part of $h(x,t)$, equivalent to suppressing the initial surface velocity in the unforced problem of King et al. (see III.7)). In the unforced problem, the magnitude of the growth integral is controlled by U_0, the initial surface velocity. Ultimately, the response at $V=c$ is a transient solution created by the start-up of the disturbance. As such, it is separate from the long-time oscillatory solution in each region. The overall long-time asymptotic solution is the superposition of the oscillatory terms and this transiently growing and convecting $V=c$ peak.

III.4.2 Details of solution response for $\omega_f > \omega_c$

The FSS (Appendix B.1.1) is used to generate Figure III.7 for the case where the forcing frequency is above the critical value. Above the critical frequency, ω_c given in (III.10), the solution has a similar structure as the $\omega_f < \omega_c$ case. As the forcing frequency is increased towards the critical frequency in Figure III.9, the velocities V_2 and V_3 move towards $V = 0$. Across the critical frequency, the regions B_2 and C_2 collapse, leaving only the regions B and C as shown in Figure III.17. Additional details on this transition are included in Section III.5.

One feature of the solution for $\omega_f > \omega_c$ is that the oscillation frequencies in the response are much higher than those for $\omega_f < \omega_c$, and thus significant magnification is needed to observe individual wave-forms and transitions between regions. The same qualitative features of the solution are seen across bounding velocities — the FSS (Appendix B.1.1) is always continuous and smooth, the asymptotic solution agrees with the FSS away from critical velocities (but not close to them), and discontinuities across critical velocities can be observed in some transitions between regions. In what follows, we discuss the physics of these regions in a more abbreviated form, comparing and contrasting with the $\omega_f < \omega_c$ case discussed in Section III.4.1.

The long-time *Forced Solution* near $V = 0$ corresponds to the regions B and C in Figure III.17; this differs from the $\omega_f < \omega_c$ case, where regions B_2 and C_2 formed the long time amplitude. As mentioned before, Figure III.17 has fewer distinct regions than Figure III.9. Due to the collapse of V_2 and V_3 as ω_f transitions past ω_c, the $\omega_f > \omega_c$ case has no

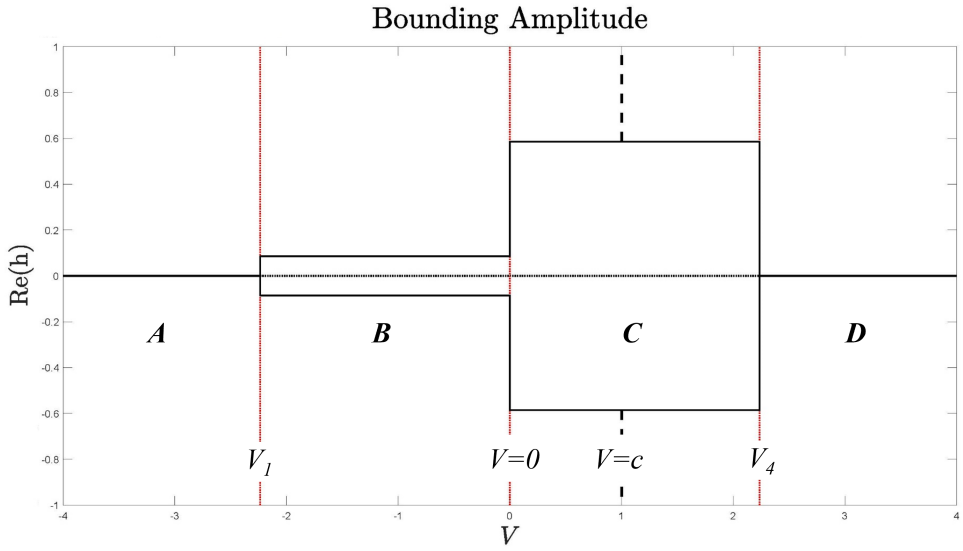

Figure III.17: Infinite time bounding envelope of the solution, $h(x,t)$ given by (III.17), plotted against the velocity for $\omega_f > \omega_c$. The velocities V_1 and V_4 are the *Leading Edge of the Forced Solution*. Regions A and D are the *Asymptotically Undisturbed Regions*, and B and C (excluding $V = c$) are the *Forced Solutions*. The data was generated using $\omega_f = 1$, $A_f = 1$, $B = 1$, and $c = 1$. The vertical line at $V = c = 1$ represents the location of the growing peak, if one occurs.

equivalent regions to B_2 and C_2 as for the $\omega_f < \omega_c$ case (compare Figures III.9 and III.17). This difference is also seen by inspection of the asymptotic forms and bounding amplitudes for the $\omega_f < \omega_c$ and $\omega_f > \omega_c$ cases given by (III.15) and (III.17), respectively; it can be seen that the *Forced Regions* of both cases are the result of the contributions of a single pole each, k_3 in the upstream regions and k_2 in the downstream regions (see Figure III.3 for pole structure).

As with the case where $\omega_f < \omega_c$, the outer regions A and D in Figure III.17 are the *Asymptotically Undisturbed Regions* that limit to zero amplitude as t approaches infinity.

The critical velocity of $V = 0$ divides the upstream and downstream behavior as before. Across this velocity, both the numerical and asymptotic solutions are continuous and the solutions have different frequencies and amplitudes on either side as for $\omega_f < \omega_c$. Similarly to the $\omega_f < \omega_c$ results, the asymptotic solution and numerical solution disagree near the critical velocity of $V = c$; however, in this case, it is for a different reason. For $\omega_f > \omega_c$, the FSS and asymptotic solutions agree when $V = c$, and this is true for nearby velocities as well. In the $\omega_f < \omega_c$ case, however, the asymptotic solution diverges for velocities near $V = c$ due to the nonumiformity of the large time limit (see Section III.4.1.7 above). The reason for this behavior difference is that the real part of the solution does not diverge when $\omega_f > \omega_c$; it is the *imaginary* part which demonstrates similar divergence to the $\omega_f < \omega_c$ case. If A_f is real, the long-time asymptotic solution is continuous across $V = c$, whereas it is not for $\omega_f < \omega_c$.

III.5. Critical velocities over ω_f

It is worth exploring how the breadth of the regions described in Sections III.4.1 and III.4.2 change with varying ω_f. Figure III.18 shows the loci of observable critical velocities in the solution to III.8. It was generated by plotting the four velocities V_1 through V_4, given in (III.14) and (III.16), for a range of ω_f values holding all other parameter fixed at the same values used in prior figures.

For a value of ω_f below the critical frequency (red horizontal line), we can see that there are four critical velocities, two upstream and two downstream. The outer pair (V_1 and V_4) are the *Leading Edges of the Forced Solution* and the inner pair (V_2 and V_3) are the *Leading*

Edges of the Additionally Forced Regions. For a value of ω_f above the critical frequency (blue horizontal line), we can see that there are only two critical velocities (V_1 and V_4) — the pair are the *Leading Edges of the Forced Solution.* Note that the two inner velocities converge on $V = 0$ as ω approaches ω_c from below.

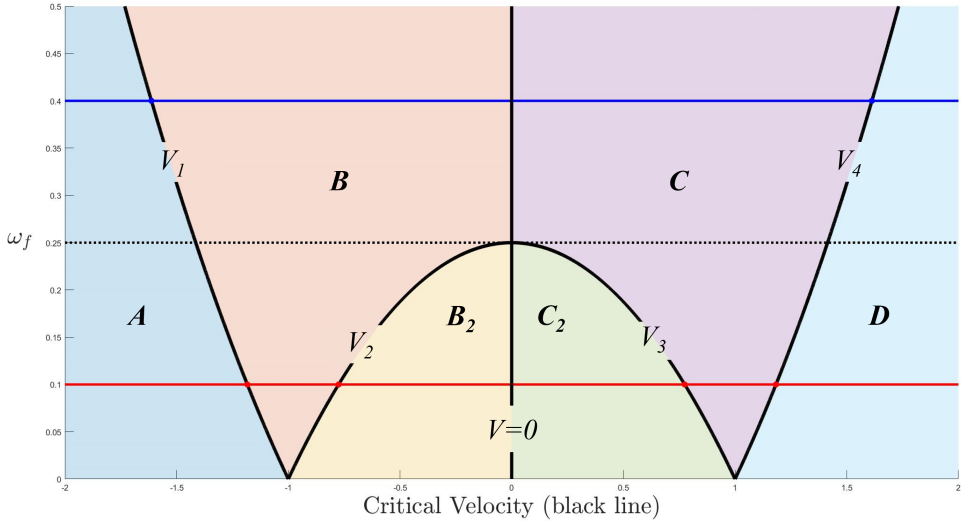

Figure III.18: Plot tracking critical velocities (black curves) (given in (III.14) and (III.16)) for different values of the forcing frequency. A horizontal line at $\omega = 0.25$ marks the critical frequency ω_c. The plot was generated using $B = 1$ and $c = 1$. Note that the critical velocity $V = c = 1$ is not included on this plot. Two horizontal lines (blue at $\omega_f = 0.4$ and red at $\omega_f = 0.1$) are included to demonstrate how to extract the critical velocities V_1, V_2, V_3, and V_4 for any given value of ω_f.

Tying Figure III.18 back to the long-time asymptotic forms, we can see that the velocity V_1 is the rate at which the contribution of k_3 travels away from the forcing location. The same is true for V_2 and k_0, V_3 and k_1, and V_4 and k_2. As ω_f is increased up towards the critical frequency, the contributions from k_2 and k_3 propagate faster through the domain, and

those of k_0 and k_1 propagate more slowly. Above the critical frequency, the contributions of k_0 and k_1 decay in time, and are therefore not relevant to the bounding amplitudes. See Figures III.3 and III.4 for the pole structure on either side of ω_c.

Through the inspection of (III.15c) and (III.15d), we see that the bounding amplitudes of Regions B_2 and C_2 go to infinity (there is a $(k_0 - k_1)$ in the denominators) and the widths go to zero ($V_2, V_3 \to 0$) as $\omega_f \to \omega_c$ from below. Due to the change in pole structure (k_0 and k_1 are coincident when $\omega_f = \omega_c$ (III.9d)) we did not perform the full asymptotic analysis for this threshold case. However, we did simulate results using the FSS (Appendix B.1.1) at the critical frequency. Although not shown here, the result appears to have a single algebraically growing peak at $V = 0$. The behavior predicted in Figure III.18 as $\omega_f \to \omega_c$ from below is consistent with that from the FSS. The infinite bounding amplitude corresponds to the peak growing without bound.

III.6. Discussion

We now comment on differences between the signaling response from operators that enable exponential growth (Figure III.1) and those that only admit algebraically growing solutions (Figures III.9 and III.17).

In an exponentially unstable system, the bounding envelope for the transient corresponds to V_- and V_+ in Figure III.1. These correspond precisely to the velocities at which the rate of exponential growth is equal to zero, and there is a continuous locus of growing amplitudes for $V \in [V_-, V_+]$. In the algebraically growing system, there is only one velocity, $V = c$, at which growth can occur (see Figures III.9 and III.17). The interaction between transient and

forced responses is significantly altered; instead of a broad region of competition between growing forced and transient responses even at large times, there are only large regions of constant amplitude that expand away from the source with time in accordance with the bounding critical velocities. Additionally, the speed V_E in Figure III.1 is not present in algebraically growing systems, as this corresponds to the velocity at which the arguments of exponential growth of the transient are equal to that of the transient. There is no relevant analogous speed in the algebraically growing system. Note, however, that there is a direct crossover between exponential and algebraic signaling for the velocity V_I in Figure III.1 with those in this chapter. All the critical velocities (V_1-V_4) in the neutrally stable response correspond to locations where the influence of poles (arising from the oscillatory forcing) in the Fourier integral changes. This corresponds to their inclusion in contours used to evaluate the integrals at large time.

While classical stability analysis (III.5) fails to classify the behavior of the transients, it correctly predicts that there is no growth or decay in the long-time response of (III.8) for any given x (V approaches 0). This is an intriguing result because the transient behavior arises from the homogeneous solution to which classical stability analysis is applied.

The signaling response of (III.8) has both upstream and downstream effects of forcing as time goes to infinity (see the long-time forced regions of Section III.4.1.5). The effects neither grow nor decay in space and thus, given enough time, the effects of the forcing will infect the whole domain with constant amplitude oscillations. This behavior is unlike that of an exponential signaling problem [36], where the forced solution either grows or decays in space at large times. That said, there is an upstream and downstream behavior present

in both algebraic and exponentially growing systems induced by the forcing.

III.7. Conclusions

The oscillatory forcing of (III.8) at neutral stability leads to a transient growing peak and a long-time oscillatory response. We find that the behavior of the transient solution is highly dependent on how the disturbance is initiated. Only certain phases of the forcing function will lead to an algebraically growing peak in the response. This dependence on initial condition is analogous to the findings of King et al. [15], where only forcing the initial surface velocity leads to algebraic growth. The bounding amplitudes and critical velocities, which characterize the oscillatory response, can be extracted from the long-time asymptotic solution; specifically, the amplitudes are extracted from the long-time asymptotic solution as the sum of multiple sinusoids and the critical velocities are extracted from the coincidence of a pole from the particular solution and a saddle point from the method of steepest descent. We find that there is a significant change in structure for forcing frequencies above and below a critical forcing frequency.

In conclusion, we note that signaling in the system studied yields a response that travels both upstream and downstream from the disturbed location. This behavior, combined with the spatial invariance within the regions, means that the disturbance will infect the entire domain after a sufficiently long time. From an manufacturing perspective, the system is vulnerable to such disturbances, as the damage to the product will not be localized.

Chapter IV

On the two-dimensional extension of one-dimensional algebraically growing waves at neutral stability

This section, with the exception of adjustments to the flow and references, was taken directly from the manuscript "On the two-dimensional extension of one-dimensional algebraically growing waves at neutral stability" which has been submitted for publication [17].

IV.1. Introduction

An essential feature of a partial differential equation operator that models wave propagation is whether it admits solutions that will amplify or damp with time as waves propagate in space. In some physical processes, such as in liquid fuel atomizers [1, 2, 3], instabilities are necessary to enable the flow to break into droplets, and in other cases turbulence is used to facilitate mixing [18]. In many processes, however, stability of wave-like disturbances is not only desired, it is required, such as in thin film coating used to manufacture printed electronics and liquid crystal display screens [4, 5]. Although the latter processes are governed by the nonlinear equations of fluid dynamics, it is standard to linearize about steady operating conditions; coating processes are run with tight constraints on the uniformity of the product, and thus linearized equations are often sufficient to predict the effect of process disturbances [6].

Classical stability theory, introduced by Lord Rayleigh [7] in 1880 and further refined over the next hundred years, serves to classify the response, h, of a linearized system by assembling its fundamental modes (responses), $h_{\mathbf{k}}$, as $h = \sum_{(k_x,k_z)} h_{\mathbf{k}}$. For a two-dimensional (2D) linear operator, each mode may be expressed as:

$$h_{\mathbf{k}} = A(\mathbf{k})e^{i(\mathbf{k}\cdot\mathbf{x}-\omega t)} = A(k_x,k_z)e^{i(k_x x+k_z z-\omega t)} \tag{IV.1}$$

where $\mathbf{k}$ is the real wave number vector, $\mathbf{x}$ is the spatial vector, ω is a complex frequency, t is time, and $A(\mathbf{k}) = A(k_x, k_z)$ is the wave number dependent amplitude. By substituting (IV.1) into the homogeneous version of the linearized operator, the dispersion relation $\omega \equiv \omega(\mathbf{k}) = \omega(k_x, k_z)$ is found such that the result (IV.1) is nontrivial (i.e., leaving $A(\mathbf{k})$ arbitrary).

The idea, then, is to examine the behavior of individual modes to draw stability conclusions. In particular, since $\mathbf{k}$ is real valued, the only mechanism for (IV.1) to admit exponential growth or decay is through the imaginary part of the complex frequency, $\omega_i(\mathbf{k}) \equiv \mathrm{Im}[\omega(\mathbf{k})]$. Any single mode that grows in time will dominate other modes which decay in time. Furthermore, of the growing modes, the one that grows the fastest (or decays the slowest) will dominate the behavior of h as $t \to \infty$ with an exponential growth (or decay) rate of $\omega_{i,\max} \equiv \max(\omega_i(\mathbf{k}))$ determined from the dispersion relation. The amplitude of the long-time behavior, $h_{\max}$, may be expressed as:

$$h_{\max} \sim A_{\max} e^{\omega_{i,\max} t} \qquad \text{as } t \to \infty, \tag{IV.2}$$

where $A_{\max}$ is the amplitude of the maximum growth mode. In (IV.2), $\omega_{i,\max}$ can be used to determine the classical stability for a given set of conditions as follows [8, 12, 9]:

$$\omega_{i,\max} < 0: \quad \text{The system is stable,} \tag{IV.3a}$$

$$\omega_{i,\max} = 0: \quad \text{The system is neutrally stable,} \tag{IV.3b}$$

$$\omega_{i,\max} > 0: \quad \text{The system is unstable.} \tag{IV.3c}$$

Depending on the operator being studied, the stability of the system may depend on the parameters in the governing equation. If a given set of parameters results in $\omega_{i,\max} = 0$, the condition of neutral stability is met. When this occurs, the system governed by the operator is said to be at the "neutral stability boundary", as small changes in the parameters can often move the system to a state of stability or instability .

Classical stability analysis implies that a stable system (IV.3a) will exhibit exponentially damped responses with time whereas a system that is unstable (IV.3c) will exhibit exponen-

tial amplification. However, at the boundary between the two regimes (IV.3b), the method fails to accurately predict the long-time linear stability of the system, as shown in the previous work by King et al. [15] and Huber et al. [16]. Specifically, King et al. examined a one-dimensional (1D) operator (henceforth referred to as 1D-KRK[1]) that governs the response to varicose perturbations in a curtain flow, and Huber et al. studied a 1D operator (henceforth referred to as 1D-CMH)[1] that enabled the neutral stability threshold in (IV.3) to be traversed by the variation of a parameter. At the neutral stability boundary, neither operator should result in growing or decaying responses as per the classification given by (IV.3b); however, both 1d-KRK and 1D-CMH admit solutions that exhibit *algebraic* (i.e., t^p, p real and rational) growth in time. In this chapter, we examine the 2D extensions of the 1D-KRK and 1D-CMH operators, denoted respectively as the 2D-KRK and 2D-CMH operators.

A closely related set of problems is that of one-dimensional water waves that are neutrally stable according to (IV.3b) but whose amplitudes damp with an algebraic $t^{-1/2}$ dependence at long times [13, 14]. Lighthill notes that the damping rate is reduced by a factor of $t^{-1/2}$ (i.e., $t^{-1/2}$ becomes t^{-1}) with the addition of each spatial dimension [14]. Herein, we show that this feature is also true of at least two systems that exhibit algebraic growth in 1D.

The chapter is organized as follows. In Section IV.2, the 2D-KRK operator is introduced, its Fourier integral solution is obtained, and its long-time asymptotic behavior is determined. Section IV.3 similarly examines the 2D-CMH operator. A comparison between the 2D

[1]Notation is chosen to reflect the dimesionality of the operator and the lead author's initials

responses in Sections IV.2 and IV.3 and their 1D counterparts in [15] and [16] is provided in Section IV.4, and concluding remarks are provided in Section IV.5.

IV.2. 2D-KRK: 2D extension of algebraically growing 1D-KRK model for varicose waves in liquid curtains

IV.2.1 Problem statement

The first problem examined here is the 2D extension of a 1D operator derived from a model of varicose waves in a thin flowing curtain in the absence gravity and with passive ambient gas [2]. The previous 1D analysis found that the response to disturbances in this flow grows algebraically; a natural extension is to examine the response to a 2D disturbance. The increase in dimension is implemented by replacing all the 1D spatial derivatives with 2D del operators as follows:

$$\left[\left(\frac{\partial}{\partial t}+\mathbf{c}\cdot\nabla\right)^2+B^2\nabla^4\right]h=A\delta(x)\delta(z)\delta(t), \tag{IV.4a}$$

$$\mathbf{c}\cdot\nabla=c_x\frac{\partial}{\partial x}+c_z\frac{\partial}{\partial z},\qquad \nabla^4=\frac{\partial^4}{\partial x^4}+2\frac{\partial^4}{\partial x^2z^2}+\frac{\partial^4}{\partial z^4}, \tag{IV.4b}$$

$$h(x,z,0)=0,\qquad \frac{\partial h}{\partial t}(x,z,0)=0, \tag{IV.4c}$$

$$h\to 0\quad\text{as}\quad x,z\to\pm\infty,\qquad c_x,c_z\geq 0,\qquad B,A\in\mathbb{R}. \tag{IV.4d}$$

In (IV.4a), $\mathbf{c}$ is the underlying convective fluid flow vector with components c_x and c_z, and B is a real valued parameter that is related to the Weber number as described in [15]. Note that the forcing function in (IV.4a) has the real-valued amplitude A. As written, the constraints in (IV.4c) are chosen to be homogeneous; care, however, has been taken

in making that choice. It is clear from the 1D-KRK and the 1D-CMH [15, 16] analyses that the form of initial conditions can affect whether algebraic growth occurs. This is discussed further in the next section, before proceeding to examine the solution to the system in (IV.4).

IV.2.2 Initial condition justification

It is first useful to note that an impulse disturbance to the surface velocity, $\partial h/\partial t$ in (IV.4c), has the exact same effect as the impulse forcing function included in (IV.4a) (see C.1.1 for details). For this reason, the initial velocity may be taken to be zero in (IV.4c) without loss of generality. Additionally, an impulse disturbance to initial surface height, h in (IV.4c), leads to a solution that violates the condition of $h \to 0$ as $x, z \to \pm\infty$ in (IV.4d); this nonphysical solution is included in C.1.1. Although not stated explicitly in [15], this violation also occurs in 1D-KRK. If one extends the class of allowable solutions to include spatially non-local responses (i.e., solutions which violate $h \to 0$ as $x, z \to \pm\infty$), the solution nevertheless does damp with time. To avoid the nonphysical nature of this solution however, the initial height is chosen to be zero in (IV.4c). In summary, homogeneous constraints on the system in (IV.4) are chosen without loss of generality in the stability conclusions that follow.

IV.2.3 Classical stability analysis

In the one-dimensional problem 1D-KRK, all modes $h_{\mathbf{k}}$ in (IV.1) are neutrally stable [15]. The addition of a higher dimension does not change this behavior. Through the substitution of the modal form (IV.1) into the homogeneous version of (IV.4a), the following dispersion

relation is obtained:

$$\omega = (c_x k_x + c_z k_z) \pm B(k_x^2 + k_z^2). \tag{IV.5}$$

In (IV.5), k_x and k_z are the real wave numbers in the x and z directions, respectively, and ω is the complex frequency. Because c_x, k_x, c_z, k_z are real, ω is always real, just as in the case of water waves [13, 14]. As such, the imaginary part of ω is always 0, and all modes (IV.1) are neutrally stable for all values of the parameters according to (IV.3). As a check, note that the 1D dispersion relation (Equation (5a) in [15] with $n = 2$) is recovered by letting $c_z = k_z = 0$ in (IV.5). According to classical stability analysis in (IV.3), the response to such a disturbance should neither grow nor decay. However, the solution grows algebraically in 1D as shown in King et al. [15].

IV.2.4 Integral solution

The solution to (IV.4) is found by taking Fourier transforms in x and z (resulting in the transformed variable $\hat{\hat{h}}_{xz}$) and the Laplace transform in t. The resulting Fourier inversion integral solution is given as

$$h(x,z,t) = \frac{1}{4\pi^2} \int_{-\infty}^{\infty} \int_{-\infty}^{\infty} \hat{\hat{h}}_{xz} e^{ik_x x} e^{ik_z z} dk_x dk_z,$$

$$\hat{\hat{h}}_{xz} = A e^{-i\psi t} \frac{\sin(\eta t)}{\eta}, \qquad \psi = c_x k_x + c_z k_z, \qquad \eta = B(k_x^2 + k_z^2). \tag{IV.6}$$

Note that there is a removable singularity at $\eta = 0$ in (IV.6). In order to extract the asymptotic behavior of the integral at large times, the standard approach is to express the sine function in terms of complex exponentials and evaluate each new integral as t goes to infinity. However, doing so leads to poles along the path of integration, i.e. principal values.

Although one could proceed in this way, the issue is avoided entirely by introducing the new variable ξ into the integral (IV.6) to obtain

$$\tilde{h}(x,z,t,\xi) = \frac{A}{4\pi^2}\int_{-\infty}^{\infty}\int_{-\infty}^{\infty} e^{-i\psi t}\left(\frac{\sin(\xi\eta t)}{\eta}\right)e^{ik_x x}e^{ik_z z}dk_z dk_x, \tag{IV.7a}$$

$$\tilde{h}(x,z,t,0) = 0, \qquad \tilde{h}(x,z,t,1) = h(x,z,t), \tag{IV.7b}$$

where (IV.6) and (IV.7a) are linked via the relation in (IV.7b). The structure of the integrand in (IV.7a) is chosen such that taking its derivative with respect to ξ completely removes the η in the denominator as:

$$\frac{\partial\tilde{h}}{\partial\xi} = \frac{At}{4\pi^2}\int_{-\infty}^{\infty}\int_{-\infty}^{\infty} e^{-i\psi t}\cos(\xi\eta t)e^{ik_x x}e^{ik_z z}dk_z dk_x. \tag{IV.8}$$

The solution for h may then be obtained via the integration of the resulting (IV.8) using the constraints in (IV.7b):

$$h(x,z,t) = \int_0^1 \frac{\partial\tilde{h}}{\partial\xi}d\xi. \tag{IV.9}$$

In order to evaluate the integral through the method of steepest descent, the cosine in (IV.8) is complexified and the resulting integral is decomposed as

$$\frac{\partial\tilde{h}}{\partial\xi} = \frac{At}{8\pi^2}\left(\mathcal{Q}+\mathcal{W}\right), \tag{IV.10a}$$

$$\mathcal{Q} = \int_{-\infty}^{\infty} e^{\left(i\xi Bk_z^2 + i(\frac{z}{t}-c_z)k_z\right)t}dk_z\left[\int_{-\infty}^{\infty} e^{\left(i\xi Bk_x^2 + i(\frac{x}{t}-c_x)k_x\right)t}dk_x\right], \tag{IV.10b}$$

$$\mathcal{W} = \int_{-\infty}^{\infty} e^{\left(-i\xi Bk_z^2 + i(\frac{z}{t}-c_z)k_z\right)t}dk_z\left[\int_{-\infty}^{\infty} e^{\left(-i\xi Bk_x^2 + i(\frac{x}{t}-c_x)k_x\right)t}dk_x\right]. \tag{IV.10c}$$

The integrals in (IV.10b) and (IV.10c) are evaluated in closed form (see C.1.2) to yield:

$$\frac{\partial\tilde{h}}{\partial\xi} = \frac{A}{4\xi B\pi}\sin\left(\frac{t}{4\xi B}\left((V_x-c_x)^2+(V_z-c_z)^2\right)\right) \tag{IV.11}$$

where $V_x = {}^{x}/_{t}$ and $V_z = {}^{z}/_{t}$ are velocities introduced to provide a convenient representation of the solution.

Equation (IV.11) is then substituted into (IV.9) and integrated to attain the solution to (IV.4). The exact solution can be expressed in terms of a similarity variable Φ as

$$h(\hat{V},t) = \frac{A}{4B\pi}\left(\frac{\pi}{2} - \int_0^{\frac{\Phi}{4B}} \frac{1}{u}\sin(u)du\right), \qquad \Phi = \hat{V}^2 t, \tag{IV.12a}$$

$$\hat{V} = \sqrt{(V_x - c_x)^2 + (V_z - c_z)^2}. \tag{IV.12b}$$

In (IV.12b), $\hat{V} = 0$ corresponds to the peak of the response, $V_x = c_x$ and $V_z = c_z$. More generally, $\hat{V}$ is defined as the locus of velocities relative to the velocity of the convecting peak (c_x, c_z). Note that when $\hat{V} = 0$ in (IV.12a) the solution has a constant height expressed as

$$h\Big|_{\hat{V}=0} = \frac{A}{8B}. \tag{IV.13}$$

The long-time asymptotic behavior of the sine integral in (IV.12a) for $\hat{V} \neq 0$ may be expressed as:

$$h(\Phi)\Big|_{(\hat{V}\neq 0)} \sim \frac{A}{\pi\Phi}\cos\left(\frac{\Phi}{4B}\right) + O\left(\frac{1}{\Phi^2}\right), \quad \Phi = \hat{V}^2 t, \quad \text{as } \Phi \to \infty. \tag{IV.14}$$

The limit of Φ going to infinity aligns with the limit of t going to infinity for any fixed non-zero $\hat{V}$.

The sine integral solution (IV.12a) (implemented using MATLAB's sinint function) is shown in Figures IV.1 and IV.2 for different values of the convection parameters c_x and c_z. In accordance with (IV.13), the height of the response peak (i.e., $\hat{V} = 0$) remains constant as

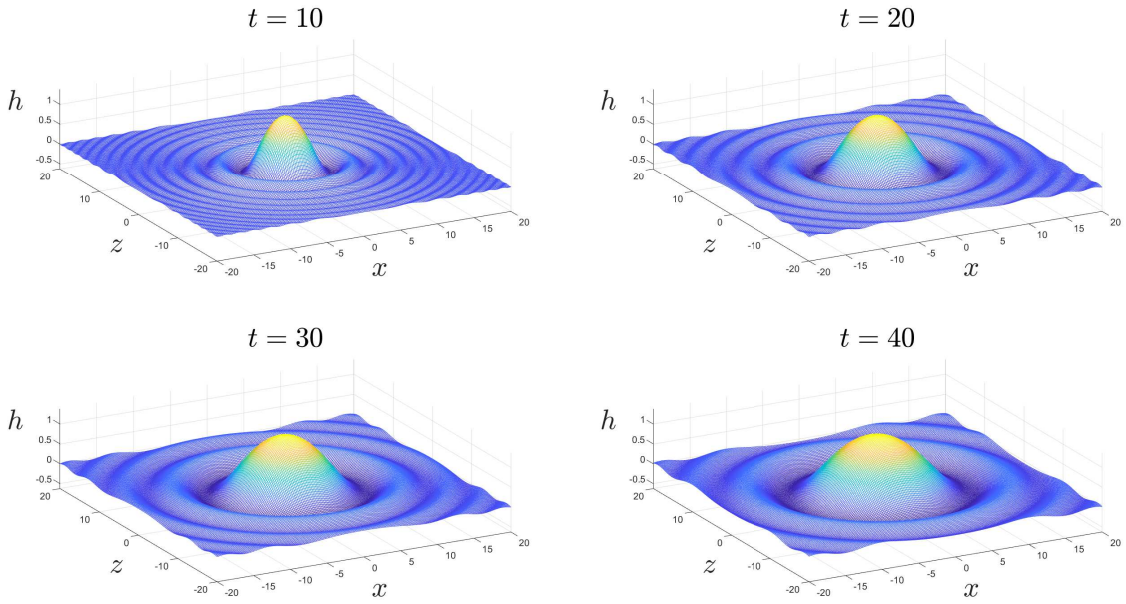

Figure IV.1: Time evolution of 2D-KRK response given by (IV.12a) with $A = 10$ and $B = 1$. There is no underlying convective flow as $c_x = c_z = 0$. The constant height peak remains situated at $x = z = 0$ and the breadth of the response increases as time progresses. The radius of any given phase feature (e.g. crest or trough) increases as $\sqrt{t}$ as given by (IV.17).

the response evolves in time. For the other loci of velocities, $\hat{V} \neq 0$, the solution decays as $O(1/t)$ in accordance with (IV.14).

The similarity variable in (IV.12a) implies that a similarity transform could be applied to (IV.4) to attain an ordinary differential equation whose exact solution is (IV.12a). Figure IV.3 provides a plot of the similarity solution, which has been represented spatially in Figures IV.1 and IV.2. By inspection, it is observed that the spatial responses of Figures IV.1 and IV.2 are rotations and stretches of this solution relative to the location of

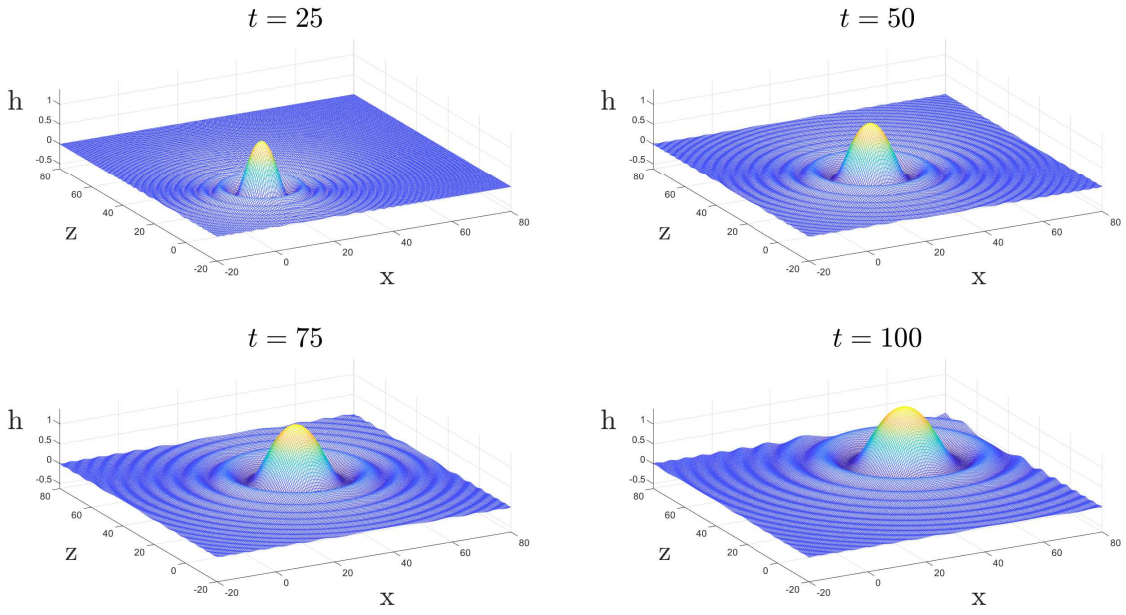

Figure IV.2: Time evolution of 2D-KRK response given by (IV.12a) with $A = 10$, $B = 1$, and underlying convective flow of $c_x = c_z = 0.5$. The peak moves along $(x, z) = (c_x t, c_z t)$com, and the breadth of any given phase feature (e.g. crest or trough) propagates radially relative to this position with time as $\sqrt{t}$ as given by (IV.16).

the traveling peak ($\hat{V} = 0$) at $x = c_x t$ and $z = c_z t$ according to (IV.12b).

The similarity solution (IV.12a) may be used to extract more features of the solution in the physical (x, z, t) domain. If $\hat{V}$ is held fixed in (IV.12), then Φ goes as t, and we can examine the behavior of any propagation speed relative to that of the peak (corresponding to $\hat{V} = 0$). In accordance with (IV.14), then, the response for any fixed $\hat{V}$ decays asymptotically as $1/t$ for large times. The variable Φ may be equivalently expressed explicitly in terms of space and time as:

$$\Phi = \frac{R^2}{t}, \quad R^2 = (x - c_x t)^2 + (z - c_z t)^2, \tag{IV.15}$$

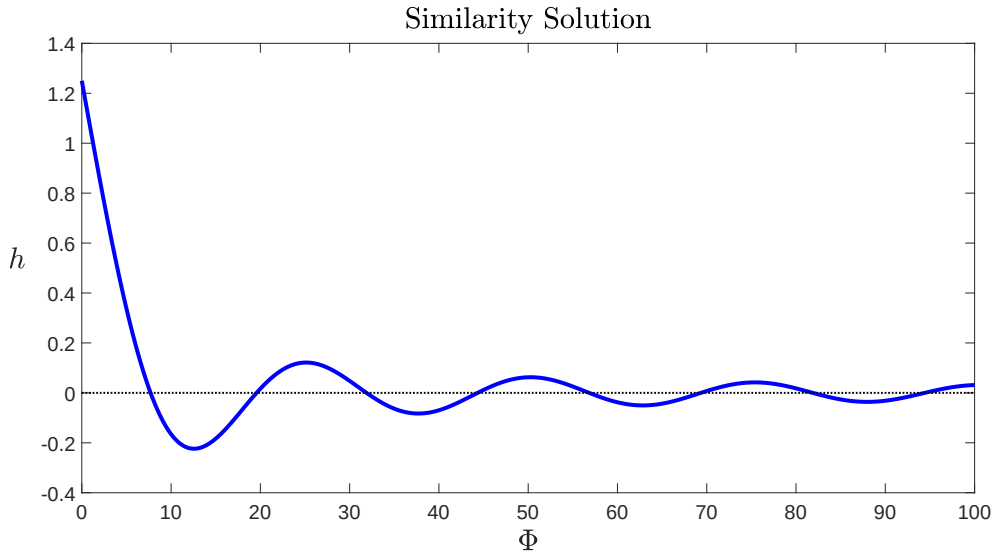

Figure IV.3: Similarity solution (IV.12a) for $A = 10$ and $B = 1$.

where R is the radius of a circle centered at $x = c_x t$ and $z = c_z t$. Thus for fixed R, Φ will go as $1/t$ as shown in (IV.15). A fixed value of R provides the locus of points a distance of R away from the convecting peak. This is most easily visualized when $c_x = c_z = 0$ (Figure IV.1), as fixed values of R corresponds to fixed concentric circles in the x, z plane. As time goes on, the solution at a fixed R will yield smaller Φ values; Figure IV.3 indicates that the solution grows towards the maximum value of the peak as $t \to \infty$ (i.e., $\Phi \to 0$ for fixed R).

IV.2.5 Spatial stability

The similarity solution (IV.12a) can be used to track the spatial behavior of the response. For any given fixed value of Φ, $h(\Phi)$ will be constant. Therefore, all values of x, z, and t which result in the same Φ will be the same height. This also means that the apparent phase of the wave form is fixed for a given value of ϕ. Equation (IV.15) may be rewritten

as:

$$R = \sqrt{(x - c_x t)^2 + (z - c_z t)^2} = \sqrt{\Phi t}. \tag{IV.16}$$

Thus, for any given height, the solution (fixed Φ) moves radially relative to the peak as $\sqrt{t}$, but does so more slowly than the peak itself translates ($x = c_x t, z = c_z t$). Figure IV.4 provides a visualization of these features for a given value of Φ.

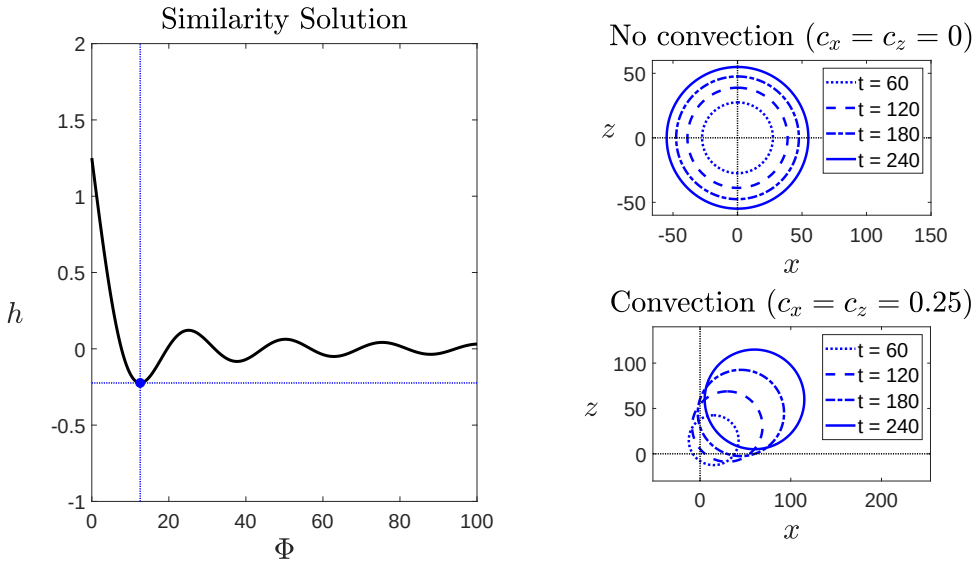

Figure IV.4: Similarity solution (IV.12) (left) with the specific point of $\Phi = 4B\pi$ chosen (•). This point is tracked through time for non convective (top right) and convective (bottom right) parameters. The disturbance is initiated at $(x, z) = (0, 0)$ in accordance with (IV.4a). In both cases, the circles of constant h, given by (IV.16) and (IV.17), propagate out from the peak over time. For the convective case, the rings spread outwards more slowly than they convect. All data was generated with $A = 10$ and $B = 1$.

For the case where either c_x or c_z is nonzero, the peak itself convects away from its initializing location at $x = z = 0$. From that perspective, the solution itself has a character akin to a

convectively unstable system [12, 9], although here the maximum height of the system is constant. For this reason, we follow the convention of Barlow et al. [23] in classifying these waves as "convectively neutral." It is worth noting that if both convective parameters are zero, then the expanding circles are all concentric, as shown in Figure IV.4, and are given by

$$\sqrt{x^2 + z^2} = \sqrt{\Phi t}. \tag{IV.17}$$

In this case the system can said to be "absolutely neutral" because the disturbance will eventually infect any given (x, z) domain [23]. Unlike absolutely unstable systems, the solution here does not grow without bound, as the maximum value is the constant height of the peak.

IV.3. 2D-CMH: 2D extension of algebraically growing 1D-CMH model

IV.3.1 Problem statement

We now consider the 2D extension of the 1D differential operator described in Section [16] and examine the response of that system. For reference in what follows, recall from Section IV.1 that the 1D and 2D problems are referred to as 1D-CMH and 2D-CMH, respectively. The well-posed system to examine the 2D response, h, is given by

$$\left[\frac{\partial^2}{\partial t^2} + \nabla^4 - \nabla^2\frac{\partial}{\partial t} + B\frac{\partial}{\partial t} + B^2\right] h = A\delta(x)\delta(z)\delta(t), \tag{IV.18a}$$

$$\nabla^4 = \frac{\partial^4}{\partial x^4} + 2\frac{\partial^4}{\partial x^2 z^2} + \frac{\partial^4}{\partial z^4}, \qquad \nabla^2 = \frac{\partial^2}{\partial x^2} + \frac{\partial^2}{\partial z^2}, \tag{IV.18b}$$

$$h(x,z,0)=0, \qquad \frac{\partial h}{\partial t}(x,z,0)=0, \tag{IV.18c}$$

$$h\to 0 \quad \text{as} \quad x,z\to\pm\infty, \qquad B\in\mathbb{R}. \tag{IV.18d}$$

where B is a real parameter affecting system stability (see [16]) and A is a real forcing magnitude. Note that (IV.18) is a simplified extension of the 1D-CMH operator found in [16], as the terms responsible for convection have been removed to facilitate the analysis. As with the previous problem, zero valued initial conditions are chosen. Further justification for this choice is provided in Section IV.3.3.

IV.3.2 Classical stability analysis

The classical stability analysis is performed by substituting (IV.1) into the homogeneous form of (IV.18) as described previously. A dispersion relation for $\omega(\mathbf{k})$ is obtained that assures nontrivial solutions,

$$\omega=\frac{1}{2}\left(-i(B+\eta)\pm\sqrt{3\left(\eta-\frac{B}{3}\right)^2+\frac{8}{3}B^2}\right), \qquad \eta=k_x^2+k_z^2. \tag{IV.19}$$

Equation (IV.19) indicates that

$$\omega_i=-\frac{(B+k_x^2+k_z^2)}{2} \quad \text{and that} \quad \omega_{i,\max}=-\frac{B}{2}, \tag{IV.20}$$

and thus stability is determined by the sign of B in (IV.20). According to the classical stability characterization (IV.3), the system is unstable when $B<0$, stable when $B>0$, and neutrally stable when $B=0$. This is the same characterization given to the 1D-CMH system in [16]. For $B=0$ (the situation examined in this chapter) the dispersion relation is written for reference as

$$\omega=\frac{1}{2}\left(-i\eta\pm\eta\sqrt{3}\right), \quad \eta=k_x^2+k_z^2, \quad \eta\geq 0. \tag{IV.21}$$

The corresponding operator is expressed as

$$\left[\frac{\partial^2}{\partial t^2} + \nabla^4 - \nabla^2 \frac{\partial}{\partial t}\right] h = A\delta(x)\delta(z)\delta(t), \tag{IV.22a}$$

$$\nabla^4 = \frac{\partial^4}{\partial x^4} + 2\frac{\partial^4}{\partial x^2 z^2} + \frac{\partial^4}{\partial z^4}, \qquad \nabla^2 = \frac{\partial^2}{\partial x^2} + \frac{\partial^2}{\partial z^2}, \tag{IV.22b}$$

$$h(x, z, 0) = 0, \qquad \frac{\partial h}{\partial t}(x, z, 0) = 0, \tag{IV.22c}$$

$$h \to 0 \quad \text{as} \quad x, z \to \pm\infty. \tag{IV.22d}$$

IV.3.3 Initial Conditions

As discussed in the context of the 2D-KRK problem in Section IV.2, care has been taken in choosing homogeneous constraints in (IV.18c) and (IV.22c) so as to assure correct stability conclusions are drawn about the operator. In particular, the effect of applying an impulse function to the initial surface velocity $\partial h/\partial t$, is the same as applying the impulse forcing function included in (IV.22a) in an analogous way to the 2D-KRK problem of Section IV.2 (see Supplemental Material Section C.4.1). Due to the complexity of the analysis method, the effect of a delta function in the initial surface height, $h(x, z, 0)$ in (IV.22c), was surveyed numerically via the Fourier Series Solution (FSS) provided in C.2.1. It should be noted that spatially infinite domain problems require transforms to obtain solutions, but here a discrete Fourier series is utilized. To do so, the domain of the operator is truncated to be sufficiently large such that changes in the domain length do not yield any changes in the response in the times examined [21]. We find that the response from an initial surface height decays along all $V_x = x/t$ and $V_z = z/t$ velocities either at the same rate as, or faster than, the solution disturbed with only the surface velocity. We conclude that an impulsive function forcing is a sufficient disturbance to extract the stability character of

the operator. As a result, the analysis is conducted with just the impulse forcing function in (IV.22a) and the initial conditions given in (IV.22c). In what follows, the just-described FSS (Appendix C.2.1) is used to validate all asymptotic results in their regimes of validity and to generate full solutions to (IV.22). In the 3D plot to follow (Figure IV.5), the FSS is generated using 2000 terms each in k_x and k_z. For the plots where only one direction is shown (Figures IV.10 and IV.6), 4000 terms were used in k_x; k_z is not needed to generate solutions because only $z = 0$ was considered.

IV.3.4 Analysis

The solution to (IV.22) is found by taking Fourier transforms in x and z (resulting in the transformed variable $\hat{\hat{h}}_{xz}$) and the Laplace transform in t. The resulting Fourier inversion integral solution is given as

$$h(x,z,t) = \frac{1}{4\pi^2}\int_{-\infty}^{\infty}\int_{-\infty}^{\infty}\hat{\hat{h}}_{xz}e^{ik_x x}e^{ik_z z}dk_x dk_z,$$

$$\hat{\hat{h}}_{xz} = \left(Ae^{-\frac{\eta}{2}t}\right)\frac{\sin\left(\frac{\eta}{2}\sqrt{3}t\right)}{\frac{\eta}{2}\sqrt{3}}, \qquad \eta = k_x^2 + k_z^2. \tag{IV.23}$$

Note that the result (IV.23) is similar in form to that of (IV.6) for the 2D-KRK problem (Section IV.2), with the significant difference being the $O(k_x^2, k_z^2)$ term in the damped exponential instead of the $O(k_x, k_z)$ term. This difference in form leads to a significant increase in analysis complexity. In order to evaluate (IV.23), it is first converted to polar form as, $(k_x, k_z) \to (\xi, \theta)$, with radial component $\xi \in [0, \infty)$ and angular component $\theta \in [0, 2\pi]$. The result is the new integral given by

$$h(V_x, V_z, t) = \frac{A}{2\pi^2\sqrt{3}}\int_0^{\infty}\frac{\sin\left(\frac{\sqrt{3}}{2}\xi^2 t\right)}{\xi}e^{-\frac{\xi^2}{2}t}\left(\int_0^{2\pi}e^{i\mathcal{B}\xi t}d\theta\right)d\xi,$$

$$\mathcal{B} = \left(\cos(\theta)V_x + \sin(\theta)V_z\right), \qquad V_x = \frac{x}{t}, \quad V_z = \frac{z}{t}. \tag{IV.24}$$

The inner integral in θ can be evaluated asymptotically through the method of steepest descent (see Appendix C.2.2 for additional details) in the limit as $t \to \infty$ holding V_x and V_z fixed. The result is

$$\int_0^{2\pi} e^{i\mathcal{B}\xi t} d\theta \bigg|_{\hat{V}\neq 0} \sim 2\cos\left(\xi \hat{V} t - \frac{\pi}{4}\right)\sqrt{\frac{2\pi}{\hat{V}\xi t}} \quad \text{as } t \to \infty, \tag{IV.25}$$

where $\hat{V} = \sqrt{V_x^2 + V_z^2}$ is an aggregate velocity relative to the origin. When $\hat{V} = 0$, the θ integral can be evaluated exactly. The solution to the θ integral for this case is

$$\int_0^{2\pi} e^{i\mathcal{B}\xi t} d\theta \bigg|_{\hat{V}=0} = \int_0^{2\pi} e^0 d\theta = 2\pi. \tag{IV.26}$$

Equations (IV.25) and (IV.26) are substituted into (IV.24) to yield

$$h(\hat{V}, t)\Big|_{\hat{V}\neq 0} \sim \frac{A}{2\pi^2\sqrt{3}} \int_0^\infty \frac{\sin\left(\frac{\sqrt{3}}{2}\xi^2 t\right)}{\xi} e^{-\frac{\xi^2}{2}t} \left(2\cos\left(\xi\hat{V}t - \frac{\pi}{4}\right)\sqrt{\frac{2\pi}{\hat{V}\xi t}}\right) d\xi \qquad \text{as } t \to \infty, \tag{IV.27}$$

$$h(0, t) = \frac{A}{\pi\sqrt{3}} \int_0^\infty \frac{\sin\left(\frac{\sqrt{3}}{2}\xi^2 t\right)}{\xi} e^{-\frac{\xi^2}{2}t} d\xi. \tag{IV.28}$$

Equation (IV.28), which is exact, may be evaluated, through the variable substitution of $U = \frac{\sqrt{3}}{2}\xi^2 t$, to obtain a constant height solution as

$$h\Big|_{\hat{V}=0} = \frac{A}{6\sqrt{3}} \text{ for all } t. \tag{IV.29}$$

In the case where $\hat{V} \neq 0$, (IV.27) is rearranged through the substitution of $U = \xi^2 t$ to obtain

$$h \sim \frac{A}{2\pi^2\sqrt{3}} \left(\frac{(2\pi)^{\frac{1}{2}}}{\hat{V}^{\frac{1}{2}} t^{\frac{1}{4}}}\right) \int_0^\infty \frac{\sin\left(\frac{\sqrt{3}}{2}U\right)}{U^{\frac{5}{4}}} e^{-\frac{U}{2}} \cos\left(\hat{V}(Ut)^{\frac{1}{2}} - \frac{\pi}{4}\right) dU \qquad \text{as } t \to \infty. \tag{IV.30}$$

To evaluate the integral in (IV.30), the cosine is interpreted as the real part of a complex integral as follows:

$$h \sim \frac{A}{2\pi^2\sqrt{3}}\left(\frac{(2\pi)^{\frac{1}{2}}}{\hat{V}^{\frac{1}{2}}t^{\frac{1}{4}}}\right) Real\left[e^{\left(-i\frac{\pi}{4}\right)}J\right] \qquad \text{as } t \to \infty, \tag{IV.31}$$

$$J = \int_0^\infty \frac{\sin\left(\frac{\sqrt{3}}{2}U\right)}{U^{\frac{5}{4}}} e^{-\frac{U}{2}} e^{\left(i\hat{V}(Ut)^{\frac{1}{2}}\right)} dU. \tag{IV.32}$$

After performing the substitutions of $W = \sqrt{U}$ and $\tau = \sqrt{\hat{V}^2 t}$, (IV.32) can be written as

$$J = 2(J_1 + iJ_2), \tag{IV.33a}$$

$$J_1 = \int_0^\infty \frac{\sin\left(\frac{\sqrt{3}}{2}W^2\right)}{W^{\frac{3}{2}}} e^{-\frac{W^2}{2}} \cos(W\tau) dW, \tag{IV.33b}$$

$$J_2 = \int_0^\infty \frac{\sin\left(\frac{\sqrt{3}}{2}W^2\right)}{W^{\frac{3}{2}}} e^{-\frac{W^2}{2}} \sin(W\tau) dW. \tag{IV.33c}$$

In the analysis of the integrals in (IV.33b) and (IV.33c), traditional methods of asymptotic analysis fail as τ approaches infinity (which is consistent with the $t \to \infty$ limit taken in (IV.30)). In particular, integration by parts and the method of steepest descent both cannot be used extract an asymptotic behavior. Integration by parts fails because of the saddle point along the real k axis, and the method of steepest descent fails because the complex integration contour cannot be properly closed. A solution can, however, be found by complexifying the sines and evaluating the resulting integrals in terms of modified Bessel functions of the first kind, $\mathcal{I}_\nu(z)$. These can, in turn, be expanded asymptotically for large τ. This is a simplified explanation for brevity; the full analysis can be found in Supplemental Material Section C.4.3.3.

The structure of the modified Bessel functions plays a key role in the evaluation of (IV.33b) and (IV.33c) and is discussed here. The following asymptotic expansions were used in our analysis and are adjustments of those found in Abramowitz and Stegun [38] and Wolfram Alpha [39]:

$$I_\nu(z) \sim \frac{e^z}{\sqrt{2\pi z}}\mathbb{I}(\nu,z) + i\frac{e^{-z+i\pi\nu(1-2m)-i\pi m}}{\sqrt{2\pi z}}\mathbb{J}(\nu,z) \qquad \text{as } |z|\to\infty, \tag{IV.34a}$$

$$m = \begin{cases} 0, & \mathrm{Im}[z] > 0 \\ \\ 1, & \mathrm{Im}[z] < 0 \end{cases}, \qquad \nu\in\mathbb{R}, \qquad z\in\mathbb{C}, \qquad z\notin\mathbb{R}, \tag{IV.34b}$$

$$\mathbb{I}(\nu,z) = 1 - \frac{(4\nu^2-1)}{8z} + \frac{(4\nu^2-1)(4\nu^2-9)}{2!(8z)^2} - \frac{(4\nu^2-1)(4\nu^2-9)(4\nu^2-25)}{3!(8z)^3} + \frac{(4\nu^2-1)(4\nu^2-9)(4\nu^2-25)(4\nu^2-49)}{4!(8z)^4} + O\left(\frac{1}{z^5}\right), \tag{IV.34c}$$

$$\mathbb{J}(\nu,z) = 1 + \frac{(4\nu^2-1)}{8z} + \frac{(4\nu^2-1)(4\nu^2-9)}{2!(8z)^2} + \frac{(4\nu^2-1)(4\nu^2-9)(4\nu^2-25)}{3!(8z)^3} + \frac{(4\nu^2-1)(4\nu^2-9)(4\nu^2-25)(4\nu^2-49)}{4!(8z)^4} + O\left(\frac{1}{z^5}\right), \tag{IV.34d}$$

these adjustments were necessary so that they agreed with the implementation of MATLAB's besseli() function over the full range of arguments required in our analysis. Note that the only difference between $\mathbb{I}$ and $\mathbb{J}$ in (IV.34) is the sign of every other term. An interesting issue encountered in the asymptotic analysis of (IV.32) is the interactions between the leading order terms in (IV.34a). If only the asymptotically dominant terms of (IV.34a) are considered, the following solution is constructed using the first five terms in $\mathbb{I}$ and $\mathbb{J}$,

$$J = b\sqrt{2\pi}\left(C_1\tau^{-\frac{3}{2}} + C_2\tau^{-\frac{7}{2}} + C_3\tau^{-\frac{15}{2}}\right) \qquad \text{as } S\to\infty, \tag{IV.35}$$

where C_1, C_2,and C_3 are constants provided in Supplemental Material Section C.4.3.4. However, in accordance with (IV.31), the solution for J is multiplied by $e^{-i\pi/4}$ and the real part is taken. When that is done, we find that

$$Real\left[e^{-i\frac{\pi}{4}}C_1\right] = Real\left[e^{-i\frac{\pi}{4}}C_2\right] = Real\left[e^{-i\frac{\pi}{4}}C_3\right] = Real\left[e^{-i\frac{\pi}{4}}J\right] = 0. \tag{IV.36}$$

Thus, no asymptotic behavior may be extracted from the leading order terms. Consequently, the sub-dominant terms of the Bessel expansion in (IV.34) must be included in the analysis of J, which leads to the the following result

$$\begin{aligned} J \sim 2\sqrt{2\pi}e^{i\frac{\pi}{4}}\Bigg(&\frac{1}{2}\sin\left(\frac{\sqrt{3}}{8}\tau^2\right) + \frac{\sqrt{3}}{2}\cos\left(\frac{\sqrt{3}}{8}\tau^2\right) - \frac{i}{2}\cos\left(\frac{\sqrt{3}}{8}\tau^2\right) \\ &+ \frac{i\sqrt{3}}{2}\sin\left(\frac{\sqrt{3}}{8}\tau^2\right)\Bigg)S^{-\frac{3}{2}}e^{-\frac{S^2}{8}} + O\left(\tau^{-\frac{5}{2}}e^{-\frac{S^2}{8}}\right) \quad \text{as } S\to\infty. \end{aligned} \tag{IV.37}$$

Substituting (IV.37) into (IV.31) yields the asymptotic solution to (IV.22). This solution, and (IV.29), can be expressed as a function of a similarity variable Φ as

$$\begin{aligned} h(\Phi)\Big|_{\Phi\neq 0} \sim \frac{A}{\pi\sqrt{3}}\Bigg(&\sin\left(\frac{\sqrt{3}}{8}\Phi\right) \\ &+ \sqrt{3}\cos\left(\frac{\sqrt{3}}{8}\Phi\right)\Bigg)\frac{e^{-\frac{\Phi}{8}}}{\Phi} + O\left(\Phi^{-\frac{3}{2}}e^{-\frac{\Phi}{8}}\right) \quad \text{as } \Phi\to\infty, \end{aligned} \tag{IV.38a}$$

$$h\Big|_{\Phi=0} = \frac{A}{6\sqrt{3}} \text{ for all } t, \tag{IV.38b}$$

$$\Phi = \hat{V}^2 t, \qquad \hat{V} = \sqrt{V_x^2 + V_z^2}. \tag{IV.38c}$$

Note that the similarity variable Φ is defined identically to that of the 2D-KRK problem (IV.12a) for $c_x = c_z = 0$. However, unlike the solution to the 2D-KRK problem, the solution (IV.38a) is not exact. That said, the result in (IV.38b) is not subject to asymptotic constraints and is exact.

Similarly to the non-convective case for the 2D-KRK operator, the 2D-CMH solution has a single peak of constant height for all time, given exactly by (IV.29) (or equivalently by (IV.38b)). For all other velocities $\hat{V}$ in (IV.38a), the solution decays exponentially. The asymptotic solution given by (IV.38a) is nonuniform in space and cannot resolve the behavior for small Φ (see Figure IV.6). For this reason, Figure IV.5 uses the FSS (Appendix C.2.1) to construct the full response solution.

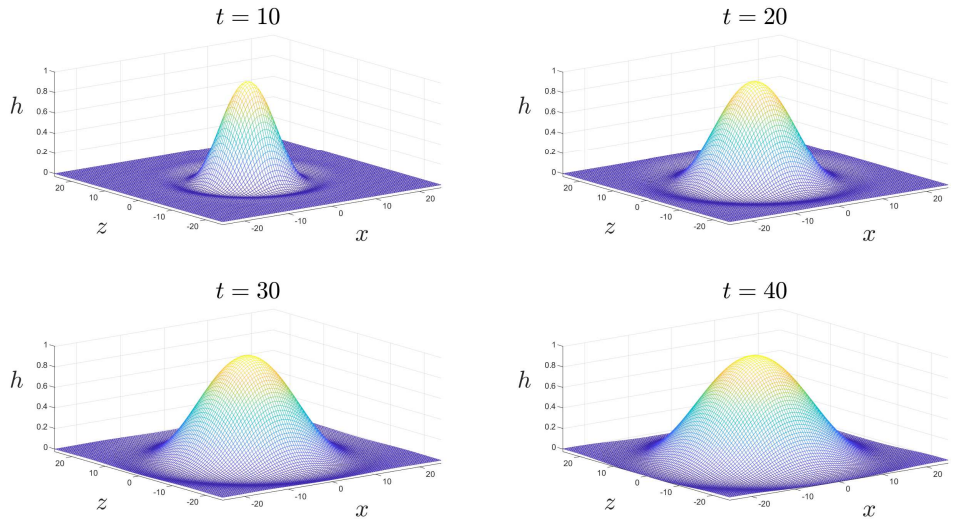

Figure IV.5: FSS to (IV.22) for several different times. As time progresses, the peak expands radially and isotropically, but the maximum value remains constant. The data was generated using 2000 Fourier terms each in k_x and k_z and a value of $A = 10$.

Notably in Figure IV.5, the response spreads radially in time; however the solution decays in time for every nonzero velocity (i.e., for a given $\hat{V}$). According to (IV.38a), the asymptotic solution is constant for any given fixed value of Φ; thus a given solution height, h, expands as $\sqrt{t}$ as given by (IV.17). Because convective terms in the operator are zero as discussed above, the response is symmetric about the origin (the location of the initiating disturbance).

As the peak at $x = z = 0$ does not grow or decay, the result may be considered "absolutely neutral" as described for 2D-KRK in Section IV.2.5.

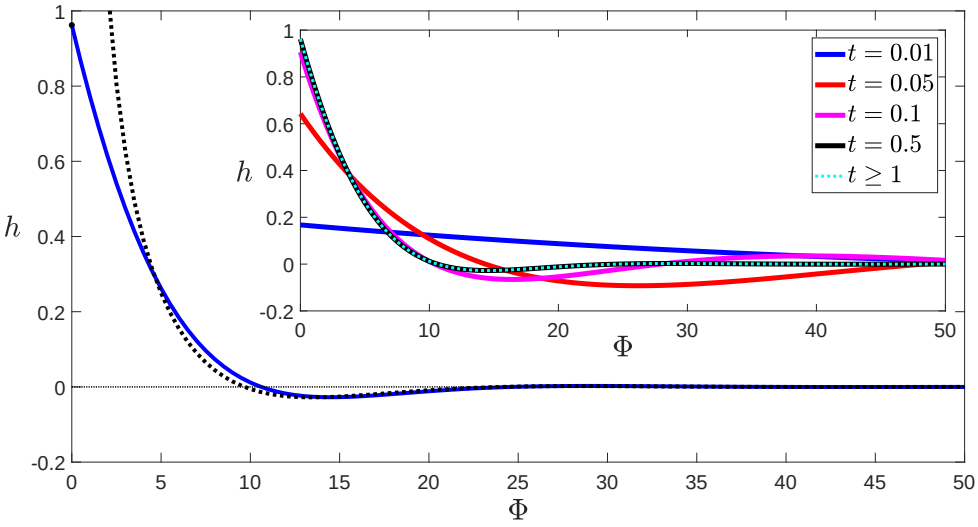

Figure IV.6: Comparison between the FSS to (IV.22)(solid blue line in main figure) and asymptotic solution (IV.38) (dashed black line in main figure) solutions for different values of Φ. The two solutions agree at large values of Φ and at $\Phi = 0$, but disagree at small values of Φ. The Φ-axis is marked with a dotted black line. The data in the main plot was generated for various x and z values $t = 10$. The inset figure shows how the FSS (Appendix C.2.1) reaches a similarity solution as t increases, well before the value of $t = 10$ used in the main plot.

As mentioned previously, the asymptotic solution (IV.38a) cannot accurately predict the solution response for small values of Φ, where all of the nontrivial behavior occurs. Nevertheless, the behavior of the asymptotic solution is useful to examine key differences between the 1D and 2D response propagation to follow. Below a value of approximately $\Phi = 11.4$, the asymptotic solution and the FSS begin to disagree, based on a criterion that

the absolute difference be less than 1% of the peak height (see C.2.3). It is worth noting that, for sufficiently long time, the FSS (Appendix C.2.1) tends towards a function solely of the similarity variable $\Phi = \hat{V}^2 t$, as shown in the insert of Figure IV.6. This allows for a compact comparison shown in the main window of Figure IV.6 between the Fourier series and the the long-time asymptotic expansion, the latter of which is solely a function of Φ for all time, but only accurate for long-time and fixed $\hat{V}$; this is shown by the agreement of the two solutions in Figure IV.6 as $\Phi \to \infty$.

IV.4. Discussion

IV.4.1 Comparison between 1D-KRK and 2D-KRK

We now compare and contrast the 2D-KRK response propagation determined above in Section IV.2 with the 1D-KRK response from previous work. To enable a direct comparison, we write the 1D solution from [15] with only a forcing disturbance as

$$h(x,z) = t\frac{|V_x - c_x|}{2B}\left[S\left(\frac{|V_x - c_x|}{2B^{\frac{1}{2}}}t^{\frac{1}{2}}\right) - C\left(\frac{|V_x - c_x|}{2B^{\frac{1}{2}}}t^{\frac{1}{2}}\right)\right][A] + \frac{1}{\sqrt{\pi}}\cos\left[\frac{\pi}{4} - \frac{(V_x - c_x)^2 t}{4B}\right]\left(\frac{A}{\sqrt{B}}t^{\frac{1}{2}}\right), \quad \text{(IV.39a)}$$

where the Fresnel integrals $S(z)$ and $C(z)$ are defined as

$$S(z) = \sqrt{\frac{2}{\pi}}\int_0^z \sin(k^2)dk, \qquad C(z) = \sqrt{\frac{2}{\pi}}\int_0^z \cos(k^2)dk. \quad \text{(IV.39b)}$$

Note that, along the peak ($V_x = c_x$), (IV.39a) becomes

$$h(x,z)\Big|_{V_x = c_x} = \frac{A}{\sqrt{2B\pi}}t^{\frac{1}{2}}. \quad \text{(IV.40)}$$

The asymptotic behavior of (IV.39a) for $V_x \neq c_x$ is provided in [15] (under the simplifications used above) as

$$h(x,t)\Big|_{V_x \neq c_x} \sim \left(\frac{AB^{\frac{1}{2}} 2^{\frac{3}{2}}}{\sqrt{2\pi}|V_x - c_x|^{\frac{5}{2}}} t^{-\frac{1}{2}} \right) \cos\left[\left(\frac{|V_x - c_x|}{2} \right)^2 \frac{t}{B} + \frac{\pi}{4} \right] + O(t^{-1}) \quad \text{as } t \to \infty. \tag{IV.41}$$

A significant distinction between the 1D-KRK and 2D-KRK solutions is that the peak of the former grows in time in accordance with (IV.40) while the peak of the latter stays constant. Additionally, the 1D-KRK solution response has nontrivial features that extend farther (i.e., larger breadth) than those of the 2D-KRK solution (see Figures IV.7 and IV.8). The difference is further demonstrated by plotting the data sets normalized by their peaks (see C.1.3 for plot).

The difference in the width of the 1D and 2D responses can be partially explained by the fact that the 1D solution exhibits transient growth (Figure IV.9), but the 2D response exhibits no such behavior. Every nonzero $\hat{V}$ value in the 2D case immediately starts decaying, as evidenced by the derivative of h in (IV.12a) with respect to t,

$$\left.\frac{\partial h}{\partial t}\right|_{t=0} = -\frac{A\hat{V}^2}{16B^2\pi}. \tag{IV.42}$$

Past the transience, the solutions for every nonzero $\hat{V}$ decay faster in the 2D case (i.e., $O(1/t)$ from (IV.13)) than in the 1D case (i.e., $O(t^{-1/2})$ from (IV.40)), further curtailing the peak width. In both cases, the convective term does not change the shape of the disturbance, it only translates it in a given direction. For the 2D solution, this can be seen explicitly in the similarity solution (IV.12a), where h is a function of the velocity relative to the traveling peak rather than that relative to the origin.

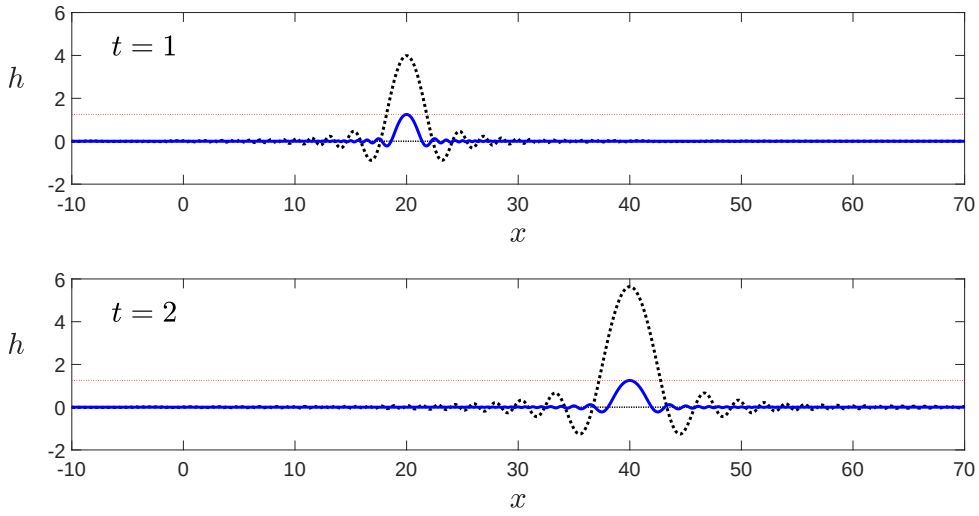

Figure IV.7: Comparison between the convective solutions of 1D-KRK (dotted black curve) and 2D-KRK (solid blue curve) for $t = 1$ and $t = 2$. Short times are chosen to capture the behavior of 1D-KRK before the algebraic growth swamps out the constant height of 2D-KRK. Red horizontal lines mark the height of the 2D peak, which remains constant. The 1D-KRK response is generated using (IV.39a), and the 2D-KRK response is generated using (IV.12), both with $A = 10$ and $B = 1$.

Overall, we see that the 1D-KRK response grows algebraically in (IV.40) compared to the constant height of the 2D-KRK peak in (IV.13) and this reduction in amplitude by a factor of $t^{1/2}$ carries over to other fixed velocities. In particular, as noted above, the 1D-KRK response goes as $t^{-1/2}$ from (IV.41) and in 2D-KRK, the response goes as $1/t$ from (IV.14).

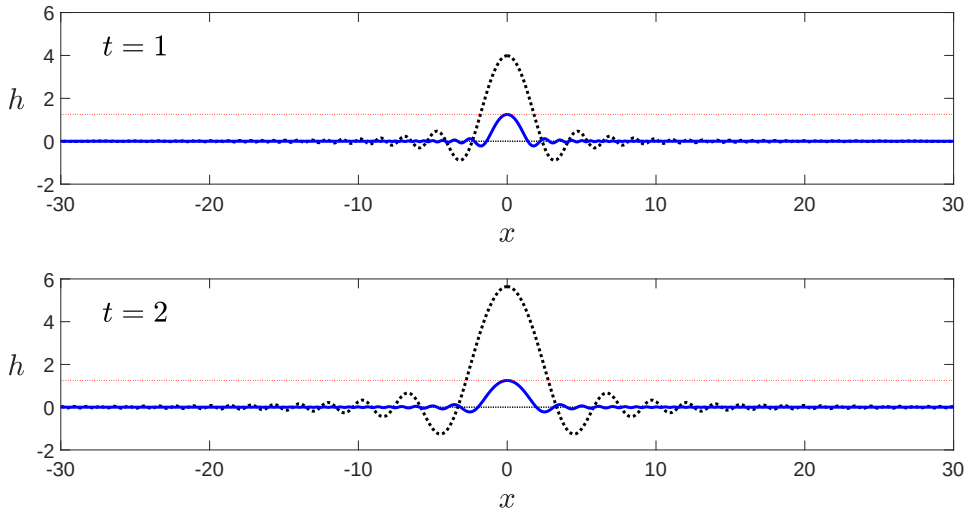

Figure IV.8: Comparison between the non-convective ($c = 0$ for 1D, $c_x = c_z = 0$ for 2D) solutions of 1D-KRK (dotted black curve) and 2D-KRK (solid blue curve) for $t = 1$ and $t = 2$. Short times are chosen to capture the response features of 1D-KRK before the growing peak makes the axis scale too large to see the solution features of the 2D-KRK. Red horizontal lines mark the height of the 2D peak, which remains constant. The 1D-KRK response is generated using (IV.39a), and the 2D-KRK response is generated using (IV.12), both with $A = 10$ and $B = 1$.

IV.4.2 Comparison between 1D-CMH and 2D-CMH

We now compare and contrast the 2D-CMH response propagation determined in Section IV.3 with the 1D-CMH responses from previous work. To enable comparison, we write the 1D solution from [16] without convective terms and with only a forcing disturbance as

$$h(x,t)\Big|_{V_x\neq 0} \sim \frac{e^{-\frac{V_x^2}{8}t}}{\sqrt{3\pi t}}\left(\frac{4A}{V_x^2}\right)\cos\left[\frac{\sqrt{3}V_x^2 t}{8}\right] \quad \text{as } t\to\infty. \tag{IV.43}$$

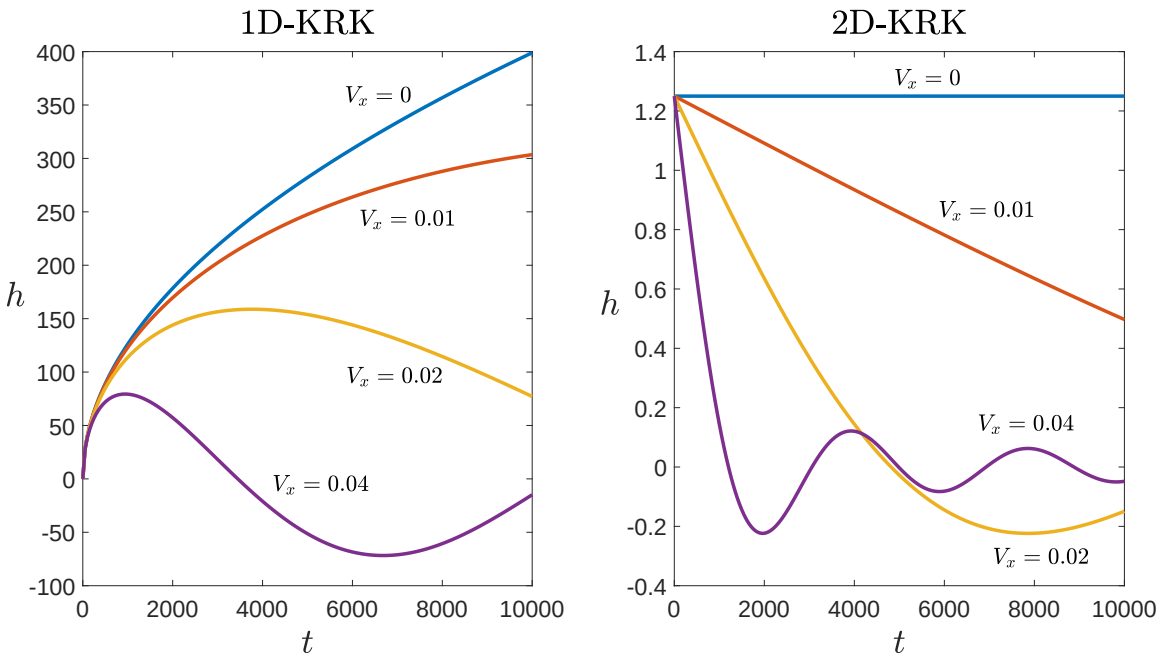

Figure IV.9: Non-convective results for small velocities (i.e., fixed velocities $V_x \equiv {}^{x}/_{t}$) for the 1D- and 2D-KRK. In the 1D problem (left), the solution will grow transiently along non-zero velocities, but will ultimately decay in time. In the 2D problem (right), the solution immediately starts decaying along all non-zero velocities. The data for both cases were generated with the impulsive forcing amplitude of $A = 10$, the parameter value of $B = 1$, and the underlying velocities of $c_x = c_z = 0$. The 1D-KRK response is generated using the exact solution (IV.39a) adapted from [15] with $c = 0$. The 2D solution is generated using (IV.12).

The behavior of (IV.43) for $V_x = 0$ is given exactly in [16] as

$$h(x,t)\Big|_{V_x=0} = A\sqrt{\frac{t}{3\pi}}. \tag{IV.44}$$

A significant distinction between the 1D-CMH and 2D-CMH solutions is that the peak of the former grows in time in accordance with (IV.44) while the peak of the latter stays constant in accordance with (IV.29). Figure IV.10 provides a comparison of the 1D-CMH and

2D-CMH solutions obtained via the Fourier Series Solution (FSS) provided in C.2.1.

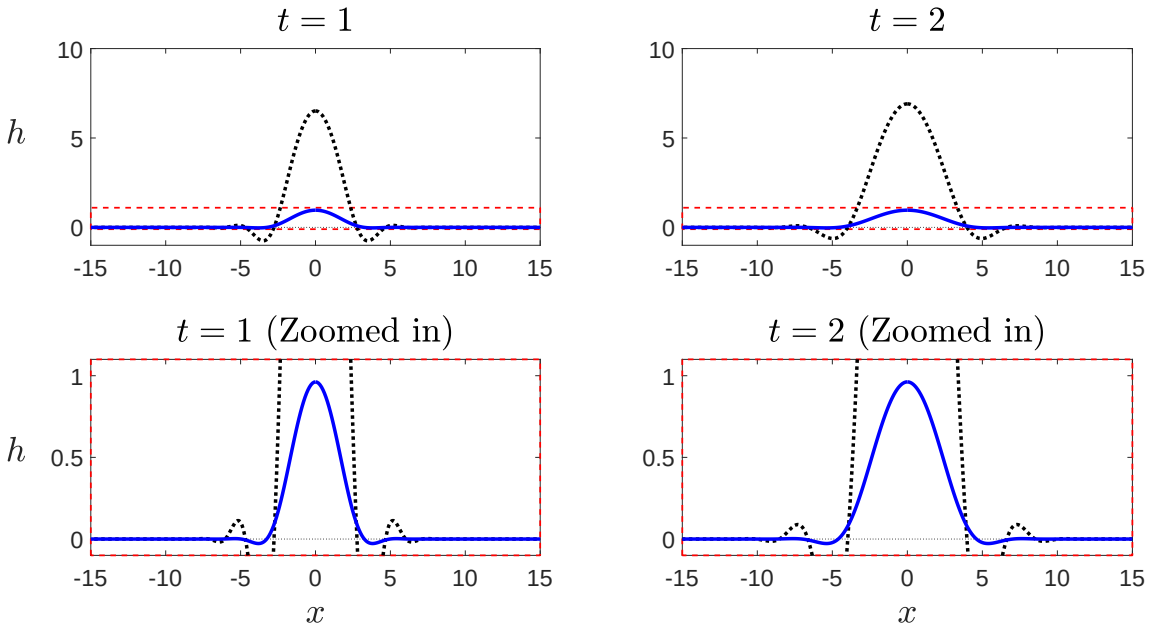

Figure IV.10: Comparison between the 1D solution (dotted black line) of [16] and the 2D solution (IV.22) (solid blue line). Both solutions are generated using the FSS (Appendix C.2.1) with $A = 10$. The top row is zoomed out to show both solutions. The bottom row is zoomed in on the red dashed region to show that the 2D solution has the same structure as the 1D solution, just on a smaller scale.

As with the previous operator, there is a large difference in amplitude between the 1D and 2D cases. At the velocity of the peak, $V_x = 0$ (equivalent to $\hat{V} = 0$ for the 2D case), the 1D-CMH solution grows algebraically as $t^{1/2}$ from (IV.44) and the 2D-CMH solution is a constant from (IV.29). For nonzero $\hat{V}$, the increase in dimension leads to a decay rate in 2D-CMH of the form $e^{-t}(t^{-1})$ from (IV.38a) which is a factor of $t^{-1/2}$ faster than the decay rate in 1D-CMH of $e^{-t}(t^{-1/2})$ from (IV.43). Unlike the behavior shown in figure IV.8, both cases here have the same controlling factor of e^{-t}. As such, there is not a noticeable

difference between the widths of the responses.

IV.5. Conclusions

The linear operators studied by King et al. [15] and Huber et al. [16] have been extended to 2D through an identical methodology; time derivatives are kept the same, and spatial derivatives are replaced with 2D del operators. For both operators, we find that an increase in the dimensionality leads to a decrease in growth rates and an increase in decay rates. The changes are equivalent for both operators, and scale the response character by a factor of $t^{-1/2}$. The algebraic growth of $t^{1/2}$ at the peak velocities in both [15] and in [16] is reduced to a constant height proportional to t^0. Along all the other velocities, the behavior is reduced from $(t^{-1/2})$ and $(e^{-\hat{V}/8}t^{-1/2})$ to (t^{-1}) and $(e^{-\hat{V}/8}t^{-1})$ respectively. The propagation of wave features in 2-D expand as $t^{1/2}$, which is slightly more slowly than the corresponding 1D case for the KRK operator. Both solutions can be expressed in terms of the similarity variable Φ (in 2D-KRK, for all time; in 2D-CMH, only for large time) which couples time and the radial velocity relative to the peak and allows for relevant features of the solutions to be extracted.

Chapter V

Conclusions

Three types of problems have been examined that demonstrate a breakdown of classical stability analysis at neutral stability. For the problem of thin-film flow along an incline that is predicted as being neutrally stable [27] at or below a critical value of the Reynolds number, we discovered that responses, in fact, decay as $t^{-1/4}$ at the critical value and decay as $t^{-1/2}$ below the critical value. For the 2D extension of 1D algebraically unstable flows [15, 16], we find that the change of dimension results in a reduction in the response by a factor of $t^{1/2}$; this is consistent with the results of Lighthill [14] for neutrally stable (but algebraically decaying) water waves. Lastly, we showed that when a 1D algebraically growing flow is subjected to localized oscillatory forcing (i.e, "the signaling problem"), the algebraically growing peak persists, but the forcing induces distinct upstream and downstream responses that neither grow nor decay in time. In contrast to prior work on convectively unstable signaling problems [35, 36, 37], where a spatially growing wave envelopes are predicted, here we are instead able to predict the constant amplitudes of regions within the neutrally

stable wave packet. In all the problems considered, long-time asymptotic analysis is utilized to extract the features described above analytically. Future avenues of research are to examine other operators which demonstrate neutral stability through the same methods to evaluate the generality of the conclusions drawn in this work. Specifically, one could examine the signaling problem for 1D inclined plane film flow (Chapter II) and also the effect of an additional spatial dimension on the flow's stability. Additionally, one could examine signaling in 2D spatial problems to establish how long time forced solutions evolve through a 2D propagating transient.

Bibliography

[1] EA Ibrahim. Spatial instability of a viscous liquid sheet. *Journal of Propulsion and Power*, 11(1):146–152, 1995.

[2] Sung Lin. *Breakup of liquid sheets and jets.* Cambridge University Press, 2003.

[3] Mohamed F El-Sayed, GM Moatimid, FMF Elsabaa, and MFE Amer. Hydrodynamic instabilities of two viscoelastic liquid sheet models in an inviscid gas medium. *Atomization and Sprays*, 25(2), 2015.

[4] Edward Cohen and Edgar Gutoff. *Modern Coating and Drying Technology.* Wiley, 1992.

[5] Stephan F Kistler and Peter M Schweizer. *Liquid film coating.* Springer, 1997.

[6] Steven J Weinstein and Kenneth J Ruschak. Coating flows. *Annu. Rev. Fluid Mech.*, 36:29–53, 2004.

[7] Lord Rayleigh. On the stability of certain fluid motions. *Proc. Math. Soc. Lond.*, 11:57–70, 1880.

[8] S. Chandrasekhar. *Hydrodynamic and Hydromagnetic Stability.* Clarendon Press, 1968.

[9] P Huerre. *Perspectives in Fluid Dynamics*, chapter Open shear flow instabilities, pages 159–229. Cambridge University Press, 2000.

[10] Peter J Schmid and Dan S Henningson. *Stability and transition in shear flows*. Springer Science & Business Media, 2001.

[11] Philip G Drazin and William Hill Reid. *Hydrodynamic stability*. Cambridge University Press, 2004.

[12] P. Huerre and M. Rossi. Hydrodynamic instabilities in open flows. In C. Godrèche and P. Manneville, editors, *Hydrodynamics and Nonlinear Instabilities*, pages 81–288. Cambridge University Press, 1998.

[13] Gerald Beresford Whitham. *Linear and nonlinear waves*, volume 42. John Wiley & Sons, 2011.

[14] James Lighthill. *Waves in fluids*. Cambridge University Press, 2001.

[15] K. R. King, S. J. Weinstein, P. M. Zaretzky, M. Cromer, and N. S. Barlow. Stability of algebraically unstable dispersive flows. *Phys. Rev. Fluids*, 1(073604), 2016.

[16] Colin Huber, Meaghan Hoitt, Nathaniel S Barlow, Nicole Hill, Kimberlee Keithley, and Steven J Weinstein. On the stability of waves in classically neutral flows. *IMA Journal of Applied Mathematics*, 85(2):309–340, 04 2020.

[17] Colin M Huber, Nathaniel S Barlow, and Steven J Weinstein. On the two-dimensional extension of one-dimensional algebraically growing waves at neutral stability. 2022.

[18] Edward L Paul, Victor A Atiemo-Obeng, and Suzanne M Kresta. *Handbook of industrial mixing: science and practice*. John Wiley & Sons, 2004.

[19] X. Wu. Nonlinear theories for shear flow instabilities: Physical insights and practical implications. *Annu. Rev. Fluid Mech.*, 51:451–485, 2019.

[20] KM Case. Stability of inviscid plane couette flow. *Physics of Fluids (1958-1988)*, 3(2):143–148, 1960.

[21] N. S. Barlow, B. T. Helenbrook, S. P. Lin, and S. J. Weinstein. An interpretation of absolutely and convectively unstable waves using series solutions. *Wave Motion*, 47(8):564–582, 2010.

[22] Luigi De Luca and Michela Costa. Instability of a spatially developing liquid sheet. *J. Fluid Mech.*, 331:127–144, 1997.

[23] N. S. Barlow, B. T. Helenbrook, and S. P. Lin. Transience to instability in a liquid sheet. *J. Fluid Mech.*, 666:358–390, 2011.

[24] H. Schlichting. *Boundary Layer Theory*. McGraw-Hill, seventh edition, 1979.

[25] P. Manneville. Overview. In C. Godrèche and P. Manneville, editors, *Hydrodynamics and Nonlinear Instabilities*, pages 1–24. Cambridge University Press, 1998.

[26] G. Joulin and P. Vidal. An introduction to the instability of flames, shocks, and detonations. In C. Godrèche and P. Manneville, editors, *Hydrodynamics and Nonlinear Instabilities*, pages 493–673. Cambridge University Press, 1998.

[27] C-S Yih. Stability of liquid flow down an inclined plane. *Phys. Fluids*, 6(3):321–334, 1963.

[28] L. Brevdo, P. Laure, F. Dias, and T. J. Bridges. Linear pulse structure and signaling in a film flow on an inclined plane. *J. Fluid Mech.*, 396:37–71, 1999.

[29] S. V. Alekseenko, V. E. Nakoryakov, and B. G. Pokusaev. *Wave flow of liquid films*. Begell House, 1994.

[30] Th. von Kármán. Über laminare und turbulente reibung. *ZAMM*, 1:233–252, 1921.

[31] K. Pohlhausen. Zur näherungsweisen integration der differentialgleichung der laminaren reibungsshicht. *ZAMM*, 1(252-268), 1921.

[32] P. J. Pritchard. *Fox and McDonald's Introduction to Fluid Mechanics*. Wiley, 8 edition, 2011.

[33] S. J. Weinstein. Wave propagation in the flow of shear-thinning fluids down an incline. *AIChE J.*, 36(12):1873–1889, 1990.

[34] Carl M Bender and Steven A Orszag. *Advanced Mathematical Methods for Scientists and Engineers I*. Springer Science & Business Media, 1999.

[35] J. M. Gordillo and M. Pérez-Saborid. Transient effects in the signaling problem. *Phys. Fluids*, 14(12):4329–4343, 2002.

[36] N. S. Barlow, B. T. Helenbrook, and S. J. Weinstein. Algorithm for spatio-temporal analysis of the signaling problem. *IMA J. Appl. Math.*, 82:1–32, 2017.

[37] N. S. Barlow, S. J. Weinstein, and B. T. Helenbrook. On the response of convectively unstable flows to oscillatory forcing with application to liquid sheets. *J. Fluid Mech.*, 699:115–152, 2012.

[38] M. Abramowitz and I Stegun. *Handbook of Mathematical Functions*, page 377. Dover, 1972.

[39] Wolfram|Alpha. `https://www.wolframalpha.com/input?i=expansion+of+modified+bessel+of+the+first+kind+as+z+goes+to+infinity`.

[40] Norman Bleistein. *Mathematical methods for wave phenomena*. Academic Press, 1984.

[41] I. S. Gradshteyn and I. M. Ryzhik. *Table of integrals, series, and products: seventh edition*. Academic Press, 2007.

[42] Wolfram|Alpha. `https://www.wolframalpha.com/input?i=integrate+x%5E%28-1%2F2%29*e%5E%28-b*x%5E2%29*sin%28c*x%29+from+0+to+infinity%2C+real%28b%29%3E0`.

[43] Wolfram|Alpha. `https://www.wolframalpha.com/input?i=integrate+x%5E%28-3%2F2%29*e%5E%28-b*x%5E2%29*sin%28c*x%29+from+0+to+infinity%2C+real%28b%29%3E0`.

Appendix A

Appendix: On the stability of waves in classically neutral flows

A.1. Appendix: Justification for asymptotic equivalence in (II.16)

We now justify that the 2nd term in (II.15c) is subdominant to the first, which leads to the asymptotic equivalence shown in (II.16) as $t \to \infty$. The typical approach to follow is to rewrite the integral (II.15c) in two pieces as:

$$h(x,t) = h_1(x,t) + h_2(x,t) \tag{A.1a}$$

where

$$h_1(x,t) = \frac{1}{2\pi} \int_{-\infty}^{\infty} C_1(k) e^{\phi_1(k)t} dk, \quad h_2(x,t) = \frac{1}{2\pi} \int_{-\infty}^{\infty} C_2(k) e^{\phi_2(k)t} dk. \tag{A.1b}$$

In (A.1a), the path of integration is taken along the real axis as written. It suffices, then to show that $h_2 \ll h_1$ as $t \to \infty$ to justify equation (II.16). Interestingly, the integral h_2 cannot be evaluated via standard techniques in the $t \to \infty$ limit. In particular, the two typical methods at our disposal — the method of steepest descent and integration by parts — fail as follows.

When the method of steepest descent is used, the integral h_2 along the real k-axis is evaluated as part of a complex contour integral, and the topology of the complex phase function $\phi_2(k)$ is configured such that saddle points, k_s, have lower Real$[\phi_2(k_s)]$ values than surrounding regions of the plane. Figure A.1 shows a typical case that represents the situation for all x/t rays evaluated in this chapter. The indicated saddle points cannot be accessed via a contour integral that includes the real axis (or even a portion of it denoted as the contour C in Figure A.1) in such a way that the saddle points have a maximum Real$[\phi_2(k_s)]$ along the deformed contour, and the method fails.

The method of integration by parts fails precisely because the integral $h_2(x,t)$ is convergent in the infinite domain of k. This requires its integrand go to zero as $k \to \pm\infty$ (and it does, based on the contours in Figure A.1), and as a result repeated integration by parts merely yields a zero result and no asymptotic behavior can be extracted.

A different approach is thus necessary to prove the assertion that $h_2(x,t)$ is subdominant. To do so, we return to the form of the integral in (II.15c) and compare the magnitude of the terms in the integrand directly at each value of k (recall that k is real as the path of integration lies along the real axis). We denote the two pieces of the integrand as:

$$I_1 = C_1(k)e^{\phi_1(k)t}, \quad I_2 = C_2(k)e^{\phi_2(k)t}, \tag{A.2a}$$

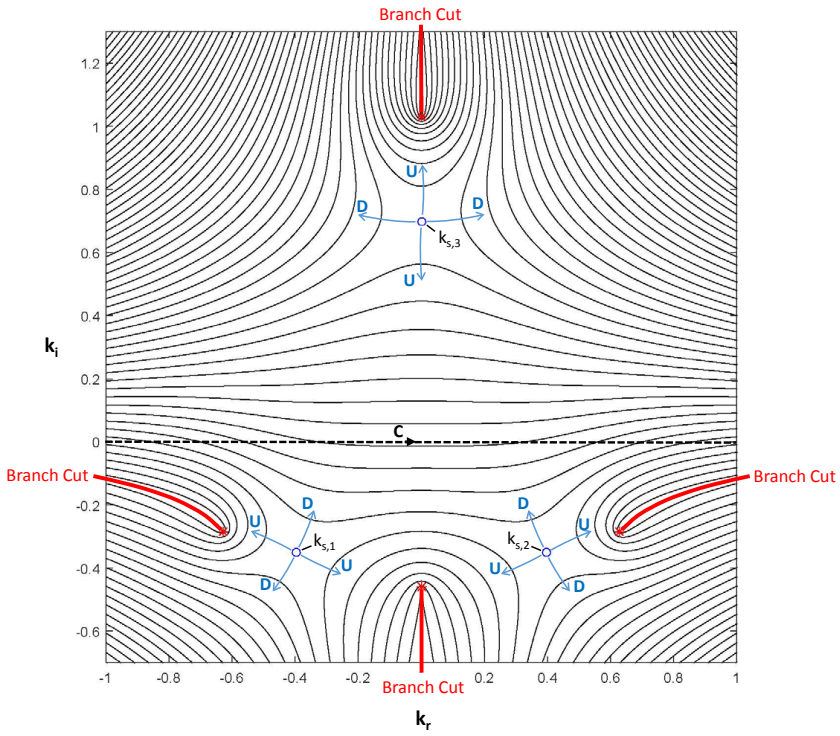

Figure A.1: Contours of constant Real$[\phi_2(k)]$ vs complex $k = k_r + ik_i$ at neutral stability ($Re = \cot\theta$) for $x/t = 3$, $\theta = \pi/4$, and $We = 0.1$. There are 3 saddle points ($\circ$) denoted as $k_{s,j}$ for $j \in [1, 3]$. Branch points ($*$) and branch cuts are taken in accordance with the principal values of the square roots in (II.15a). The directions in which Real$[\phi_2(k)]$ decrease and increase are indicated with arrows using the notation D and U, respectively. The orientation of the saddles does not enable a closed contour to be drawn that includes the contour **C** (the real axis) and also has Real$[\phi_2(k_{s,j})]$ as a maximum along the contour. Thus, all the saddle points are spurious, i.e., none may be used via the method of steepest decent to determine the long time asymptotic behavior of the 2nd term in the integral of (II.15c). For reference, the location of the saddles and associated contour values are as follows: $k_{s,1} = -0.2957 - 0.2492i$, Real$[\phi_2(k_{s,1})] = -2.4192$; $k_{s,2} = 0.2957 - 0.2492i$, Real$[\phi_2(k_{s,2})] = -2.4192$; $k_{s,3} = 0.6976i$, Real$[\phi_2(k_{s,3})] = -4.3440$.

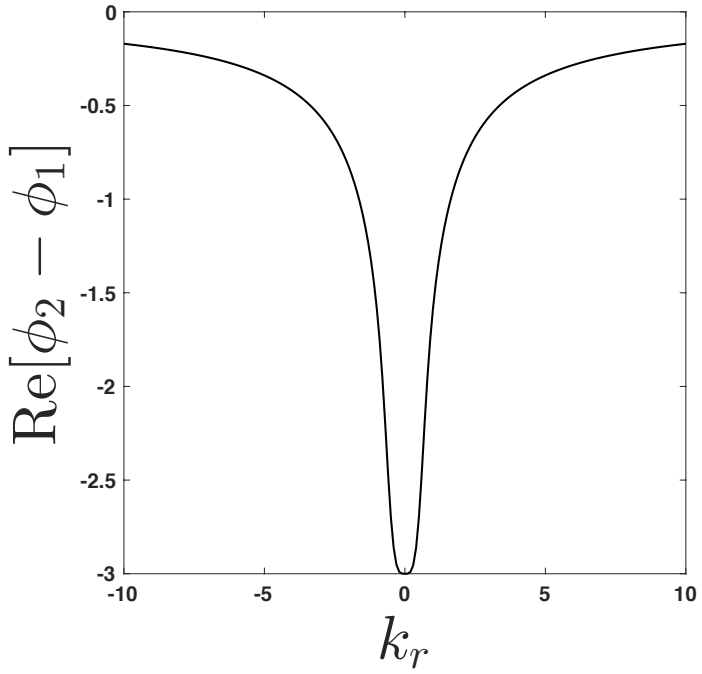

Figure A.2: Plot of Real$[\phi_2(k) - \phi_1(k)]$ vs. k for $Re = \cot(\theta)$, $\theta = \pi/4$, and $We = 0.1$.

and thus using equations (II.15a), (II.15b), (II.15d), we obtain

$$\frac{I_2}{I_1} = \frac{C_2(k)}{C_1(k)} e^{(\phi_2(k)-\phi_1(k))t}, \quad \frac{C_2(k)}{C_1(k)} = \left(\frac{iu_0 - \omega_1 h_0}{\omega_2 h_0 - iu_0}\right), \quad \phi_2(k) - \phi_1(k) = -\sqrt{\beta^2 - 4\gamma}, \tag{A.2b}$$

where all parameters are defined in equations (II.8) and (II.15). As $t \to \infty$, the real part of the exponential in equation (A.2b) governs the magnitude of the ratio I_2/I_1; a typical plot of the growth rate in the exponential, Real$[\phi_2(k) - \phi_1(k)]$ vs. k is given in Figure A.2. Figure A.2 indicates that as $t \to \infty$, the magnitude of $I_2/I_1 \to 0$ for finite k. However, as the domain of k is increased toward $\pm\infty$ (not shown here), the plot asymptotes to zero, indicating that the growth rates are comparable there. Furthermore, the magnitude of the ratio $C_2(k)/C_1(k)$ in (A.2b) approaches 1 in these limits. Thus, for all finite values of k, we can certainly establish that I_2 is subdominant to I_1 as $t \to \infty$, but this result is not proven

in the limit of infinite k. This also indicates that in (A.1b), $h_2 \ll h_1$ as $t \to \infty$ if finite bounds are taken on the indicated integrals instead of the infinite limits indicated.

To complete the proof that $h_2 \ll h_1$ as $t \to \infty$, we rewrite the equations for h_1 and h_2 in (A.1b) as

$$h_1(x,t) = \frac{1}{2\pi}\int_{-\infty}^{-L} C_1(k)e^{\phi_1(k)t}dk + \frac{1}{2\pi}\int_{-L}^{L} C_1(k)e^{\phi_1(k)t}dk + \frac{1}{2\pi}\int_{L}^{\infty} C_1(k)e^{\phi_1(k)t}dk, \quad \text{(A.3a)}$$

$$h_2(x,t) = \frac{1}{2\pi}\int_{-\infty}^{-L} C_2(k)e^{\phi_2(k)t}dk + \frac{1}{2\pi}\int_{-L}^{L} C_2(k)e^{\phi_2(k)t}dk + \frac{1}{2\pi}\int_{L}^{\infty} C_2(k)e^{\phi_2(k)t}dk, \quad \text{(A.3b)}$$

where $L > 0$ is a finite number. We have already established that the finite bound integral in (A.3b) is subdominant to the corresponding finite bound integral in (A.3a) from Figure A.2 and the preceding arguments (in Figure A.2, $L = 10$ as indicated). Integration by parts may be used on the remaining semi-infinite integrals in equation (A.3a) and (A.3b) to yield

$$\begin{aligned}
\frac{1}{2\pi}\int_{-\infty}^{-L} C_1(k)e^{\phi_1(k)t}dk &\sim \frac{C_1(-L)}{2\pi t\ \left.\frac{d\phi_1(k)}{dk}\right|_{k=-L}} e^{\phi_1(-L)t}, \\
\frac{1}{2\pi}\int_{L}^{\infty} C_1(k)e^{\phi_1(k)t}dk &\sim -\frac{C_1(L)}{2\pi t\ \left.\frac{d\phi_1(k)}{dk}\right|_{k=L}} e^{\phi_1(L)t}, \qquad \text{(A.4a)}
\end{aligned}$$

$$\begin{aligned}
\frac{1}{2\pi}\int_{-\infty}^{-L} C_2(k)e^{\phi_2(k)t}dk &\sim \frac{C_2(-L)}{2\pi t\ \left.\frac{d\phi_2(k)}{dk}\right|_{k=-L}} e^{\phi_2(-L)t}, \\
\frac{1}{2\pi}\int_{L}^{\infty} C_2(k)e^{\phi_2(k)t}dk &\sim -\frac{C_2(L)}{2\pi t\ \left.\frac{d\phi_2(k)}{dk}\right|_{k=L}} e^{\phi_2(L)t} \text{ as } t \to \infty. \qquad \text{(A.4b)}
\end{aligned}$$

We thus see that

$$\frac{\frac{1}{2\pi}\int_{-\infty}^{-L} C_2(k)e^{\phi_2(k)t}dk}{\frac{1}{2\pi}\int_{-\infty}^{-L} C_1(k)e^{\phi_1(k)t}dk} = O(e^{(\phi_2(-L)-\phi_1(-L))t}),$$

$$\frac{\frac{1}{2\pi}\int_{L}^{\infty} C_2(k)e^{\phi_2(k)t}dk}{\frac{1}{2\pi}\int_{L}^{\infty} C_1(k)e^{\phi_1(k)t}dk} = O(e^{(\phi_2(L)-\phi_1(L))t}) \text{ as } t \to \infty. \tag{A.5}$$

Since according to Figure A.2, which is representative for all cases examined in this chapter, $\text{Real}[\phi_2(k) - \phi_1(k)] < 0$ for finite k, this indicates that the ratios in (A.5) go to zero as $t \to \infty$. Thus, we see that all integrals in (A.3b) are subdominant to those in (A.3a) for all real k, which establishes that $h_2 \ll h_1$ as $t \to \infty$ in (A.1). This furthermore establishes the asymptotic equivalence indicated in equation (II.16) of the main text. This conclusion is also demonstrated by the agreement between our numerical solutions and the $t \to \infty$ asymptotic behavior of equation (II.16).

A.2. Appendix: Long time asymptotic solution to (II.16)

The following analysis is separated into two subsections based on a structural change in the dispersion relation for flow down an incline plane. Classical analysis tells us that, for $Re \leq \cot(\theta)$, the wavenumber of maximum growth is $k = 0$ (see Figure II.3) and that the exponential growth rate is zero. Note that, by definition (II.18b), a maximum in $\omega_i(k_r)$ is a saddle point. Any such maximum is also a contributing saddle point, in that a steepest descent path can be closed back to the real-axis (see [36], Appendix A). Applying definition (II.18a) to (II.11), we find that the corresponding ray of maximum growth is $x/t = 3$. Thus, for $Re \leq \cot(\theta)$, the peak of a wave packet travels at a velocity $x/t = 3$ as

it flows down the incline plane. The explicit knowledge of the (k_s, x/t) pair at the peak allows us to make simplifications outlined above. For $x/t \neq 3$, the saddle locations and their corresponding steepest descent paths are less straightforward to deduce. For this reason, we separate the following evaluation of integral (II.16) into two subsections — one for the peak along $x/t = 3$ and one for the "off-peak" rays $x/t \neq 3$.

A.3. Appendix: Evaluation of (II.16) for $x/t = 3$ and $Re \leq \cot(\theta)$

Here, we apply the method of steepest descent to the integral (II.16) for $x/t = 3$, which corresponds to the contributing saddle $k_s = 0$. Expanding $\phi_1(k)$ (given by (II.15d)) about $k = 0$, and making direct use of (II.11), we obtain the following

$$\begin{aligned}\phi_1(k) \sim{}& \left[Re - \cot(\theta)\right] k^2 - \frac{6}{5} iRe \left[Re - \cot(\theta)\right] k^3 \\ &+ \left\{ \frac{36}{25} Re^2 \left[Re - \cot(\theta)\right] - \frac{12}{5} \mathrm{Re}^3 c \left[Re - \cot(\theta)\right]^2 - \frac{Re}{3We} \right\} k^4 + O(k^5), \quad k \to 0,\end{aligned} \tag{A.6}$$

and thus

$$\phi_1(k) \sim \left[Re - \cot(\theta)\right] k^2, \ Re < \cot(\theta) \tag{A.7a}$$

$$\phi_1(k) \sim -\frac{\mathrm{Re}}{3We} k^4, \ Re = \cot(\theta) \tag{A.7b}$$

which indicates that $k_s = 0$ is a 2^{nd} order saddle for $Re < \cot(\theta)$ and a 4^{th} order saddle for $Re = \cot(\theta)$, according to definition (II.17). Substituting $k = 0$ into $C_1(k)$ and (A.7) for

$\phi_1(k)$ in (II.16) leads to

$$h\left(x,t\right)|_{\frac{x}{t}=3} \sim \frac{1}{2\pi}\left(h_0 + u_0\ Re/3\right)\int\limits_{-\infty}^{\infty} e^{-[\cot(\theta)-Re]k^2t}\ dk \text{ as } t\to\infty,\ Re<\cot(\theta),$$

$$h\left(x,t\right)|_{\frac{x}{t}=3} \sim \frac{1}{2\pi}\left(h_0 + u_0\ Re/3\right)\int\limits_{-\infty}^{\infty} e^{-\frac{Re}{3We}k^4t}\ dk \text{ as } t\to\infty,\ Re=\cot(\theta), \quad \text{(A.8)}$$

where the integration path remains along the real line, since the argument of the exponential is purely real and thus no rotation through the saddle is required. Since the integrands of (A.8) are even, the integrals may be rewritten

$$h\left(x,t\right)|_{\frac{x}{t}=3} \sim \frac{1}{\pi}\left(h_0 + u_0\ Re/3\right)\int\limits_{0}^{\infty} e^{-[\cot(\theta)-Re]k^2t}\ \ dk \text{ as } t\to\infty,\ Re<\cot(\theta), \quad \text{(A.9a)}$$

$$h\left(x,t\right)|_{\frac{x}{t}=3} \sim \frac{1}{\pi}\left(h_0 + u_0\ Re/3\right)\int\limits_{0}^{\infty} e^{-\frac{Re}{3We}k^4t}\ dk \text{ as } t\to\infty,\ Re=\cot(\theta). \quad \text{(A.9b)}$$

Upon making the variable substitutions $v = \left[\cot(\theta) - Re\right]k^2t$ and $v = \frac{Re}{3We}k^4t$ in (A.9a) and (A.9b) respectively, we obtain

$$h\left(x,t\right)|_{\frac{x}{t}=3} \sim \frac{\left(h_0 + u_0\ Re/3\right)}{\pi p\sqrt{\left[\cot(\theta) - Re\right]t}}\int\limits_{0}^{\infty} e^{-v}v^{\frac{1}{2}-1}\ \ dv \text{ as } t\to\infty,\ Re<\cot(\theta), \quad \text{(A.10)}$$

$$h\left(x,t\right)|_{\frac{x}{t}=3} \sim \frac{\left(h_0 + u_0\ Re/3\right)}{\pi p\left\{\frac{\mathrm{Re}}{3We}t\right\}^{1/4}}\int\limits_{0}^{\infty} e^{-v}v^{\frac{1}{4}-1}\ \ dv \text{ as } t\to\infty,\ Re=\cot(\theta), \quad \text{(A.10)}$$

where the integrals above evaluate to $\Gamma(1/2)$ and $\Gamma(1/4)$ respectively, leading to the results given in (II.19a) and (II.19b).

A.4. Appendix: Evaluation of (II.16) for $x/t \neq 3$ and $Re \leq \cot(\theta)$

Saddles associated with the off-peak rays $x/t \neq 3$ lie in the complex k-plane, off of the real-line. Thus we must take care to evaluate integral (II.16) along a closed path that joins

the original path (the k_r-axis) with a path through the saddle, such that Real$[\phi(k_s)]$ is a maximum along this path. This allows for the integral to be replaced with an approximation near the saddle as $t \to \infty$. A representative example is given in Figure A.3 for $x/t = 2$ (parameter values given in the caption). Note that there are 3 saddle points associated with $x/t = 2$, as indicated by $\bullet$'s in Figure A.3, but only the two lying in the lower half plane are accessible as maxima along a closed path with the real axis. The steepest descent contour $\int_{\text{SD}}$ is shown by a dashed line. Note that neither the branch points (indicated by $*$'s) nor any other singularities are enclosed between the real axis and the steepest descent path, and so we may apply Cauchy's theorem to obtain

$$h\left(x,t\right)|_{\frac{x}{t}\neq 3} \sim \frac{1}{2\pi}\int_{-\text{SD}} C_1(k)e^{\phi_1(k)t}dk \text{ as } t\to\infty,\ Re \leq \cot(\theta) \tag{A.11}$$

where $\int_{\text{-SD}}$ denotes a path from left to right (opposite that shown in Figure A.3) and the long-time asymptotic casting in (A.11) is solely due the omission of the $\phi_2(k)$ term in (II.15), and not from the path deformation. As Reynolds number, Weber number, θ, and x/t vary, the location of the saddles differ from that shown in Figure A.3. However, there is always either one or two contributing saddles where Cauchy's theorem may be applied such that (A.11) holds. Additionally, since all $x/t \neq 3$ saddles are 2^{nd}-order, a general asymptotic solution may be formulated according to the method of steepest descent by looking in the vicinity of the saddles, replacing $C_1(k)$ with $C_1(k_s)$, $\phi(k)$ with its 2^{nd}-order

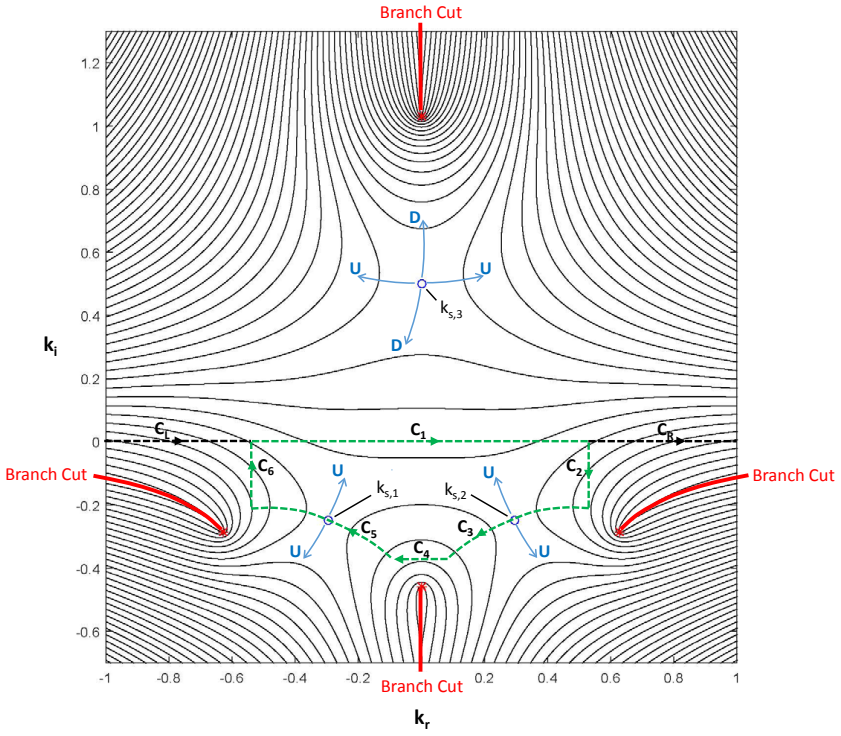

Figure A.3: Contours of constant Real$[\phi_1(k)]$ vs complex $k = k_r + ik_i$ at neutral stability ($Re = \cot\theta$) for $x/t = 2$, $\theta = \pi/4$, and $We = 0.1$. Notation is the same as in Figure A.1. The orientation of the saddles enables a closed contour (indicated by dashed lines) to be drawn through $k_{s,1}$ and $k_{s,2}$ that includes a portion of the real axis, $\mathbf{C}_1$, and also has Real$[\phi_1(k_{s,j})]$ as a maximum along the contour — thus, the method of steepest decent may be used to determine the long time asymptotic behavior of the integral involving $\phi_1(k)$ in (II.15c) along the contour $\mathbf{C}_1$. Alternatively, the orientation of saddle $k_{s,3}$ makes it spurious (does not contribute to the asymptotic behavior) and is not accessible by connection to any real contour. The path of integration in (II.15c) is the infinite k_r-axis, i.e. consists of the contour $\mathbf{C}$=$\mathbf{C}_\mathrm{L}$∪$\mathbf{C}_1$∪$\mathbf{C}_\mathrm{R}$; however, it can be shown via integration by parts that the contributions over $\mathbf{C}_\mathrm{L}$ and $\mathbf{C}_\mathrm{R}$ are subdominant to that of $\mathbf{C}_1$, such that the long time asymptotic behavior is determined by the integral $\mathbf{C}_1$ — and thus the saddle points dominate the asymptotic behavior. For reference, the location of the contributing saddles and related quantities necessary to determine the asymptotic behavior using (A.13), (A.14), and (A.24a) are as follows: $a = 0.2957$, $b = 0.2492$, $c = 0.8218$, $d = 0.6805$, $r = 5.9476$, and $q = 5.4227$.

expansion about k_s in (A.11), and rewriting the limits of integration as follows

$$h\left(x,t\right)|_{\frac{x}{t}\neq 3} \sim \frac{1}{2\pi}\Bigg[C_1(k_{s1})e^{\phi_1(k_{s1})}\overbrace{\int_{k_{s1}-\epsilon}^{k_{s1}+\epsilon} e^{\frac{1}{2}\frac{d^2\phi_1}{dk^2}\Big|_{k_{s1}}(k-k_{s1})^2t}dk}^{I_1} + C_1(k_{s2})e^{\phi_1(k_{s2})}\underbrace{\int_{k_{s2}-\epsilon}^{k_{s2}+\epsilon} e^{\frac{1}{2}\frac{d^2\phi_1}{dk^2}\Big|_{k_{s2}}(k-k_{s2})^2t}dk}_{I_2}\Bigg] \text{ as } t\to\infty,\ Re\leq\cot(\theta) \tag{A.12}$$

where ϵ is a small positive constant. Note that in the above we have assumed two contributing saddles k_{s1} and k_{s2}. For cases with two saddles, such as that shown in Figure A.3, the locations of quantities in (A.12) in the complex k-plane are as follows

$$\begin{aligned} k_{s1,2} = \mp a - ib,\ \omega_1(k_{s1,2}) &= \mp c - id, \\ \left.\frac{d^2\phi_1}{dk^2}\right|_{k_{s1,2}} &= -r \mp iq, \\ a,\ b,\ c,\ d,\ q,\ r &> 0, \end{aligned} \tag{A.13}$$

where $k_{s1,2}$ refers to both saddle points. It is useful to write the following quantity from (A.13) in complex polar form

$$r+iq = \rho e^{i\Theta},\ \rho = \sqrt{r^2+q^2},\ \Theta = \tan^{-1}\left(\frac{q}{r}\right),\ \Theta\in\left(0,\frac{\pi}{2}\right) \tag{A.14}$$

from which it follows from (A.13) that

$$\left.\frac{d^2\phi_1}{dk^2}\right|_{k_{s1,2}} = -\rho e^{\pm i\Theta}. \tag{A.15}$$

We now proceed to solve for I_1 (denoted in (A.12)) using the orientation of the path through the saddle k_{s1} shown in Figure A.3. After substituting (A.15) into (A.13) and splitting I_1 into two integrals entering and leaving the saddle k_{s1}, we obtain

$$I_1 = \int_{k_{s1}-\epsilon}^{k_{s1}} e^{-\frac{1}{2}\rho e^{i\Theta}(k-k_{s1})^2t}dk + \int_{k_{s1}}^{k_{s1}+\epsilon} e^{-\frac{1}{2}\rho e^{i\Theta}(k-k_{s1})^2t}dk. \tag{A.16}$$

The split made above is done such that the quantity $(k - k_{s1})$ can be written in complex polar form in accordance with Figure A.3 with the appropriate angle entering and leaving the saddle as follows

$$\begin{aligned} (k - k_{s1}) &= Ue^{i\Psi} \\ \Psi \in \left[\frac{\pi}{2}, \pi\right] &\text{ for } k \in [k_{s1} - \epsilon, k_{s1}] \\ \Psi \in \left[-\frac{\pi}{2}, 0\right] &\text{ for } k \in [k_{s1}, k_{s1} + \epsilon]\,. \end{aligned} \tag{A.17}$$

Upon substituting (A.17) into (A.16), we obtain

$$I_1 = e^{i\Psi} \int_{-\epsilon e^{-i\Psi}}^{0} e^{-\frac{1}{2}\rho U^2 t e^{i(\Theta+2\Psi)}} dU + e^{i\Psi} \int_{0}^{\epsilon e^{-i\Psi}} e^{-\frac{1}{2}\rho U^2 t e^{i(\Theta+2\Psi)}} dU. \tag{A.18}$$

Note that in order for the integrals of (A.18) to represent paths of steepest descent, the argument of the outer exponential must be real and negative, such that following condition must hold between Ψ and Θ [40],

$$\Theta + 2\Psi = 2n\pi \tag{A.19}$$

where $n = 1$ for the first integral of (A.18) (entering the saddle) and $n = 0$ for the second integral of (A.18) (leaving the saddle). In accordance with (A.19), we substitute $\Psi = \pi - \Theta/2$ into the first integral of (A.18) and $\Psi = -\Theta/2$ into the second integral of (A.18) to obtain (after some simplification)

$$I_1 = 2e^{-i\frac{\Theta}{2}} \int_{0}^{\epsilon'} e^{-\frac{1}{2}\rho U^2 t} dU, \tag{A.20}$$

where $\epsilon' = \epsilon e^{i\Theta/2}$ is a real quantity (recall that U is the real-valued magnitude defined in (A.17)). Thus (A.20) is a real integral translated and rotated from its skewed path through

saddle k_{s1} in Figure A.3. We now replace (A.20) with its semi-infinite extension

$$I_1 \sim 2e^{-i\frac{\Theta}{2}} \int_0^\infty e^{-\frac{1}{2}\rho U^2 t} dU \text{ as } t \to \infty, \tag{A.21}$$

noting that (A.21) asymptotically approaches (A.20) as $t \to \infty$. Due the to dominant contribution at the saddle, the added contribution from ϵ' to ∞ in (A.21) will be subdominant to (A.20). The improper integral in (A.21) evaluates exactly to $\sqrt{2\pi/(\rho t)}/2$ (see equation 3.321.3 in [41]), and thus (A.21) becomes

$$I_1 \sim e^{-i\frac{\Theta}{2}} \sqrt{\frac{2\pi}{\rho t}} \text{ as } t \to \infty. \tag{A.22}$$

If we apply the same technique as done above to I_2 in (A.12) involving saddle k_{s2} in Figure A.3, whose real imaginary part is the same but real part opposite sign of k_{s1} and whose steepest descent path is oriented perpendicular to that of k_{s1}, we obtain

$$I_2 \sim e^{i\frac{\Theta}{2}} \sqrt{\frac{2\pi}{\rho t}} \text{ as } t \to \infty. \tag{A.23}$$

Substituting (A.22) and (A.23) into (A.12), using (A.13) to recognize that $\phi_1(k_{s1,2}) = \left[b\left(\frac{x}{t}\right) - d\right] \pm i\left[c - a\left(\frac{x}{t}\right)\right]$ and $C_1(k_{s1}) = \overline{C_1(k_{s2})}$, we obtain

$$h\left(x,t\right)|_{\frac{x}{t}\neq 3} \sim \sqrt{\frac{2}{\rho\pi t}}\, e^{\left(b\frac{x}{t}-d\right)t} \text{ Real}\left\{C_1(k_{s1}) e^{i\left[\left(c-a\frac{x}{t}\right)t - \Theta/2\right]}\right\} \text{ as } t \to \infty,\ a \neq 0,\ Re \leq \cot(\theta), \tag{A.24a}$$

where the $a \neq 0$ condition reminds us that we have assumed two contributing saddles symmetric about the imaginary axis, as shown in Figure A.3 for saddles in the lower-half plane for $x/t = 2$. The result (A.24a) may be applied to contributing saddles in the lower or upper half plane (which is the case for $x/t = 4$, see Figure A.4) if the definitions in (A.13)

are modified as follows

$$a = |\text{Real}[k_s]|\,, \tag{A.24b}$$

$$b = -\text{Imag}[k_s], \tag{A.24c}$$

$$c = |\text{Real}[\omega_1(k_s)]|\,, \tag{A.24d}$$

$$d = -\ \text{sgn}\ (\text{Imag}[ks])\ \ |\text{Imag}[\omega_1(k_s)]|\,, \tag{A.24e}$$

$$r = \left|\text{Imag}\left[\frac{d^2\omega_1}{dk^2}\right]_{k_s}\right|, \tag{A.24f}$$

$$q = -\ \text{sgn}\ (\text{Imag}[ks])\left|\text{Real}\left[\frac{d^2\omega_1}{dk^2}\right]_{k_s}\right|. \tag{A.24g}$$

For $Re < \cot(\theta)$, as either Re is decreased or $x/t \to 3$ (from above or below) the saddles move closer together until they combine on the imaginary axis and thus only one saddle contributes, as shown in Figure A.5. Carrying out the above analysis for this case leads to

$$h\,(x,t)\,|_{\frac{x}{t}\neq 3} \sim \frac{1}{\sqrt{2\rho\pi t}}\ e^{\left(b\frac{x}{t}-d\right)t}\ \text{Real}\left[C_1(k_{s1})e^{i(ct-\Theta/2)}\right]\ \text{as}\ t\to\infty,\quad a=0,\quad Re<\cot(\theta), \tag{A.24h}$$

where b, c, and d correspond to $k_{s,1}$ in Figure A.5.

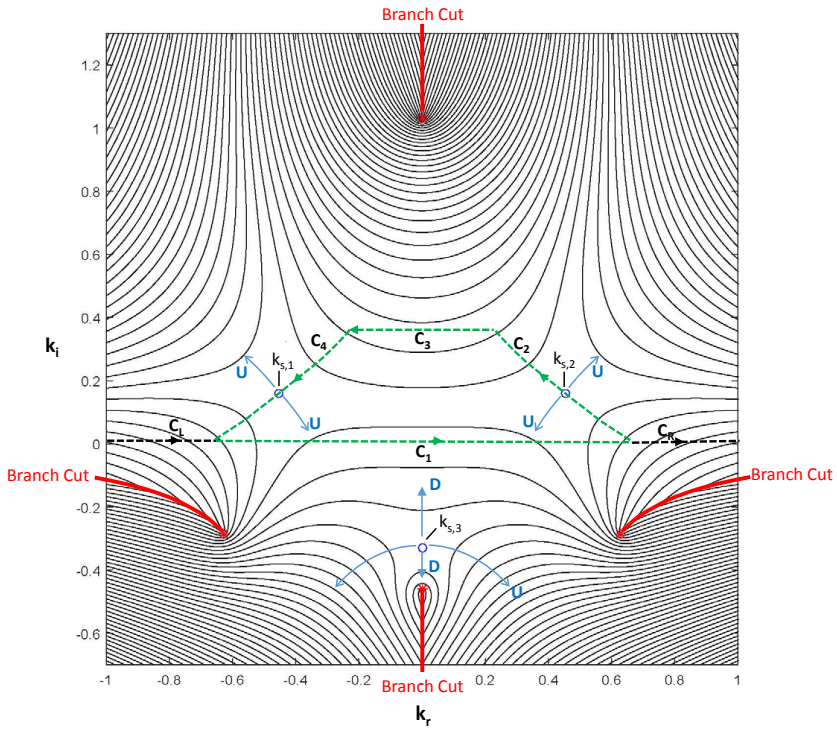

Figure A.4: Contours of constant Real$[\phi_1(k)]$ vs complex $k = k_r + ik_i$ at neutral stability ($Re = \cot\theta$) for $x/t = 4$, $\theta = \pi/4$, and $We = 0.1$. Notation is the same as in Figure A.2 and discussion is the same as in Figure A.3. For reference, the location of the contributing saddles and related quantities necessary to determine the asymptotic behavior using (A.13), (A.14), and (A.24a) are as follows: $a = 0.4528$, $b = 0.1584$, $c = 1.4871$, $d = 0.5053$, $r = 0.7466$, and $q = 5.1297$.

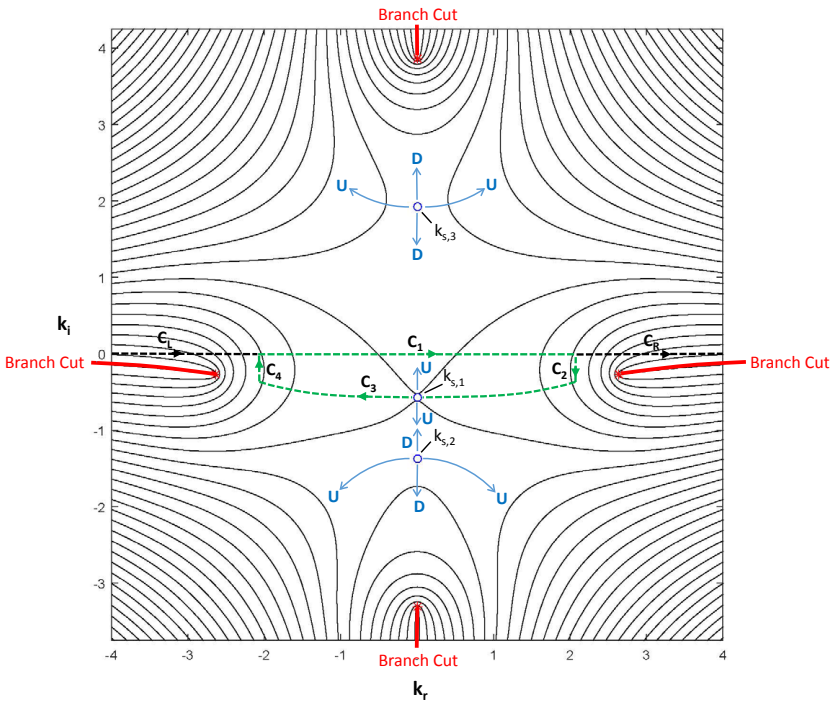

Figure A.5: Contours of constant Real$[\phi_1(k)]$ vs complex $k = k_r + ik_i$ at neutral stability ($Re = 0.05\cot\theta$) for $x/t = 2$, $\theta = \pi/4$, and $We = 0.1$. Notation is the same as in Figure A.1. The orientation of the saddles enables a closed contour (indicated by dashed lines) to be drawn through $k_{s,1}$ that includes a portion of the real axis, $\mathbf{C}_1$, and also has Real$[\phi_1(k_{s,1})]$ as a maximum along the contour — thus, the method of steepest decent may be used to determine the long time asymptotic behavior of the integral involving $\phi_1(k)$ in (II.15c) along the contour $\mathbf{C}_1$. Alternatively, the orientation of saddles $k_{s,2}$ and $k_{s,3}$ makes them spurious and are not accessible by connection to any real contour. The path of integration in (II.15c) is the infinite k_r-axis, i.e. consists of the contour $\mathbf{C}$=$\mathbf{C}_\mathrm{L}\cup\mathbf{C}_1\cup\mathbf{C}_\mathrm{R}$ and evaluated in the same manner as discussed in Figure A.3. For reference, the location of the contributing saddle, and related quantities necessary to determine the asymptotic behavior using (A.13), (A.14), and (A.24h) are as follows: $a = 0$, $b = 1.3728$, $c = 0$, $d = 2.8420$, $r = 1.8563$, and $q = 0$.

Appendix B

Appendix: On the response of neutrally stable flows to oscillatory forcing with application to liquid sheets

B.1. Appendix: Fourier Series Solution (FSS) to (III.8)

B.1.1 Form of the FSS

In order to validate the asymptotic analysis employed in Appendix B.2, the solution to (III.8) over the infinite domain $x \in (-\infty, \infty)$ is approximated with a Fourier series solution (FSS) over a finite domain of $x \in [-L, L]$ with periodic boundary conditions $h(-L, t) = h(L, t)$

as done by Barlow et al. [21]. The finite length L is taken to be sufficiently large so that the response is unaffected by an increase in L during the simulation time. The FSS is given by

$$h_F(x,t) = \sum_{n=-N}^{N} \left(\left(F_{1_n} e^{r_{1_n} t} + F_{2_n} e^{r_{2_n} t} + F_{3_n} e^{i\omega_f t} \right) e^{ik_n x} \right), \tag{B.1a}$$

where

$$x \in [-L, L], \qquad k_n = \frac{n\pi}{L}, \tag{B.1b}$$

$$F_{1_n} = \frac{h_0}{2L} - F_{2_n} - F_{3_n}, \quad F_{2_n} = \frac{\frac{u_0}{2L} - r_{1_n}\frac{h_0}{2L} + (r_{1_n} - i\omega_f)F_{3_n}}{(r_{2_n} - r_{1_n})}, \tag{B.1c}$$

$$F_{3_n} = \frac{\frac{A_f}{2L}}{(i\omega_f)^2 + \alpha_n(i\omega_f) + \beta_n}, \tag{B.1d}$$

$$r_{1_n} = -i(ck_n - Bk_n^2), \qquad r_{2_n} = -i(ck_n + Bk_n^2), \tag{B.1e}$$

$$\alpha_n = (2ick_n), \qquad \beta_n = (ick_n)^2 + B^2(k_n)^4. \tag{B.1f}$$

Notably,

$$h(x,t) = \lim_{N\to\infty} \left(\lim_{L\to\infty} \left(h_F(x,t) \right) \right) \tag{B.2}$$

B.1.2 Spatial resolution of solutions

A key issue with the implementation of the long-time asymptotic solutions given in equations (III.15) and (III.17) is the resolution of high frequency sinusoids. An important distinction to make first is that the spatial resolution discussed here is entirely separate from how many terms are included in the FSS. Spatial resolution here refers to how many data points are sampled over a given V domain. While the values of the step size in V could be tested manually, it is possible to approximate the required step size by looking at the asymptotic solutions.

To explore this issue, we first suppose that the phase of the highest frequency (in V) exponential from the long-time asymptotic solution, denoted generally as f, has some associated frequency which is a function of time, $\omega_A(t)$, and some phase shift which may be a function of time, $\phi(t)$, such that,

$$f = e^{i(\omega_A(t)V + \phi(t))}. \tag{B.3}$$

As an example, for region C in Figure III.9, $\omega_A(t) = k_2 t$ and $\phi(t) = i\omega_f t$ (extracted from the exponent in (III.15e)). For a fixed time, it follows that the mode given in (B.3) has a wavelength of $2\pi/\omega_A(t)$ in V. We may then choose the number of points in our numerical solution such that the maximum value for the step size in V is, for example,

$$\Delta V = \frac{\pi}{10\omega_A(t)}. \tag{B.4}$$

As an example, the ΔV needed to achieve this level of resolution for region C in Figure III.9 would be

$$\Delta V_{(\omega_f < \omega_c,\ \text{Region } C)} = \frac{\pi}{10k_2 t} = \left(\frac{B\pi}{5\left(c - \sqrt{c^2 + 4B\omega_f}\right)} \right) \frac{1}{t}. \tag{B.5}$$

Note that, as we look at longer and longer times, a smaller step size in V is required to achieve the same resolution relative to the wave pattern. This is especially problematic as $t \to \infty$ because $\Delta V \to 0$. As long as the same velocity points are sampled, however, the FSS (Appendix B.1.1) and the asymptotic solutions can be compared. However, if ΔV is too large, the aliasing solution will obscure the structure.

B.2. Appendix: Fourier Integral solution to (III.8)

The solution to the system (III.8) is found by taking its Fourier transform, solving the resulting ordinary differential equation in the time domain through a Laplace transform, and then using the Fourier inversion integral to obtain

$$\begin{aligned} h(x,t) = -\frac{A_f}{2\pi B^2}\int_{-\infty}^{\infty}\left(\frac{\cos(Bk^2t)e^{ik(V-c)t}}{(k-k_0)(k-k_1)(k-k_2)(k-k_3)}\right)dk \\ -\frac{iA_fc}{2\pi B^3}\int_{-\infty}^{\infty}\left(\frac{\sin(Bk^2t)e^{ik(V-c)t}}{k(k-k_0)(k-k_1)(k-k_2)(k-k_3)}\right)dk \\ -\frac{iA_f\omega_F}{2\pi B^3}\int_{-\infty}^{\infty}\left(\frac{\sin(Bk^2t)e^{ik(V-c)t}}{k^2(k-k_0)(k-k_1)(k-k_2)(k-k_3)}\right)dk \\ +\frac{A_f}{2\pi B^2}\int_{-\infty}^{\infty}\left(\frac{e^{i(kV+\omega_f)t}}{(k-k_0)(k-k_1)(k-k_2)(k-k_3)}\right)dk. \end{aligned} \tag{B.6}$$

The definitions of k_0 through k_3 are given in equation (III.9d) and are written here for completeness:

$$\begin{aligned} k_0 &= \frac{-c-\sqrt{c^2-4B\omega_f}}{2B}, \qquad k_1 = \frac{-c+\sqrt{c^2-4B\omega_f}}{2B}, \\ k_2 &= \frac{c-\sqrt{c^2+4B\omega_f}}{2B}, \qquad k_3 = \frac{c+\sqrt{c^2+4B\omega_f}}{2B}. \end{aligned} \tag{B.7}$$

The four integrals in (B.6) are combined into two new integrals, $\tilde{I}$ and $\hat{I}$, which are equations (III.9b) and (III.9c) in the main text.

B.2.1 Evaluation of $\tilde{I}$

In order to evaluate (III.9b) it is broken into $\tilde{I}_1$ and $\tilde{I}_2$ such that

$$\tilde{I} = \tilde{I}_1 + \tilde{I}_2, \tag{B.8a}$$

$$\tilde{I}_1 = \int_{-\infty}^{\infty} -\frac{A_f e^{i(\omega_f)t}}{B^2} \frac{e^{i(kV)t} e^{iB(k-k_2)(k-k_3)t}}{(k-k_0)(k-k_1)(k-k_2)(k-k_3)} dk, \tag{B.8b}$$

$$\tilde{I}_2 = \int_{-\infty}^{\infty} \frac{A_f e^{i(\omega_f)t}}{B^2} \frac{e^{i(kV)t}}{(k-k_0)(k-k_1)(k-k_2)(k-k_3)} dk. \tag{B.8c}$$

Equation (B.8b) is evaluated with a "bow-tie" contour[1] centered on

$$k_s = \frac{(c-V)}{2B}, \tag{B.9}$$

which extends into the first and third quadrants; Supplemental Material Section B.7 provides the methodology and Figure B.2 (provided in Section B.7) shows the "bow-tie" contour shape. Equation (B.8c) is evaluated with a half-plane contour in either the upper or lower half-plane, depending on the sign of V (see Supplemental Material Section B.8).

Solutions for $\tilde{I}_1$ and $\tilde{I}_2$ are summarized below (from Supplemental Material Sections B.7 and B.8)

$$\begin{aligned}\tilde{I}_1 \sim \frac{-A_f e^{i\omega_f t}}{B^2} \Bigg[&\left(\left(P_A(k_0;k_s) - P_B(k_0;k_s) + \right) F(k_0) \right) + \left(\left(P_A(k_1;k_s) - P_B(k_1;k_s) \right) F(k_1) \right) \\ &+ \left(\left(P_A(k_2;k_s) - P_B(k_2;k_s) \right) F(k_2) \right) + \left(\left(P_A(k_3;k_s) - P_B(k_3;k_s) \right) F(k_3) \right) \\ &+ \frac{2e^{\left(\frac{i\pi}{4}\right)} e^{-i\left(\frac{(V-c)^2}{4B} + \omega_f\right)t}}{(k_s-k_0)(k_s-k_1)(k_s-k_2)(k_s-k_3)} \sqrt{\frac{\pi}{4Bt}} \Bigg] \quad \text{as} \quad t \to \infty, \end{aligned} \tag{B.10a}$$

[1] The contour is so called because it is shaped like a bow-tie with two lobes extending out symmetrically from a central point.

$$k_s = \frac{c-V}{2B}, \quad F(k_j) = \lim_{k \to k_j} = \left[\frac{(k-k_j)e^{i(B(k-k_2)(k-k_3)+kV)t}}{(k-k_0)(k-k_1)(k-k_2)(k-k_3)} \right], \tag{B.10b}$$

$$P_L(k_j; k_s) = \begin{cases} 2i\pi & \text{if pole } k_j \text{ is enclosed by contour } L \\ i\pi & \text{if pole } k_j \text{ is intersected by contour } L \\ 0 & \text{if pole } k_j \text{ is not enclosed by contour } L \end{cases} . \tag{B.10c}$$

The notation in (B.10a) is defined in terms of the P_L function (B.10c) for two contours labeled A and B (so, $L = A$ or $L = B$ in (B.10)); see Figure B.2 of Section B.7 for a depiction of these contours. The function P_L accounts for if a given pole k_j is contained within a given contour L. By the convention used in this chapter, the contour A is said to be the portion of the bow-tie contour that extends to the right of the saddle point k_s and contour B is said to be the portion of the bow-tie contour that extends to the left of the k_s. (see Figure B.2 in Section B.7).

The solution for $\tilde{I}_2$ is given as

$$\tilde{I}_2\Big|_{V \geq 0} = \frac{i\pi A_f}{B^2} e^{i\omega_f t} \Big(2G(k_1) + G(k_2) + G(k_3) \Big), \tag{B.11a}$$

$$\tilde{I}_2\Big|_{V \leq 0} = \frac{i\pi A_f}{B^2} e^{i\omega_f t} \Big(-2G(k_0) - G(k_2) - G(k_3) \Big), \tag{B.11b}$$

$$G(z_j) = \lim_{k \to k_j} \left((k-k_j) \frac{e^{ikVt}}{(k-k_0)(k-k_1)(k-k_2)(k-k_3)} \right), \tag{B.11c}$$

where k_0 through k_3 are defined in (III.9d). Note that the evaluation of the two expressions for $\tilde{I}_2$ at $V = 0$ are equivalent. The form of (B.10a) does not assume the position of the poles, so it is general for any case where $\omega_f \neq \omega_c$.

B.2.2 Evaluation of $\hat{I}$

The integral (III.9c) is first differentiated with respect to t and broken up into four parts such that

$$\frac{d\hat{I}}{dt} = i\frac{A_f}{2B^2}\left((V-c)\left(\hat{I}_1+\hat{I}_2\right)+B\left(\hat{I}_3+\hat{I}_4\right)\right), \tag{B.12}$$

$$\hat{I}_1 = \int_{-\infty}^{\infty} \frac{e^{i(Bk^2+k(V-c))t}}{k(k-k_0)(k-k_1)}dk, \tag{B.13a}$$

$$\hat{I}_2 = \int_{-\infty}^{\infty} \frac{-e^{i(-Bk^2+k(V-c))t}}{k(k-k_0)(k-k_1)}dk, \tag{B.13b}$$

$$\hat{I}_3 = \int_{-\infty}^{\infty} \frac{e^{i(Bk^2+k(V-c))t}}{(k-k_0)(k-k_1)}dk, \tag{B.13c}$$

$$\hat{I}_4 = \int_{-\infty}^{\infty} \frac{e^{i(-Bk^2+k(V-c))t}}{(k-k_0)(k-k_1)}dk. \tag{B.13d}$$

The four sub-integrals in (B.13) are evaluated using bow-tie contours described in Figure B.2 of Section B.7. The contours for equations (B.13a) and (B.13c) are centered at

$$k_{s_1} = \frac{(c-V)}{2B} \tag{B.14}$$

and extend into the first and third quadrants. The contours for equations (B.13b) and (B.13d) are centered at

$$k_{s_2} = \frac{(V-c)}{2B} \tag{B.15}$$

and extend into the second and fourth quadrants.

Once the contours are evaluated (again, see Supplemental Material Section B.7), the results

are combined to yield

$$\begin{aligned}\frac{d\hat{I}}{dt} \sim \frac{iA_f}{2B^2}\int_{\psi}^{t}\Bigg[& \\ & \left[\frac{P_A(k_0;k_{s_1})-P_B(k_0;k_{s_1})}{(k_0-k_1)}\right]\left(B+\frac{(V-c)}{k0}\right)\left(e^{i(Bk_0^2+k_0(V-c))t}\right) \\ & +\left[\frac{P_A(k_1;k_{s_1})-P_B(k_2;k_{s_1})}{(k_1-k_0)}\right]\left(B+\frac{(V-c)}{k1}\right)\left(e^{i(Bk_1^2+k_1(V-c))t}\right) \\ & -\frac{e^{i\frac{\pi}{4}}\sqrt{\pi B}}{(k_{s_1}-k_0)(k_{s_1}-k_1)}\left(\frac{e^{ik_{s_1}t(V-c)}}{\sqrt{t}}\right)-\frac{e^{-i\frac{\pi}{4}}\sqrt{\pi B}}{(k_{s_2}-k_0)(k_{s_2}-k_1)}\left(\frac{e^{ik_{s_2}t(V-c)}}{\sqrt{t}}\right) \\ & +\left[\frac{P_A(k_0;k_{s_2})-P_B(k_0;k_{s_2})}{(k_0-k_1)}\right]\left(-B+\frac{(V-c)}{k0}\right)\left(e^{i(-Bk_0^2+k_0(V-c))t}\right) \\ & +\left[\frac{P_A(k_1;k_{s_2})-P_B(k_1;k_{s_2})}{(k_1-k_01)}\right]\left(-B+\frac{(V-c)}{k1}\right)\left(e^{i(-Bk_1^2+k_1(V-c))t}\right) \\ & +\left(P_A(0;k_{s_1})-P_B(0;k_{s_1})\right)\left(P_A(0;k_{s_2})-P_B(0;k_{s_2})\right)\frac{(V-c)}{(k_0)(k_1)}\Bigg]dt+\mathcal{C}, \quad \text{(B.16a)}\end{aligned}$$

$$\psi=\begin{cases}\infty & \text{if } V\neq c \\ & \\ 0 & \text{if } V=c\end{cases}, \quad \text{(B.16b)}$$

The notation in (B.16a) is defined in terms of the same P_L function (B.17b) as is used in (B.10). The function P_L accounts for if a given pole k_j is contained within a given contour L. By the convention used in this chapter, the contour A is said to be the portion of the bow-tie contour that extends to the right of the saddle point k_s and contour B is said to be the contour portion of the bow-tie that extends to the left of the k_s (see Figure B.2 in Section B.7). Importantly, the P_L functions have no dependence on t, and they can be treated as constants for the purposes of integration. The lower limit of integration ψ (B.16b) is chosen such that the integration constant C evaluates to zero which is consistent with

the FSS (Appendix B.1.1) at long times. By integrating the first terms, we obtain

$$\hat{I} \sim \frac{A_f}{2B^2}\Bigg[- \Big(P_A(k_0;k_{s_1}) - P_B(k_0;k_{s_1})\Big]\left(\frac{e^{i\left(Bk_0^2+k_0(V-c)\right)t}}{k_0^2(k_1-k_0)}\right) + \left(P_A(k_1;k_{s_1}) - P_B(k_1;k_{s_1})\right)\left(\frac{e^{i\left(Bk_1^2+k_1(V-c)\right)t}}{k_1^2(k_1-k_0)}\right) - \left(P_A(k_0;k_{s_2}) - P_B(k_0;k_{s_2})\right)\left(\frac{e^{i\left(-Bk_0^2+k_0(V-c)\right)t}}{k_0^2(k_1-k_0)}\right) + \left(P_A(k_1;k_{s_2}) - P_B(k_1;k_{s_2})\right)\left(\frac{e^{i\left(-Bk_1^2+k_1(V-c)\right)t}}{k_1^2(k_1-k_0)}\right) + \frac{-ie^{i\frac{\pi}{4}}\sqrt{B\pi}}{(k_{s_1}-k_0)(k_{s_1}-k_1)}\int_{\infty}^{t}\left(\frac{e^{i\frac{k_{s_1}(V-c)}{2}\eta}}{\sqrt{\eta}}\right)d\eta + \frac{-ie^{-i\frac{\pi}{4}}\sqrt{B\pi}}{(k_{s_1}+k_0)(k_{s_1}+k_1)}\int_{\infty}^{t}\left(\frac{e^{-i\frac{k_{s_1}(V-c)}{2}\eta}}{\sqrt{\eta}}\right)d\eta + \mathcal{C}\Bigg] \quad \text{as} \quad t\to\infty, \tag{B.17a}$$

$$P_L(k_j;k_{s_m}) = \begin{cases} 2i\pi & \text{if pole } k_j \text{ is enclosed by contour } L \text{ for } \hat{I}_m \\ i\pi & \text{if pole } k_j \text{ is intersected by contour } L \\ 0 & \text{if pole } k_j \text{ is not enclosed by contour } L \end{cases}, \tag{B.17b}$$

where ψ defined in (B.16b), and the solution to the remaining integrals is given in (B.17).

B.3. Appendix: Asymptotic solution to (III.8) for $\omega_f < \omega_c$

This section develops the long-time asymptotic solution for equation (III.8) for the pole structure in Figure III.3. The long-time solution for the $\omega_f < \omega_c$ case is found by applying

the pole structure to the solutions for $\tilde{I}$ (see Appendix B.2.1) and $\hat{I}$ (see Appendix B.2.2). Evaluating (B.10), (B.11) and (B.17) yields

$$Real[h(x,t)_{\omega_f<\omega_c}] \sim Real[\frac{A_f e^{i\omega_f t}}{B^2}(T_1+T_2+T_3) - iA_f\delta_j\sqrt{t}]$$

$$\text{as } t\to\infty, \quad \delta_j = \begin{cases} 1, & V=c \\ 0, & V\neq c \end{cases}, \tag{B.18}$$

where T_1, T_2, and T_3 are defined as follows

$$T_1 \sim -\Bigg[\Big(P(k_0,k_{s_1})F(k_0)\Big)+\Big(P(k_1,k_{s_1})F(k_1)\Big)+\Big(P(k_2,k_{s_1})F(k_2)\Big) + \Big(P(k_3,k_{s_1})F(k_3)\Big)+\frac{2e^{\left(\frac{i\pi}{4}\right)}e^{-i\left(\frac{(V-c)^2}{4B}+\omega_f\right)t}}{(k_{s_1}-k_0)(k_{s_1}-k_1)(k_{s_1}-k_2)(k_{s_1}-k_3)}\sqrt{\frac{\pi}{4Bt}}\Bigg] \quad \text{as} \quad t\to\infty, \tag{B.19a}$$

$$F(k_j) = \lim_{k\to k_j} = \left[\frac{(k-k_j)e^{i(B(k-k_2)(k-k_3)+kV)t}}{(k-k_0)(k-k_1)(k-k_2)(k-k_3)}\right], \tag{B.19b}$$

$$T_2 = \text{sgn}(V)i\pi\Big(G(k_0)+G(k_1)+G(k_2)+G(k_3)\Big), \tag{B.20a}$$

$$G(z_j) = \lim_{k\to k_j}\left((k-k_j)\frac{e^{ikVt}}{(k-k_0)(k-k_1)(k-k_2)(k-k_3)}\right), \tag{B.20b}$$

$$T_3 \sim \frac{1}{2}\Bigg[-P(k_0,k_{s_1})\left(\frac{e^{i\left(Bk_0^2+k_0(V-c)\right)t}}{k_0^2(k_1-k_0)}\right)+P(k_1,k_{s_1})\left(\frac{e^{i\left(Bk_1^2+k_1(V-c)\right)t}}{k_1^2(k_1-k_0)}\right) + P(k_0,k_{s_2})\left(\frac{e^{i\left(-Bk_0^2+k_0(V-c)\right)t}}{k_0^2(k_1-k_0)}\right)-P(k_1,k_{s_2})\left(\frac{e^{i\left(-Bk_1^2+k_1(V-c)\right)t}}{k_1^2(k_1-k_0)}\right) + \frac{-ie^{i\frac{\pi}{4}}\sqrt{B\pi}}{(k_{s_1}-k_0)(k_{s_1}-k_1)}\int_\infty^t\left(\frac{e^{i\frac{k_{s_1}(V-c)}{2}\eta}}{\sqrt{\eta}}\right)d\eta + \frac{-ie^{-i\frac{\pi}{4}}\sqrt{B\pi}}{(k_{s_1}+k_0)(k_{s_1}+k_1)}\int_\infty^t\left(\frac{e^{-i\frac{k_{s_1}(V-c)}{2}\eta}}{\sqrt{\eta}}\right)d\eta+\mathcal{C}\Bigg]$$

$$\text{as} \quad t\to\infty \quad \text{and} \quad V\neq c, \tag{B.21}$$

$$k_{s_1} = \frac{(c-V)}{2B}, \quad k_{s_2} = \frac{(V-c)}{2B}, \tag{B.22}$$

$$P(k_j, k_{s_L}) = \begin{cases} i\pi & \text{if } k_{s_L} < k_j \\ \text{undefined} & \text{if } k_{s_L} = k_j \\ -i\pi, & \text{if } k_{s_L} > k_j \end{cases}. \tag{B.23}$$

In equation (B.21) $\mathcal{C}$ is an unknown constant of integration. The limits of the integrals were chosen for $V \neq c$ such that $\mathcal{C}$ evaluates to zero as motivated by comparison with the FSS (Appendix B.1.1). The integrals can be evaluated by defining $\zeta \equiv {}^{(V-c)^2}/_{4B}$, $E_1 \equiv -1$, $E_2 \equiv 1$ and evaluating the new integral through the asymptotic expansion of the Fresnel integral as

$$\int_{\infty}^{t} \left(\frac{e^{E_j \zeta \eta}}{\sqrt{\eta}} \right) d\eta = \int_{0}^{t} \left(\frac{e^{E_j \zeta \eta}}{\sqrt{\eta}} \right) d\eta - \int_{0}^{\infty} \left(\frac{e^{E_j \zeta \eta}}{\sqrt{\eta}} \right) d\eta \sim$$
$$\sqrt{\frac{2\pi}{\zeta}} \left[\left(\frac{1}{2} + \frac{\sin(\zeta t)}{\sqrt{2\pi\zeta t}} \right) + iE_j \left(\frac{1}{2} - \frac{\cos(\zeta t)}{\sqrt{2\pi\zeta t}} \right) \right] - (1 + iE_j) \sqrt{\frac{\pi}{2\zeta}}$$
$$\text{as} \qquad t \to \infty \qquad \text{and} \qquad V \neq c. \tag{B.24}$$

For the case of equation (B.21) when $V = c$, the limits of integration must be chosen to be $0 \to t$ instead of $\infty \to t$ to ensure a bounded integral, leaving the evaluation of each integral as

$$\int_{0}^{t} \frac{1}{\sqrt{\eta}} d\eta = 2\sqrt{t} + \mathcal{C}_1, \tag{B.25}$$

where $\mathcal{C}_1$ evaluates to zero compared to the FSS (Appendix B.1.1). The emergent algebraic growth only arises in the imaginary part of T_3 (B.21); as such, if A_f is chosen to be purely real, the growth only occurs in the imaginary part of $h(x,t)$ and is not observable in a physical solution.

B.4. Appendix: Asymptotic solution to (III.8) for $\omega_f > \omega_c$

This section develops the long-time asymptotic solution for equation (III.8) for the pole structure in Figure III.4. The long-time solution for the $\omega_f > \omega_c$ case is found by applying the pole structure to the solutions for $\tilde{I}$ (see Appendix B.2.1) and $\hat{I}$ (see Appendix B.2.2). Evaluating (B.10), (B.11) and (B.17) yields

$$h(x,t)_{\omega_f>\omega_c} \sim \left(\frac{A_f e^{i\omega_f t}}{B^2}\left(T_1+T_2\right)\right) - iA_f\delta_j\sqrt{t} \quad \text{as } t\to\infty, \quad \delta_j = \begin{cases} 1, & V=c \\ 0, & V\neq c \end{cases}. \tag{B.26}$$

Note that, in equation (B.26), the growing term is purely imaginary when A_f is taken to be real and even then only occurs along the $V = c$ velocity.

$$T_1 \sim -\left[P(k_2,k_s)F(k_2) + P(k_3,k_s)F(k_3)\right] \qquad \text{as} \qquad t\to\infty, \tag{B.27a}$$

$$F(k_j) = \lim_{k\to k_j} = \left[\frac{(k-k_j)e^{i(B(k-k_2)(k-k_3)+kV)t}}{(k-k_0)(k-k_1)(k-k_2)(k-k_3)}\right], \tag{B.27b}$$

$$T_2 \sim \mathrm{sgn}(V)i\pi\Big(G(k_2)+G(k_3)\Big) \qquad \text{as} \qquad t\to\infty, \tag{B.28a}$$

$$G(k_j) = \lim_{k\to k_j}\left((k-k_j)\frac{e^{ikVt}}{(k-k_0)(k-k_1)(k-k_2)(k-k_3)}\right). \tag{B.28b}$$

The definitions of k_{s_1} and $P(k_j,k_s)$ are given above in equations (B.22) and (B.23), and the poles k_0 through k_3 are defined in (III.9d). As with the $\omega_f < \omega_c$ case, the algebraic growth only occurs in the real part of h if A_f is imaginary or complex.

B.5. Appendix: Justification for bounding amplitude expressions given in Section B.5

For a given set of parameters, the solution is arranged into the form of (III.12 (including the terms which are purely imaginary, for completeness),

$$Real[h(x,t)] \sim Real\left[\sum_{n=1}^{N}\left(\alpha_n e^{i\beta_n(V)t}\right) + o(1) + (\text{Imaginary term})\right]$$
$$V \in [V_1, V_2] \quad as \quad t \to \infty, \quad \text{(B.29)}$$

for N different modes where α_n is complex and $\beta_n(V)$ is real, such the that argument of the exponential above is purely imaginary. Only imaginary exponents are considered because real exponents either lead to terms that damp with time (subdominant to oscillations) or terms that grow with time (swamp out any oscillations) as time goes to infinity. The terms are grouped in such a way that $\beta_i \neq \beta_j$, as the amplitude of two in-phase exponentials is merely the sum of the amplitudes. To handle the out of phase terms, we first write

$$\alpha_n \equiv A_n e^{(i\phi)} \quad \text{such that} \quad A_n = \left|\alpha_n\right| \tag{B.30}$$

where A_n is real and positive and ϕ is real. Equation (B.29) then becomes

$$Real[h(x,t)] \sim Real\left[\sum_{n=1}^{N}\left(A_n e^{(i\beta_n t + i\phi)}\right)\right] \qquad V \in [V_1, V_2] \qquad \text{as} \qquad t \to \infty. \tag{B.31}$$

In the summation, each term is a complex number with a fixed modulus and changing argument. Through the triangle inequality, the result of the summation is less than or asymptotic to (denoted by $\lesssim$) the sum of A_n:

$$\left|Real[h(x,t)]\right| \lesssim \sum_{n=1}^{N}(A_n) \qquad V \in [V_1, V_2] \qquad \text{as} \qquad t \to \infty. \tag{B.32}$$

From (B.30),

$$\left|Real[h(x,t)]\right| \lesssim \sum_{n=1}^{N} \left|\alpha_n\right| \qquad V \in [V_1, V_2] \qquad \text{as} \qquad t \to \infty. \tag{B.33}$$

Equation (B.33) is used directly to find the bounding amplitudes presented in Section III.3.2.

B.6. Appendix: Exploration of the relative amplitudes in Figures III.9 and III.17

The amplitudes of each region shown in Figures III.9 and III.17 were examined to determine the generality of the indicated figures qualitatively. In some cases, inspection of the asymptotic results (see (III.15a and III.15b) was all that was needed to establish relationships between the region amplitudes. In some, the bounding amplitudes were calculated to firmly establish the relationship between amplitudes (labeled as "Tested" below). In these cases, the following parameter ranges were explored:

$$A_f, B, c \quad \in (0, 10000), \quad \omega_f = W\omega_c, \tag{B.34}$$

where $W \in (0,1)$ for the $\omega_f < \omega_c$ case and $W \in (1, 10000)$ for the $\omega_f > \omega_c$ case. The results are as follows:

- For the $\omega_f < \omega_c$ case in Figure III.9, the following general conclusions are drawn. The bounding amplitude of:
  - region A is smaller than that of region B (By inspection of (III.15a and III.15b))
  - region B is smaller than that of region B_2 (By inspection of (III.15b and III.15c))

  - region B_2 is smaller than that of region C_2 (Tested)
  - region C_2 is larger than that of region C (By inspection of (III.15d and III.15e))
  - region C is larger than that of region D (By inspection of (III.15e and III.15f))
  - region B is smaller than that of region C (Tested)

- For the $\omega_c > \omega_f$ case in Figure III.17, the following general conclusions are drawn. The bounding amplitude of:
  - region A is smaller than that of region B (By inspection of (III.17a and III.17b))
  - region B is smaller than that of region C (Tested)
  - region C is larger than that of region D (By inspection of (III.17c and III.17d))

The amplitude of the *Asymptotically Undisturbed Regions* (regions A and D in Figures III.9 and III.17) is zero, so the long-time amplitude of those regions will always be less than or equal to any other region. Also through inspection, the amplitudes of the *Additional Forced Regions* (regions B_2 and C_2 in Figure III.9) are equal to the amplitudes of the respective *Forced Regions* (regions B and C in Figure III.9) plus some positive number. From this investigation, we conclude that the relative amplitudes of the regions shown in Figures III.9 and III.17 are sufficiently representative of all solutions to (III.8).

B.7. Supplemental: Evaluating a bow-tie contour

We now examine the contour integral and evaluation of Equation (B.8b), that is representative of the other contour integrals used in this paper. To begin, we rewrite (B.8b) in terms

of Φ as,

$$\tilde{I}_1 = -\frac{A_f}{B^2} \int_{-\infty}^{\infty} \left[\left(e^{i\Phi t} \right) \right] \Big/ \left[(k-k_0)(k-k_1)(k-k_2)(k-k_3) \right] dk, \tag{B.35}$$

where

$$\Phi = Bk^2 - ck - \omega_f + kV. \tag{B.36}$$

By substituting in the definition of k_2 and k_3 and differentiating Φ with respect to k, we find that there is a second order saddle point at

$$k_s = \frac{(c-V)}{2B},$$

as stated in (B.9). A preliminary contour is established in the complex k plane as shown in Figure B.1. The limits on the angles γ_1 and γ_2 are chosen such that the contour integrals along the curved sections go to zero and the dotted line path corresponds to that of the integral (B.8b) as $R \to \infty$.

Through consideration of (B.35), the contour angles, γ_1 and γ_2, are restricted to lie in the intervals $[0, \pi/2]$ and $[\pi, 3\pi/2]$, as indicated in Figure B.1. When the contour angles are chosen to be $\pi/4$ and $\frac{5\pi}{4}$, the integrals along the diagonal can be evaluated asymptotically as time goes to infinity using the method of steepest descent (see Figure B.2).

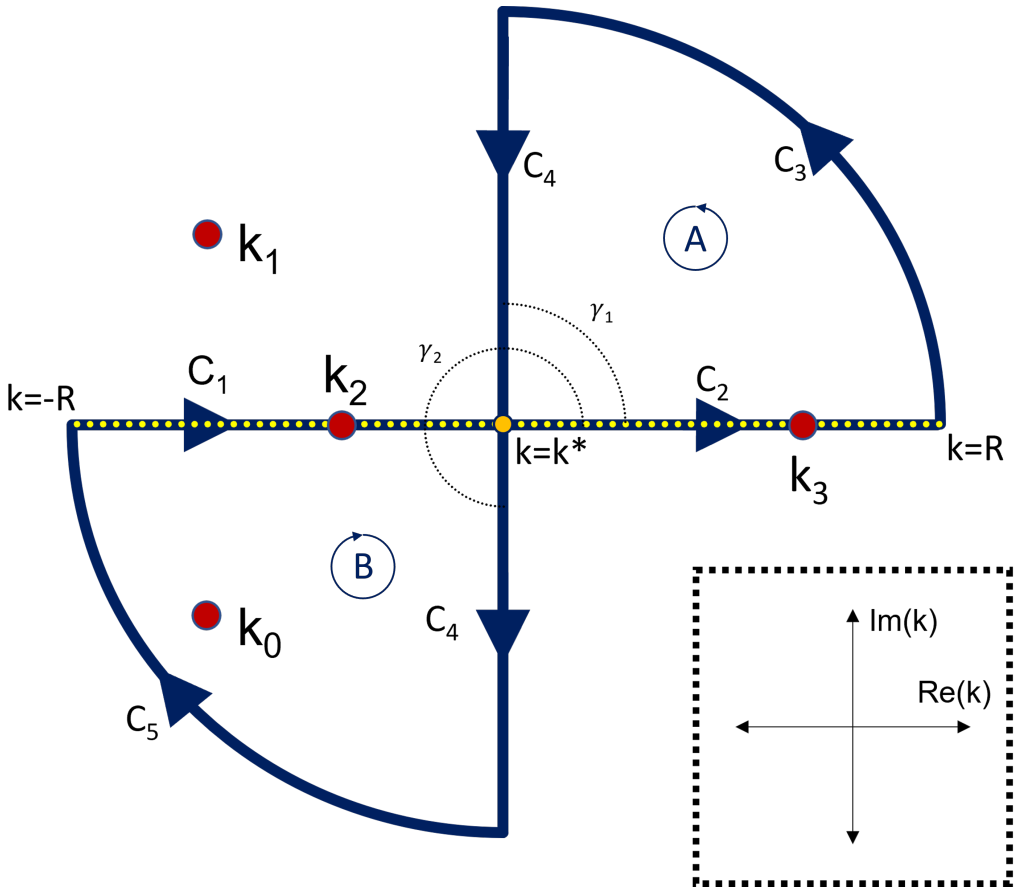

Figure B.1: General form of a bow-tie contour. For some central point k^*, the angles γ are limited to $(0,\ \pi/2)$ for γ_1 and to $(\pi,\ 3\pi/2)$ for γ_2, so that the integrals along the curved sections, C_3 and C_5 go to zero as R goes to infinity. In this example, the pole k_0 is contained within a contour, and the pole k_1 is not. The integral along the real axis, the dotted yellow line, is the integral I_1 as R goes to infinity. The inset figure shows the orientation of the contour in the complex k plane. Depending on the value of k^*, the origin lies somewhere along the dotted yellow line. For the sake of demonstration, the $\omega_f > \omega_f$ case is presented here using the pole structure in Figure III.4. In the case of $\omega_f < \omega_c$, all the poles would lie on the dotted yellow line. Each lobe of the bow-tie is a closed subcontour where $A = C_2 \cup C_3 \cup C_4$ (from $i\infty$ to k^*) and $B = C_5 \cup C_1 \cup C_4$ (from k^* to $-i\infty$).

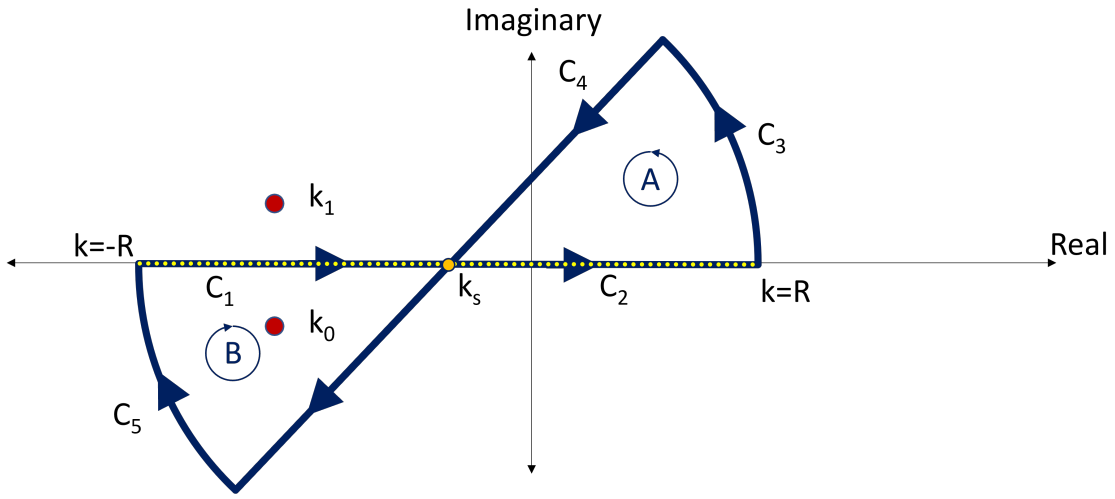

Figure B.2: An example bow-tie contour in the complex k plane. As R goes to infinity, contour sections C_1 and C_2 become the integral of interest, and contour sections C_3 and C_5 go to zero. The pole k_0 is enclosed, and the pole k_1 is not enclosed. The integral along the contour C_4 can be evaluated asymptotically as time goes to infinity due to the choice of k^* (Figure B.1) as the saddle point k_s and the choice of the angles γ. The position of the saddle point k_s is a function of velocity. Contour is depicted for $V > c$ and $\omega_f > \omega_c$. Varying V translates the contour along the real k axis. The inset figure shows the orientation of the contour in the complex k plane but does not represent where the origin is. Depending on the value of k^*, the origin lies somewhere along the dotted yellow line. For the sake of demonstration, the $\omega_f > \omega_f$ case is presented here relating to Figure III.4. In the case of $\omega_f < \omega_c$, all the poles would lie on the dotted yellow line. Each lobe of the bow-tie is a closed subcontour where $A = C_2 \cup C_3 \cup C_4$ (from $(1+i)\infty$ to k^*) and $B = C_5 \cup C_1 \cup C_4$ (from k^* to $-(1+i)\infty$)

As indicated in (B.9), the saddle point is a function of V and is always real-valued. Thus, the contour in Figure B.2 will be shifted along the real axis for different velocities. In what follows, no distinction will be made between the locus of saddles and the real k axis as they are equivalent for this problem.

The complete contour in Figure B.2 is broken up into two closed sub-contours, A and B which are separately evaluated through Cauchy's residue theorem (see Figure (B.2). As an example, we focus here on contour B of Figure B.2, shown in Figure B.3. Because the real axis segment of Figure B.2 is the integral of interest from $k = -\infty$ to $k = \infty$ it follows that the real axis segment of Figure B.3 is the integrand of interest integrated from $k = -\infty$ to k_s.

Around the closed contour B in Figure B.3 the integral can be expressed with ζ as a placeholder of the integrand as

$$\int_{C_1} \zeta dk + \int_{C_2} \zeta dk + \int_{C_3} \zeta dk = 2\pi i \text{Res}(\zeta, k_0) + \pi i \text{Res}(\zeta, k_2), \tag{B.37}$$

where $\text{Res}(f, k_j)$ is the residue of the integrand ζ at the pole k_j. The contained pole k_0 has the full contribution, but the intersected pole k_2 only has half the contribution. Also, this expression is only valid when k_0 is contained (as it is in Figure B.3). For a larger velocity, the saddle point may be shifted far enough to the left such that k_0 is no longer contained. Through the choice of γ_2, the integral along C_3 goes to zero as $R \to \infty$. Therefore, we can say that

$$\int_{C_1} \zeta dk = 2\pi i \text{Res}(\zeta, k_0) + \pi i \text{Res}(\zeta, k_2) - \int_{C_2} \zeta dk. \tag{B.38}$$

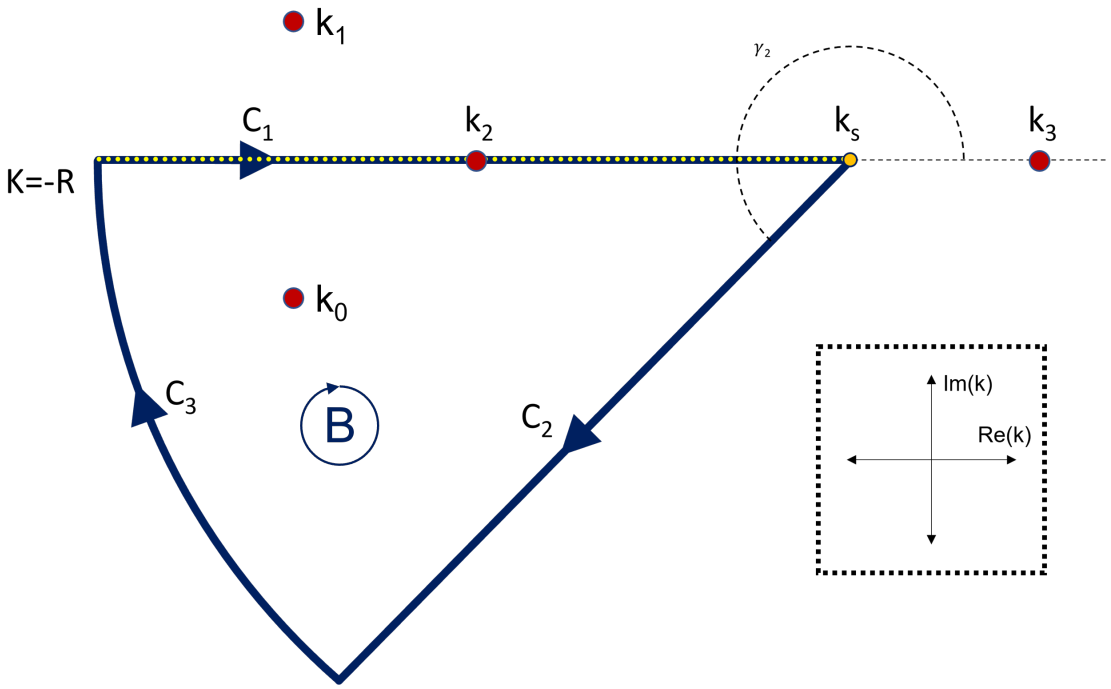

Figure B.3: Example integration contour B from Figure B.2. As before, the angle γ_2 is chosen such that the integral along C_3 goes to zero as R goes to infinity, the integral along C_2 can be determined asymptotically as time goes to infinity, and the integral along the real axis (C_1, dotted yellow line) is the integral of interest as R goes to infinity. For the sake of example, the pole k_0 is contained in the contour while the pole k_1 is not. Depending on the position of k_s, the poles k_2 and k_3 are either intersected by or separate from the contour.

Evaluating the residue of (B.35) at the saddle points yields

$$\mathrm{Res}(\zeta; k_j) = \lim_{k \to k_j} \left(-\frac{A_f}{B^2} \left(\frac{(k - k_j) e^{i\Phi t}}{(k - k_0)(k - k_1)(k - k_2)(k - k_3)} \right) \right). \tag{B.39}$$

The contour along the diagonal contour, C_2, is determined by converting the integral into

polar form as $k = k_s + re^{i\gamma}$, $dk = e^{i\gamma}dr$. This transformation yields

$$\int_{C_2} \zeta dk = \int_0^\infty e^{i\gamma}\zeta(k_s + re^{i\gamma})dr, \tag{B.40}$$

$$= e^{i\left(\gamma_2 - \left(\frac{(V-c)^2 t}{4B}\right) - \omega_f t\right)} \times \int_0^\infty \frac{e^{iBr^2 e^{2i\gamma}t}dr}{(re^{i\gamma_2} + k_s - k_0)(re^{i\gamma_2} + k_s - k_1)(re^{i\gamma_2} + k_s - k_2)(re^{i\gamma_2} + k_s - k_3)}. \tag{B.41}$$

Next, γ is chosen in order to get the exponent into the form of $-r^2$, $\gamma = \frac{5\pi}{4}$. The integral becomes:

$$\int_{C_2} \zeta dk = e^{\frac{5i\pi}{4}} e^{-i\left(\frac{(V-c)^2}{4B} + \omega_f\right)t} \int_0^\infty \frac{e^{-Br^2 t}dr}{(re^{i\frac{5\pi}{4}} + k_s - k_0)(re^{i\frac{5\pi}{4}} + k_s - k_1)(re^{i\frac{5\pi}{4}} + k_s - k_2)(re^{i\frac{5\pi}{4}} + k_s - k_3)}. \tag{B.42}$$

The integral in (B.42) can be split up into two separate integrals, one from $r = 0$ to $r = \epsilon$ and one from $r = \epsilon$ to $r = \infty$ where $\epsilon << 1$. Through integration by parts, the latter integral is asymptotically subdominant to the former. Over the small range 0 to ϵ the integral can be replaced with the integral linearized about $r = 0$. In order to evaluate the integral, ϵ is taken to infinity without adding any asymptotically dominant terms in accordance with the method of steepest descent. Doing so yields

$$\int_{C_2} \zeta dk \sim e^{\frac{5i\pi}{4}} e^{-i\left(\frac{(V-c)^2}{4B} + \omega_f\right)t} \int_0^\infty \frac{e^{-Br^2 t}dr}{(k_s - k_0)(k_s - k_1)(k_s - k_2)(k_s - k_3)} \quad \text{as} \quad t \to \infty, \tag{B.43}$$

$$\sim \frac{-e^{\frac{i\pi}{4}} e^{-i\left(\frac{(V-c)^2}{4B} + \omega_f\right)t}}{(k_s - k_0)(k_s - k_1)(k_s - k_2)(k_s - k_3)} \int_0^\infty e^{-Br^2 t}dr \quad \text{as} \quad t \to \infty, \tag{B.44}$$

$$\sim \frac{-e^{\frac{i\pi}{4}} e^{-i\left(\frac{(V-c)^2}{4B} + \omega_f\right)t}}{(k_s - k_0)(k_s - k_1)(k_s - k_2)(k_s - k_3)} \sqrt{\frac{\pi}{4Bt}} \quad \text{as} \quad t \to \infty. \tag{B.45}$$

For the arrangement of the poles and saddle point shown in Figure B.3, the section of interest can be expressed as

$$\int_{C_1} \zeta dk = 2\pi i \text{Res}(\zeta, k_0) + \pi i \text{Res}(\zeta, k_2) - \frac{-e^{\frac{i\pi}{4}} e^{-i\left(\frac{(V-c)^2}{4B} + \omega_f\right)t}}{(k_s - k_0)(k_s - k_1)(k_s - k_2)(k_s - k_3)} \sqrt{\frac{\pi}{4Bt}} \quad \text{as} \quad t \to \infty, \tag{B.46}$$

$$\text{Res}(\zeta; k_j) = \lim_{k \to k_j} \left(-\frac{A_f}{B^2} \left(\frac{(k - k_j) e^{i\Phi t}}{(k - k_0)(k - k_1)(k - k_2)(k - k_3)} \right) \right). \tag{B.47}$$

Note again that the pole structure and the velocity that is being studied will determine which of the residue terms contribute to the solution.

B.8. Supplemental: Evaluating a half-plane contour

Here we examine (B.8c), which we rewrite in terms of Φ as,

$$\tilde{I}_2 = \int_{-\infty}^{\infty} \left[\frac{A_f}{B^2} e^{i\Phi t} \right] \Big/ \left[(k - k_0)(k - k_1)(k - k_2)(k - k_3) \right] dk, \tag{B.48}$$

$$\Phi = \omega_f + kV. \tag{B.49}$$

Next we establish a half-plane contour in either the upper half-plane or lower-half plane depending on the sign of V.

The integral (B.8c) is expressed as

$$\begin{aligned} &\oint \left(\frac{A_f}{B^2} \frac{e^{i\Phi t}}{(k - k_0)(k - k_1)(k - k_2)(k - k_3)} dk \right) \\ &= \int_{C_1} \left(\frac{A_f}{B^2} \frac{e^{i\Phi t}}{(k - k_0)(k - k_1)(k - k_2)(k - k_3)} dk \right) + \int_{C_2} \left(\frac{A_f}{B^2} \frac{e^{i\Phi t}}{(k - k_0)(k - k_1)(k - k_2)(k - k_3)} dk \right) \\ &= 2\pi i \text{Res}(\zeta, k_1) + \pi i \text{Res}(\zeta, k_2) + \pi i \text{Res}(\zeta, k_3), \end{aligned} \tag{B.50}$$

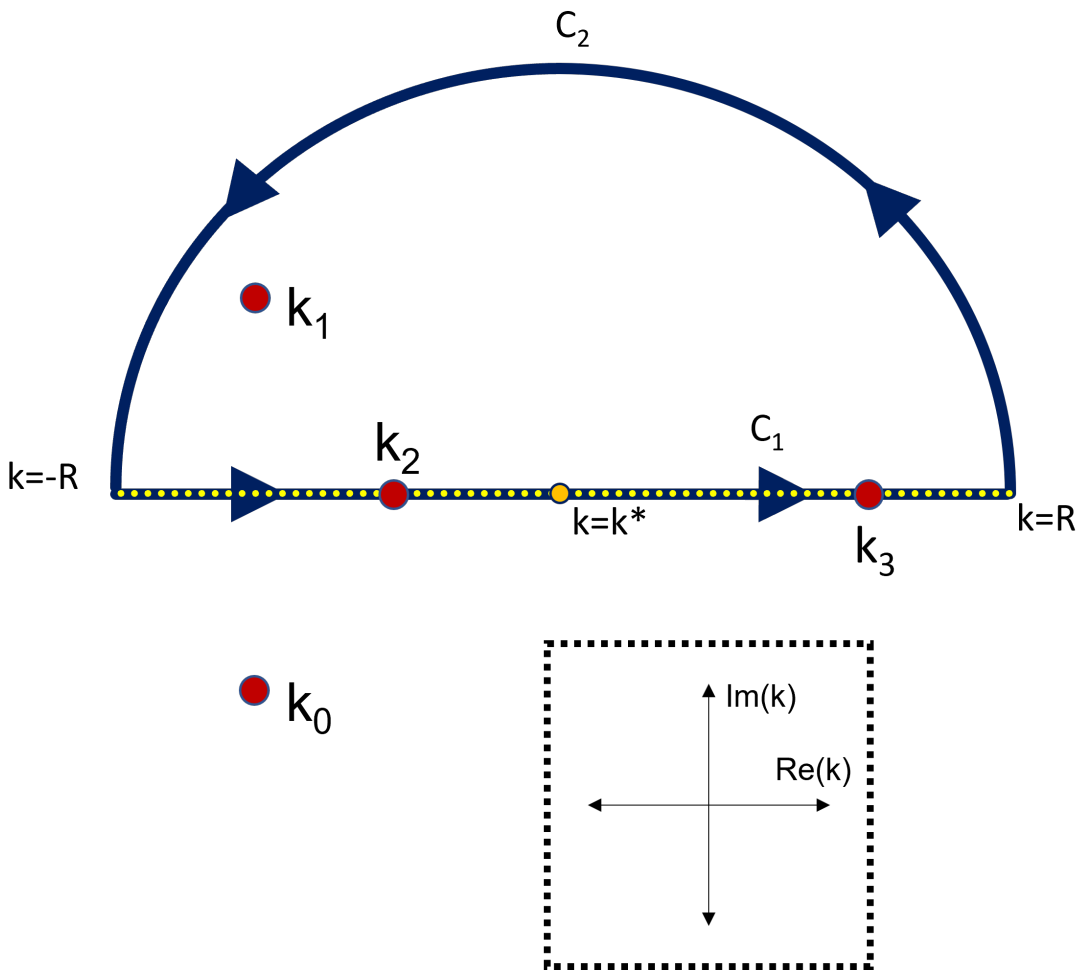

Figure B.4: Sample half-plane contour for (B.8c) for $V > 0$ and $\omega_f > \omega_c$. The poles k_1 is contained and the poles k_2 and k_3 are intersected. See (III.9d) for the definitions of the poles. The integral along the curved contour goes to zero as R goes to infinity.

where ζ is a placeholder for the integrand of (B.8c). We note that, because $V > 0$ and the contour is in the upper half-plane, the integral along C_2 goes to zero as R goes to infinity. Additionally, the integral along C_1 becomes $\tilde{I}_2$ under the same limit, yielding

$$\tilde{I}_2 = 2\pi i \text{Res}(\zeta, k_1) + \pi i \text{Res}(\zeta, k_2) + \pi i \text{Res}(\zeta, k_3), \tag{B.51}$$

$$\text{Res}(\zeta; k_j) = \lim_{k \to k_j} \left(-\frac{A_f}{B^2} \left(\frac{(k - k_j) e^{i(\omega_f + kV)t}}{(k - k_0)(k - k_1)(k - k_2)(k - k_3)} \right) \right). \tag{B.52}$$

Note that if $V < 0$ then the contour must be established in the lower half-plane, so k_0 would be contained instead of k_1. If $\omega_f < \omega_c$, all the poles lie on the real axis and the choice of direction for the contour has no effect on the solution. The result (B.51) is the desired exact result for $\tilde{I}_2$ used in the asymptotic results (B.18) and (B.26).

Appendix C

Appendix: On the two-dimensional extension of one-dimensional algebraically growing waves at neutral stability

C.1. Appendix: 2D-KRK: Analysis

C.1.1 Effect of initial conditions on solution response

Working from the 2D-KRK operator (IV.4) with the forcing amplitude set to zero, we obtain

$$\left(\frac{\partial^2 h}{\partial t^2}+2c_x\frac{\partial^2 h}{\partial t\partial x}+2c_z\frac{\partial^2 h}{\partial t\partial z}+c_x^2\frac{\partial^2 h}{\partial x^2}+2c_xc_z\frac{\partial^2 h}{\partial x\partial z}+c_z^2\frac{\partial^2 h}{\partial z^2}\right) + B^2\left(\frac{\partial^4 h}{\partial x^4}+2\frac{\partial^4 h}{\partial x^2\partial z^2}+\frac{\partial^4 h}{\partial z^4}\right)=0. \quad \text{(C.1)}$$

Instead of the homogeneous initial conditions in (IV.4c), we apply

$$h(x,z,0)=H_0\delta(x)\delta(z), \quad \frac{\partial h}{\partial t}(x,z,0)=U_0\delta(x)\delta(z), \quad \text{(C.2)}$$

where $h\to 0$ as $x,z\to\pm\infty$. Taking the Fourier transforms of (C.1) in the x and z directions, we obtain

$$\frac{d^2\hat{\hat{h}}_{xz}}{dt^2}+2ic_xk_x\frac{d\hat{\hat{h}}_{xz}}{dt}+2ic_zk_z\frac{d\hat{\hat{h}}_{xz}}{dt}-c_x^2k_x^2\hat{\hat{h}}_{xz}-2c_xc_zk_xk_z\hat{\hat{h}}_{xz}-c_z^2k_z^2\hat{\hat{h}}_{xz} + B^2k_x^4\hat{\hat{h}}_{xz}+2B^2k_x^2k_z^2\hat{\hat{h}}_{xz}+B^2k_z^4\hat{\hat{h}}_{xz}=0, \quad \text{(C.3)}$$

where

$$\hat{\hat{h}}_{xz}(0)=H_0, \quad \frac{d\hat{\hat{h}}_{xz}}{dt}(0)=U_0, \quad \text{(C.4)}$$

$$\psi=c_xk_x+c_zk_z, \quad \eta=B(k_x^2+k_z^2). \quad \text{(C.5)}$$

The solution to the 2nd order ordinary differential equation (C.3) subject to (C.4) is

$$\hat{\hat{h}}_{xz}=e^{-i\psi t}\left(\frac{U_0+(i\psi+i\eta)H_0}{\eta}\right)\left(\frac{e^{i\eta t}-e^{-i\eta t}}{2i}\right)+H_0e^{-i\psi t}e^{-i\eta t}. \quad \text{(C.6)}$$

The forced solution (IV.12a) is superimposed on (C.6) to obtain

$$\hat{\hat{h}}_{xz,Total}=e^{-i\psi t}\left(\frac{(A+U_0)+(i\psi+i\eta)H_0}{\eta}\right)\left(\frac{e^{i\eta t}-e^{-i\eta t}}{2i}\right)+H_0e^{-i\psi t}e^{-i\eta t}. \quad \text{(C.7)}$$

By inspection of (C.7), the effect of the forcing magnitude A and the initial surface velocity U_0 are equivalent. Therefore, U_0 can be taken to be zero without loss of response character.

To examine the effect of a initial surface height, the values of A and U_0 are set to zero in (C.7) and the inversion integrals are utilized to yield

$$h = H_0 \int_{-\infty}^{\infty}\int_{-\infty}^{\infty} \left(\left(\frac{\psi+\eta}{\eta}\right)\left(\frac{e^{i\eta t}-e^{-i\eta t}}{2}\right)+e^{-i\eta t}\right) e^{-i\psi t} e^{ik_x V_x t} e^{ik_z V_z t} dk_z dk_x,$$

$$\psi = c_x k_x + c_z k_z, \quad \eta = k_x^2 + k_z^2, \quad V_x = \frac{x}{t}, \quad V_z = \frac{z}{t}. \tag{C.8}$$

Through the steps included in Supplemental Material Section C.3.1, (C.8) is solved exactly to yield

$$h(x,z,t) = \frac{H_0}{4Bt\pi}\left(1 - 2\frac{c_x(V_x-c_x)+c_z(V_z-c_z)}{\hat{V}}\right)\sin\left(\frac{\hat{V}t}{4B}\right),$$

$$\hat{V} = \sqrt{(V_x-c_x)^2+(V_z-c_z)^2}. \tag{C.9}$$

Note that h is not localized — it exists at non-negligible amplitude at all values of $\hat{V}$ for any value of t. This violates the condition of $h \to 0$ as $x, z \to \infty$. This solution is admitted because the Fourier transform of the integral exists due to the rapid oscillations in the integrand.

C.1.2 Determination of $\mathcal{Q}$ and $\mathcal{W}$ in (IV.10) via contour integration

From (IV.10), the integrals $\mathcal{Q}$ and $\mathcal{W}$ may be expressed in terms of separate x and z integrals as

$$\mathcal{Q} = \mathcal{Q}_x \mathcal{Q}_z, \quad \mathcal{W} = \mathcal{W}_x \mathcal{W}_z. \tag{C.10}$$

In (C.10), the integral subscripts x and z correspond respectively to the integrated variables k_x and k_z in (IV.10); the definitions of $\mathcal{Q}_x$, $\mathcal{Q}_z$, $\mathcal{W}_x$, and $\mathcal{W}_z$ can thus be made by inspection of (IV.10). The analysis for $\mathcal{Q}_x$ is presented below; the analysis of the remaining sub-integrals closely follows that provided here, and are relegated to Supplemental Material

Section C.3.4. To begin, we write

$$\mathcal{Q}_x = \int_{-\infty}^{\infty} e^{i(\Phi(k_x))t} dk_x, \tag{C.11}$$

where Φ is expressed as

$$\Phi = \xi B k_x^2 + (V_x - c_x)k_x, \quad V_x = \frac{x}{t}. \tag{C.12}$$

The integral C.11 is evaluated through complex contour integration, and contours are chosen such that they move through saddle points; this enables the method of steepest descent to be applied as t approaches infinity. To apply the method, saddle points, k_s, are determined by writing the derivatives of Φ as

$$\frac{d\Phi}{dk_x}(k_s) = 2\xi B k_s + (V_x - c_x) = 0, \tag{C.13}$$

$$\frac{d^2\Phi}{dk_x^2}(k_s) = 2\xi B \neq 0, \tag{C.14}$$

to yield

$$k_s = \frac{(c_x - V_x)}{2\xi B}, \qquad V_x = \frac{x}{t}. \tag{C.15}$$

In taking the derivative, we hold V_x, B, and ξ fixed. Note that for any velocity, $\hat{V}$, the saddle point is purely real. The complex integration contour for $\mathcal{Q}_x$ through the saddle point k_s is shown in Figure C.1. The angles, γ_1 and γ_2 are chosen such that the contours can be evaluated (see Supplemental Material Section C.3.4). Because there are no poles enclosed in either side of the contour, the following equations must be true:

$$0 = \int_{C_{1a}} e^{i\Phi t} dk_x + \int_{C_3 b} e^{i\Phi t} dk_x + \int_{C_4} e^{i\Phi t} dk_x, \tag{C.16}$$

$$0 = \int_{C_{1b}} e^{i\Phi t} dk_x + \int_{C_2} e^{i\Phi t} dk_x + \int_{C_3 a} e^{i\Phi t} dk_x. \tag{C.17}$$

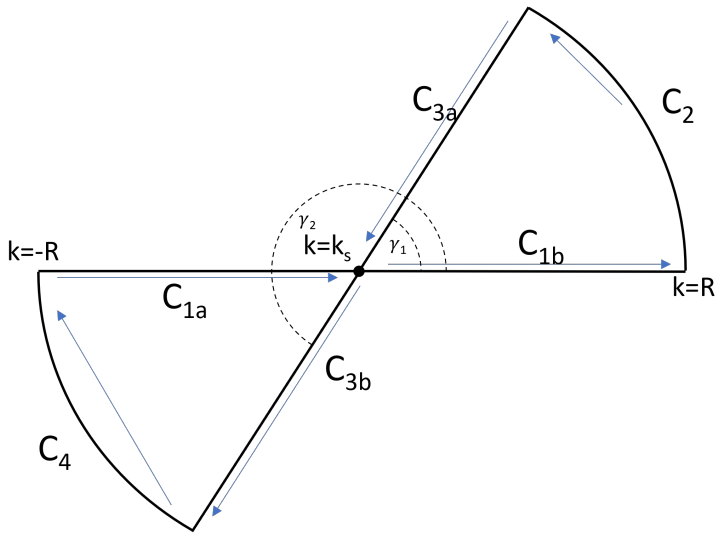

Figure C.1: Integration path for $\mathcal{Q}_x$. Note that (C.15) indicates that the saddle point k_s always lies on the real axis.

Additionally, the contours are established such that

$$\mathcal{Q}_x = \lim_{R\to\infty}\left[\int_{C_{1a}} e^{i\Phi t}dk_x + \int_{C_{1b}} e^{i\Phi t}dk_x\right]. \tag{C.18}$$

Therefore, $\mathcal{Q}_x$ can be evaluated as

$$\mathcal{Q}_x = \lim_{R\to\infty}\left[-\int_{C_2} e^{i\Phi t}dk_x - \int_{C_{3a}} e^{i\Phi t}dk_x - \int_{C_{3b}} e^{i\Phi t}dk_x - \int_{C_4} e^{i\Phi t}dk_x\right]. \tag{C.19}$$

Although motivated by the method of steepest descent to extract long-time behavior, the contours in Figure C.1 enable the exact evaluation of the integrals in (C.19) for all time (see Supplemental Material Section C.3.4.1). After evaluating (C.19) and applying the same methodology to $\mathcal{Q}_z$, $\mathcal{W}_x$, and $\mathcal{W}_z$ in (C.10) above, we obtain

$$\mathcal{Q} = \frac{i\pi}{\xi Bt} e^{\left(\frac{-i}{4\xi B}\left((V_x-c_x)^2+(V_z-c_z)^2\right)t\right)}, \tag{C.20}$$

$$\mathcal{W} = \frac{-i\pi}{\xi Bt} e^{\left(\frac{it}{4\xi B}\left((V_x-c_x)^2+(V_z-c_z)^2\right)\right)}. \tag{C.21}$$

C.1.3 Difference in response breadth between 1D-KRK and 2D-KRK responses

As mentioned in Section IV.4.1, the difference in width between the 1D-KRK and 2D-KRK peaks can be extracted by plotting the data normalized by peak height.

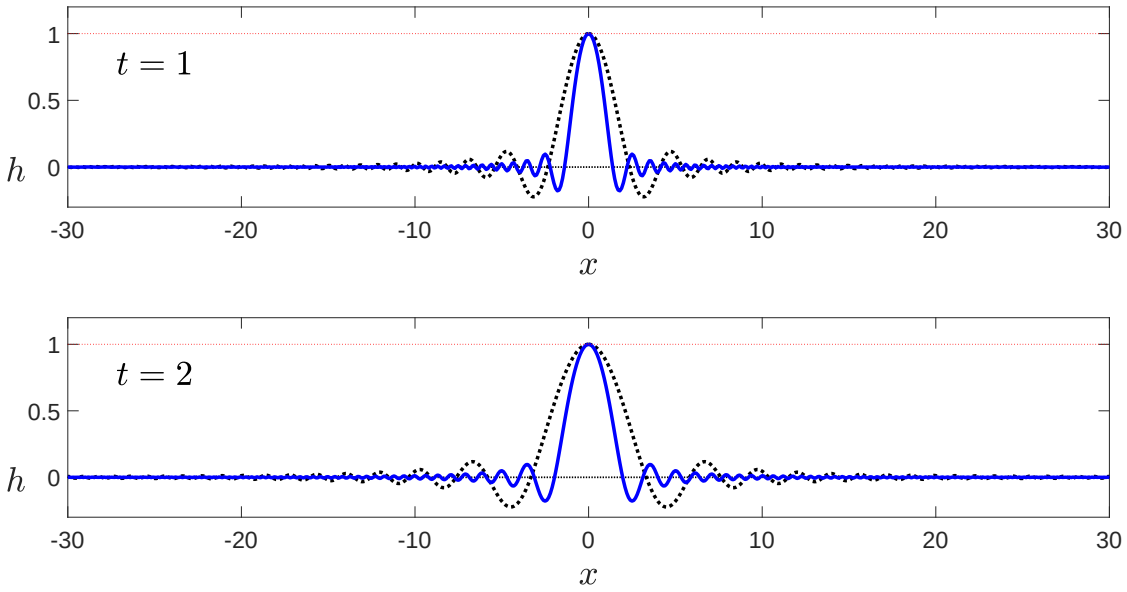

Figure C.2: A comparison between the 1D solution (IV.39a) (dotted black lines) and the 2D asymptotic solution (IV.12a) (solid blue lines) with data normalized to the respective peaks. Just as with Figure IV.8, the data were generated with $A = 10$ and $B = 1$.

Note that the 1D solution in Figure C.2 has nontrivial features that extend farther in the x-direction (i.e., has a larger breadth) than that of the 2D solution, as described and justified in Section IV.4.1. This difference is further demonstrated in the regions away from $x/t = 0$ by normalizing both data sets. The finer structure of the 2D-KRK solution in Figure IV.8 are lost because of the the difference in amplitudes between the 1D and 2D

solutions.

C.2. Appendix: 2D-CMH: Analysis

C.2.1 Fourier Series Solution (FSS)

The FSS for (IV.22) is found using standard methods [21] subject to the following initial conditions:

$$h(x,z,0) = H_0\delta(x)\delta(z), \qquad \frac{\partial h}{\partial t}(x,z,0) = U_0\delta(x)\delta(z). \tag{C.22}$$

Over the finite domains of $x \in [-L_x, L_x]$ and $z \in [-L_z, L_z]$, the FSS is

$$FSS(x,z,t) = \sum_{j=-\infty}^{\infty}\sum_{g=-\infty}^{\infty} f_{j,g}(t)e^{ik_j x}e^{ik_g z}, \qquad k_j = \frac{j\pi}{L_x}, \quad k_g = \frac{g\pi}{L_z}, \tag{C.23a}$$

$$f_{j,g} = e^{-\frac{\eta}{2}t}\left(\frac{1}{4L_xL_z}\right)\left(H_0\cos\left(\frac{\eta\sqrt{3}}{2}t\right) + 2\frac{\psi}{\eta}\sin\left(\frac{\eta\sqrt{3}}{2}t\right)\right), \tag{C.23b}$$

$$\psi = \frac{1}{\sqrt{3}}\left((A+U_0) + \frac{1}{2}\eta H_0)\right), \qquad \eta = (k_j^2 + k_g^2). \tag{C.23c}$$

C.2.2 Long-time asymptotic behavior of θ integral in (IV.24)

C.2.2.1 Phase Function and Saddle Points for Method Of Steepest Descent

The integral in θ from IV.24 is evaluated asymptotically using the method of steepest descent as $t \to \infty$. To do so, we first rewrite the integral in terms of a phase function Φ, so

$$\mathcal{I}_\theta = \int_0^{2\pi} e^{i\Phi t}d\theta, \quad \Phi = (\cos(\theta)V_x + \sin(\theta)V_z)\,\xi. \tag{C.24}$$

According to the method, derivatives of $\Phi(\theta)$ are taken to find relevant saddle points.

$$\frac{d\Phi}{d\theta} = (-\sin(\theta)V_x + \cos(\theta)V_z)\,\xi, \tag{C.25}$$

$$\frac{d^2\Phi}{d\theta^2} = -\left(\cos(\theta)V_x + \sin(\theta)V_z\right)\xi, \tag{C.26}$$

We observe that $\Phi(\theta)$ has relevant 2^{nd} order saddle points, θ_s, where the first derivative is zero and the second derivative is non-zero. These points are defined as

$$\theta_s = \arctan\left(\frac{V_z}{V_x}\right) + n\pi. \tag{C.27}$$

Note that, for integers $m = 1, 2, 3, ...$, the odd derivatives, $2m-1$, are zero at $\theta = \theta_s$ and the signs of the even derivatives alternate as $(-1)^m\left(\cos(\theta_s)V_x + \sin(\theta_s)V_z\right)$. According to the method of steepest descent, the asymptotic behavior of the integral (C.24) will be dominated by the region near the saddle point. To this end, the phase function Φ is linearized near the saddle point as

$$\Phi_{\theta_s} = \Phi(\theta_s)\left(\sum_{n=0}^{\infty}\frac{(-1)^n}{(2n)!}(\theta-\theta_s)^{2n}\right). \tag{C.28}$$

In (C.28), note that Φ_{θ_s} denotes the Taylor series expansion of Φ near the saddle point, and $\Phi^{(n)}(\theta_s)$ denotes the n^{th} derivative of Φ evaluated at the saddle point. Dropping the higher orders of $(\theta-\theta_s)$, we are left with

$$\Phi_{\theta_s} \sim \Phi(\theta_s)\left(1 - \frac{1}{2}(\theta-\theta_s)^2 + O\Big[(\theta-\theta_s)^4\Big]\right) \quad \text{as } \theta \to \theta_s, \tag{C.29}$$

which is sufficient to extract the leading order behavior of the integral (C.24) in what follows.

C.2.2.2 Integration contours for θ integral in solution of 2D-CMH problem

The following is typical of the contours which are established to evaluate (C.24) and the analysis thereof. The specific layout of the phase space depends on the signs and values of

V_x and V_z. The following analysis assumes that the saddle points, θ_s do not lie on the ends of the integration contour. The case where they do is provided in Supplemental Material Section C.4.3.1.

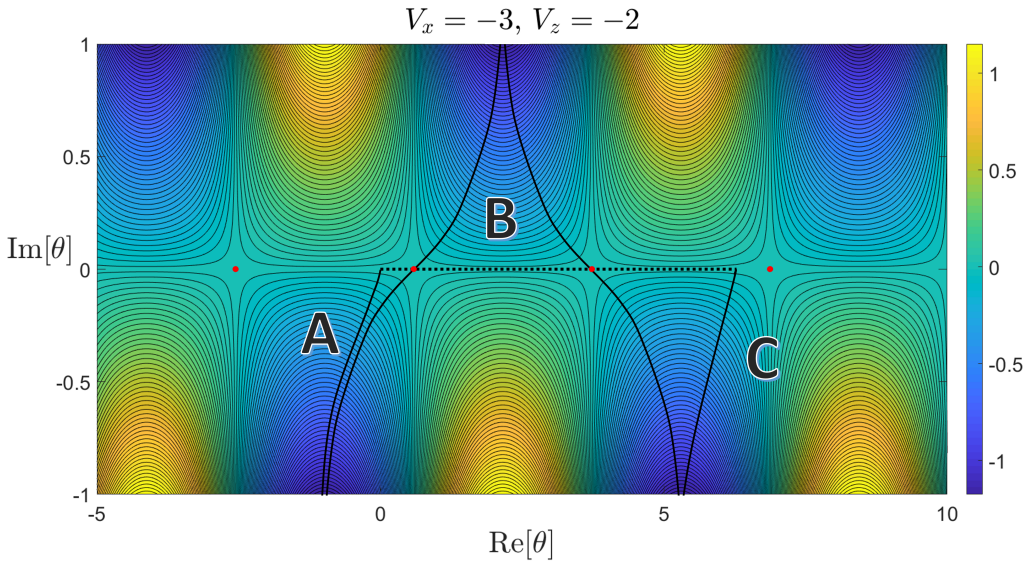

Figure C.3: Contours of constant Re$[i\Phi]$ as a function of Re$[\theta]$ and Im$[\theta]$ from (C.24). The integral of interest is marked with a dotted line running between $\theta = 0$ and $\theta = 2\pi$. Saddle points at $\theta_s = \arctan(V_z/V_x) + n\pi$ are marked with (•). Three closed contours are established which each contain a portion of the integral of interest. Each saddle point is at the maximum value of the contour, with each contour closing as Im$[\theta] \to \pm\infty$ which equates to Re$[i\Phi] \to -\infty$. Each contour will be generalized as three triangles in Figure C.4.

For the following analysis, the contours are generalized to be three triangles as shown below.

Because there are no poles (enclosed or otherwise), the closed contours in Figures C.4 lead

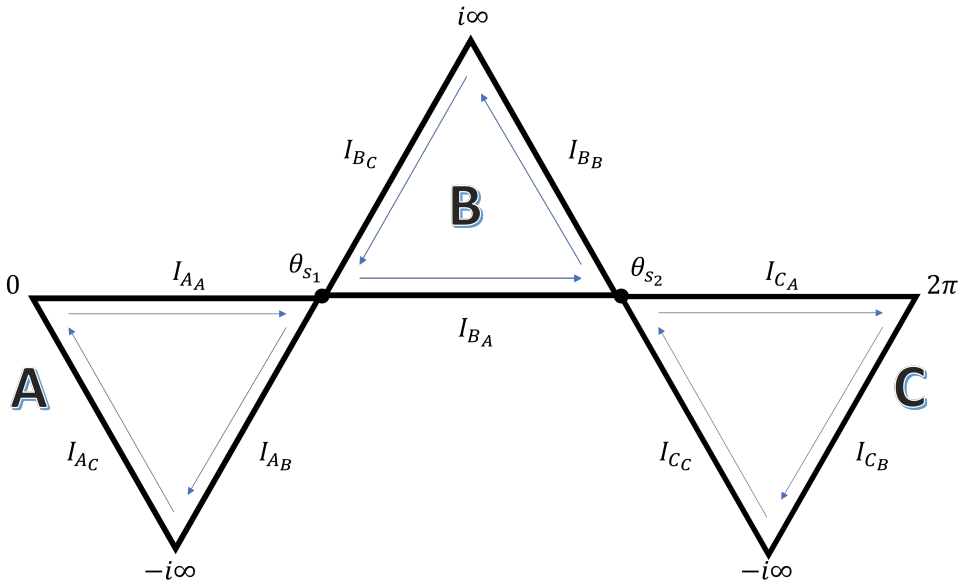

Figure C.4: Simplified schematic of the contours in Figure C.3. The integration contour for (C.24) is given by the sub-contours I_{A_A}, I_{B_A}, and I_{C_A}. The remaining sub-contours serve to form three closed contours, A, B, and C. The points θ_{S_1} and θ_{S_2} are two saddle points which lie on the integration contour. Note that two saddles will always lie on the θ contour if $V_z/V_x \neq 0$ as per (C.27).

to the following equations:

$$0 = \oint_A = \mathcal{I}_{A_A} + \mathcal{I}_{A_B} + \mathcal{I}_{A_C}, \tag{C.30a}$$

$$0 = \oint_B = \mathcal{I}_{B_A} + \mathcal{I}_{B_B} + \mathcal{I}_{B_C}, \tag{C.30b}$$

$$0 = \oint_C = \mathcal{I}_{C_A} + \mathcal{I}_{C_B} + \mathcal{I}_{C_C}, \tag{C.30c}$$

which can be rearranged as

$$\mathcal{I}_{A_A} = -\mathcal{I}_{A_B} - \mathcal{I}_{A_C}, \tag{C.31a}$$

$$\mathcal{I}_{B_A} = -\mathcal{I}_{B_B} - \mathcal{I}_{B_C}, \tag{C.31b}$$

$$\mathcal{I}_{C_A} = -\mathcal{I}_{C_B} - \mathcal{I}_{C_C}. \tag{C.31c}$$

As we are considering the cases where a saddle point does not lie at 0 or 2π (the limits of integration for (C.24)), it is observed that contours without saddle points are asymptotically subdominant to those with saddle points as t goes off to infinity. The equations can be written as

$$\mathcal{I}_{A_A} \sim -\mathcal{I}_{A_B} \quad \text{as } t \to \infty, \tag{C.32a}$$

$$\mathcal{I}_{B_A} = -\mathcal{I}_{B_B} - \mathcal{I}_{B_C}, \tag{C.32b}$$

$$\mathcal{I}_{C_A} \sim -\mathcal{I}_{C_C} \quad \text{as } t \to \infty. \tag{C.32c}$$

The total integral in θ can therefore be written asymptotically as

$$\mathcal{I}_\theta \sim -\mathcal{I}_{A_B} - \mathcal{I}_{B_B} - \mathcal{I}_{B_C} - \mathcal{I}_{C_C} \quad \text{as } t \to \infty. \tag{C.33}$$

The integral along a sub-contour (I_{A_B}, I_{B_C}, I_{B_B}, or I_{C_C}), denoted here as $\int_S$, can be written in terms of the radial distance r and angle γ relative to a saddle point. This is done by letting $\theta = \theta_s + re^{i\gamma}$, $d\theta = e^{i\gamma}dr$. Fundamentally, each sub-integral can be broken up into two regions, the region near the saddle point, and the rest of the path.

Along a sub-contour, the region near the saddle point is asymptotically dominant over the rest of the path though integration by parts. Additionally, when looking near the saddle point, Φ can be linearized using (C.29). Then, the upper bound of integration can be increased to infinity, accruing only asymptotically subdomninant terms [34]. In the conversion to radial coordinates, the angle γ is the angle of approach or departure of the steepest contours through the saddle point; the steepest paths are perpendicular to the contours of constant $\mathrm{Re}[i\Phi]$ in the complex θ plane. The values of γ are chosen such that the integrand takes the form of $e^{-r^2}dr$. Using "$\pm$" to denote that the sign depends on the

particular sub-contour being examined,

$$\int_S \sim \pm e^{i\Phi(\theta_s)t+i\gamma} \int_0^\infty e^{-\frac{\Phi(\theta_s)}{2}r^2 t} dr \quad \text{as } t \to \infty, \tag{C.34}$$

which evaluates to

$$\int_S \sim \pm e^{i\Phi(\theta_s)t+i\gamma} \sqrt{\frac{\pi}{2\Phi(\theta_s)t}} \quad \text{as } t \to \infty. \tag{C.35}$$

Applying the method to each sub-contour in (C.33), the overall integral in θ is expressed asymptotically as

$$\mathcal{I}_\theta \sim 2\cos\left(\xi\hat{V}t - \frac{\pi}{4}\right)\sqrt{\frac{2\pi}{\hat{V}t}} \quad \text{as } t \to \infty, \tag{C.36}$$

where

$$\hat{V} = \sqrt{V_x^2 + V_z^2}. \tag{C.37}$$

Note that when the saddle points lie on the ends of the integration contour, the solution is equivalent (Supplemental Material Section C.4.3.1).

C.2.3 Criterion for agreement between asymptotic and FSS solution

As mentioned at the end of Section IV.3, the judgment of when Φ is sufficiently large for the FSS (Appendix C.2.1) and asymptotic solution (IV.38) to agree is made based on Figure C.5. Here, one can observe that for $\Phi \geq 11.4$, indicated in Figure C.5, the magnitude of the error is less than $A/(600\sqrt{3}) \approx 0.01$ (1% of the peak height given by (IV.38b)).

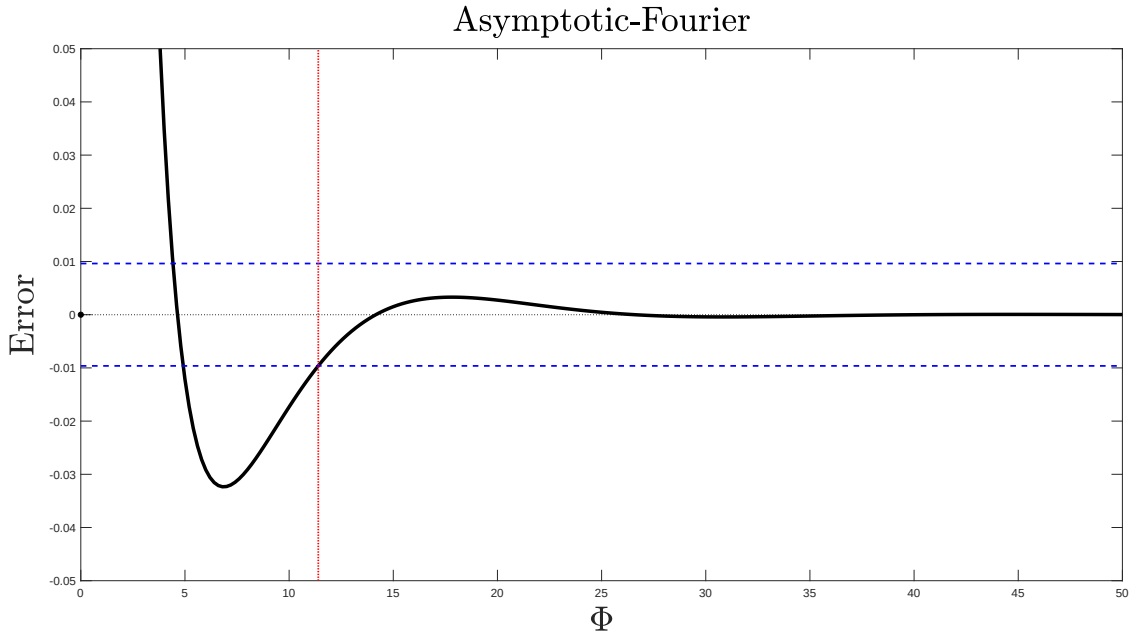

Figure C.5: The difference between the asymptotic solution (IV.38) and the FSS (Appendix C.2.1) versus Φ. The blue dashed lines denote where the difference between the two solutions is equal to $\pm 1\%$ of the exact peak height in (IV.38b). A vertical red line marks the value of $\Phi = 11.4$ above which the error is between the marked bounds. The black dotted line marks the Φ axis.

C.3. Supplemental Material: 2D-KRK: Analysis

C.3.1 Evaluating h for initial height disturbance

Equation (C.8) is transcribed below for completeness.

$$h = H_0 \int_{-\infty}^{\infty}\int_{-\infty}^{\infty} \left(\left(\frac{\psi+\eta}{\eta} \right) \left(\frac{e^{i\eta t} - e^{-i\eta t}}{2} \right) + e^{-i\eta t} \right) e^{-i\psi t} e^{ik_x V_x t} e^{ik_z V_z t} dk_z dk_x,$$

$$\psi = c_x k_x + c_z k_z, \quad \eta = k_x^2 + k_z^2, \quad V_x = \frac{x}{t}, \quad V_z = \frac{z}{t}. \tag{C.38}$$

Equation (C.38) is broken up as

$$h(x,z,t) = \frac{H_0}{4\pi^2}(\mathcal{A}+\mathcal{B}+\mathcal{C}), \tag{C.39}$$

$$\mathcal{A} = \int_{-\infty}^{\infty}\int_{-\infty}^{\infty} e^{-i\psi t}\left(\frac{i\psi(e^{i\eta t}-e^{-i\eta t})}{2i\eta}\right)e^{ik_x x}e^{ik_z z}dk_z dk_x, \tag{C.40}$$

$$\mathcal{B} = \int_{-\infty}^{\infty}\int_{-\infty}^{\infty} e^{-i\psi t}\left(\frac{i\eta(e^{i\eta t}-e^{-i\eta t})}{2i\eta}\right)e^{ik_x x}e^{ik_z z}dk_z dk_x, \tag{C.41}$$

$$\mathcal{C} = \int_{-\infty}^{\infty}\int_{-\infty}^{\infty} e^{-i\psi t}\left(e^{-i\eta t}\right)e^{ik_x x}e^{ik_z z}dk_z dk_x, \tag{C.42}$$

$$\psi = c_x k_x + c_z k_z, \quad \eta = k_x^2 + k_z^2. \tag{C.43}$$

C.3.1.1 Solution to $\mathcal{A}$ (sub-integral of h)

The integral $\mathcal{I}$ is established such that

$$\mathcal{I} = \frac{-1}{t}\int_{-\infty}^{\infty}\int_{-\infty}^{\infty} e^{-i\gamma\psi t}\left(\frac{\sin(\eta t)}{\eta}\right)e^{ik_x x}e^{ik_z z}dk_z dk_x, \tag{C.44}$$

$$\left.\frac{\partial\mathcal{I}}{\partial\gamma}\right|_{\gamma=1} = \mathcal{A}. \tag{C.45}$$

Another parameter, α, is introduced into (C.44) such that

$$\hat{\mathcal{I}} = \frac{-1}{t}\int_{-\infty}^{\infty}\int_{-\infty}^{\infty} e^{-i\gamma\psi t}\left(\frac{\sin(\alpha\eta t)}{\eta}\right)e^{ik_x x}e^{ik_z z}dk_z dk_x, \tag{C.46}$$

$$\left.\hat{\mathcal{I}}\right|_{\alpha=0} = 0, \quad \left.\hat{\mathcal{I}}\right|_{\alpha=1} = \mathcal{I}. \tag{C.47}$$

The derivative is taken with respect to α,

$$\frac{\partial\hat{\mathcal{I}}}{\partial\alpha} = -\int_{-\infty}^{\infty}\int_{-\infty}^{\infty} e^{-i\gamma\psi t}\left(\cos(\alpha\eta t)\right)e^{ik_x x}e^{ik_z z}dk_z dk_x. \tag{C.48}$$

Through the same steps as laid out for $\partial h/\partial\xi$ in Section IV.2.4, we find that

$$\frac{\partial\hat{\mathcal{I}}}{\partial\alpha} = \frac{-\pi}{\alpha B t}\sin\left(\frac{t}{4\alpha B}\left(\hat{V}_\gamma\right)\right),$$

$$\hat{V}_\gamma = (V_x - \gamma c_x)^2 + (V_z - \gamma c_z)^2. \tag{C.49}$$

Integrating in α yields

$$\mathcal{I} = \frac{\pi}{Bt}\left(\int_0^{\frac{\bar{V}_\gamma t}{4B}} \frac{1}{u}\sin(u)dv - \frac{\pi}{2}\right), \tag{C.50}$$

and differentiating in γ yields,

$$\frac{\partial \mathcal{I}}{\partial \gamma} = -\Big(c_x(V_x - \gamma c_x) + c_z(V_z - \gamma c_z)\Big)\frac{2\pi}{\bar{V}_\gamma Bt}\sin\left(\frac{\bar{V}_\gamma t}{4B}\right). \tag{C.51}$$

From the construction of $\mathcal{I}$ in (C.45),

$$\mathcal{A} = -\Big(c_x(V_x - c_x) + c_z(V_z - c_z)\Big)\frac{2\pi}{\bar{V}Bt}\sin\left(\frac{\bar{V}t}{4B}\right) \tag{C.52}$$

C.3.1.2 Solution to $\mathcal{B}$ (sub-integral of h)

Equation (C.41) is rearranged into the form

$$\mathcal{B} = \frac{1}{2}\int_{-\infty}^{\infty} e^{(iBk_x^2 + i(V_x - c_x)k_x)t}\int_{-\infty}^{\infty} e^{(iBk_z^2 + i(V_z - c_z)k_z)t}dk_z dk_x$$
$$-\frac{1}{2}\int_{-\infty}^{\infty} e^{(-iBk_x^2 + i(V_x - c_x)k_x)t}\int_{-\infty}^{\infty} e^{(-iBk_z^2 + i(V_z - c_z)k_z)t}dk_z dk_x \tag{C.53}$$

Combined with (IV.10b) and (IV.10c, it is shown in Section C.3.4 that

$$\mathcal{Q} = \int_{-\infty}^{\infty} e^{\left(i\xi Bk_z^2 + i(\frac{z}{t} - c_z)k_z\right)t}\left[\int_{-\infty}^{\infty} e^{\left(i\xi Bk_x^2 + i(\frac{x}{t} - c_x)k_x\right)t}dk_x\right]dk_z = \frac{i\pi}{\xi Bt}e^{\left(\frac{-it}{4\xi B}\left((c_x - V_x)^2 + (c_z - V_z)^2\right)\right)}, \tag{C.54}$$

$$\mathcal{W} = \int_{-\infty}^{\infty} e^{\left(-i\xi Bk_z^2 + i(\frac{z}{t} - c_z)k_z\right)t}\left[\int_{-\infty}^{\infty} e^{\left(-i\xi Bk_x^2 + i(\frac{x}{t} - c_x)k_x\right)t}dk_x\right]dk_z = \frac{-i\pi}{\xi Bt}e^{\left(\frac{it}{4\xi B}\left((V_x - c_x)^2 + (V_z - c_z)^2\right)\right)}. \tag{C.55}$$

Therefore,

$$\mathcal{B} = \frac{i\pi}{Bt}\cos\left(\frac{t}{4B}\left((V_x - c_x)^2 + (V_z - c_z)^2\right)\right). \tag{C.56}$$

C.3.1.3 Solution to $\mathcal{C}$ (sub-integral of h)

Using results in Section C.3.4 to follow and combining with (IV.10b), we obtain

$$\mathcal{W} = \int_{-\infty}^{\infty} e^{\left(-i\xi B k_z^2 + i(\frac{z}{t} - c_z)k_z\right)t} dk_z \int_{-\infty}^{\infty} e^{\left(-i\xi B k_x^2 + i(\frac{x}{t} - c_x)k_x\right)t} dk_x$$

$$= \frac{-i\pi}{\xi B t} e^{\left(\frac{it}{4\xi B}\left((V_x - c_x)^2 + (V_z - c_z)^2\right)\right)}, \quad \text{(C.57)}$$

$$\mathcal{C} = \frac{-i\pi}{Bt} e^{\left(\frac{it}{4B}\left((V_x - c_x)^2 + (V_z - c_z)^2\right)\right)}. \quad \text{(C.58)}$$

C.3.1.4 Assembling sub-integrals to obtain the solution to h

Substituting the results from Sections C.3.1.1, C.3.1.2, and C.3.1.3 into C.39 yields

$$h(x,z,t) = \frac{H_0}{4\pi^2}\Bigg(-\Big(c_x(V_x - c_x) + c_z(V_z - c_z)\Big)\frac{2\pi}{\bar{V}Bt}\sin\left(\frac{\bar{V}t}{4B}\right)$$
$$+ \frac{i\pi}{Bt}\cos\left(\frac{t}{4B}((V_x - c_x)^2 + (V_z - c_z)^2)\right) + \frac{-i\pi}{Bt} e^{\left(\frac{it}{4B}\left((V_x - c_x)^2 + (V_z - c_z)^2\right)\right)}\Bigg), \quad \text{(C.59)}$$

which can be rearranged into the form found in (C.9) in the appendix, transcribed below for completeness

$$h(x,z,t) = \frac{H_0}{4Bt\pi}\left(1 - 2\frac{c_x(V_x - c_x) + c_z(V_z - c_z)}{\hat{V}}\right)\sin\left(\frac{\hat{V}t}{4B}\right),$$
$$\hat{V} = \sqrt{(V_x - c_x)^2 + (V_z - c_z)^2}. \quad \text{(C.60)}$$

C.3.2 Development of Fourier inversion integral for 2D-KRK operator

Taking the Fourier transforms in x and z of the 2D-KRK operator (IV.4) yields a second order ordinary differential equation of the Fourier transformed variable, $\hat{\hat{h}}_{xz}(t)$.

$$\hat{\hat{h}}_{xz} = \frac{A}{\eta} e^{-i\psi t}\left(\frac{e^{i\eta t} - e^{-i\eta t}}{2i}\right), \qquad \psi = c_x k_x + c_z k_z, \qquad \eta = B(k_x^2 + k_z^2), \quad \text{(C.61)}$$

$$\hat{\hat{h}}_{xz}(0) = 0, \qquad \frac{d\hat{\hat{h}}_{xz}}{dt}(0) = 0, \tag{C.62}$$

$$\psi = c_x k_x + c_z k_z, \qquad \eta = B(k_x^2 + k_z^2). \tag{C.63}$$

Note that, in this construction, ψ and η are always real and η is non-negative. The inverse Fourier transforms (in x and z) are reproduced here from the main text (IV.6) for completeness:

$$h(x,z,t) = \frac{1}{4\pi^2} \int_{-\infty}^{\infty}\int_{-\infty}^{\infty} \hat{\hat{h}}_{xz} e^{ik_x x} e^{ik_z z} dk_z dk_x, \tag{C.64}$$

$$h(x,z,t) = \frac{A}{4\pi^2} \int_{-\infty}^{\infty}\int_{-\infty}^{\infty} e^{-i\psi t}\left(\frac{\sin(\eta t)}{\eta}\right) e^{ik_x x} e^{ik_z z} dk_z dk_x \qquad \eta = B(k_x^2 + k_z^2). \tag{C.65}$$

C.3.3 Evaluating inversion integral through the introduction of ξ

The variable ξ is introduced to create the function $\tilde{h}(x,z,t,\xi)$ such that

$$\tilde{h}(x,z,t,0) = 0, \qquad \tilde{h}(x,z,t,1) = h(x,z,t), \tag{C.66}$$

$$\tilde{h}(x,z,t,\xi) = \frac{A}{4\pi^2} \int_{-\infty}^{\infty}\int_{-\infty}^{\infty} e^{-i\psi t}\left(\frac{\sin(\xi\eta t)}{\eta}\right) e^{ik_x x} e^{ik_z z} dk_z dk_x. \tag{C.67}$$

The derivative is taken with respect to ξ,

$$\frac{\partial \tilde{h}}{\partial \xi} = \frac{At}{4\pi^2} \int_{-\infty}^{\infty}\int_{-\infty}^{\infty} e^{-i\psi t} \cos(\xi B(k_x^2 + k_z^2)t) e^{ik_x x} e^{ik_z z} dk_z dk_x, \tag{C.68}$$

and thus, in accordance with (C.66), we have

$$h(x,z,t) = \int_0^1 \frac{\partial \tilde{h}}{\partial \xi} d\xi. \tag{C.69}$$

The function $\partial\tilde{h}/\partial\xi$ is evaluated as described in Appendix C.1.2 resulting in the following:

$$\frac{\partial \tilde{h}}{\partial \xi} = \frac{A}{4\xi B\pi} \sin\left(\frac{t}{4\xi B}\left((V_x - c_x)^2 + (V_z - c_z)^2\right)\right). \tag{C.70}$$

Through (C.69), we obtain

$$h(x,z,t) = \int_0^1 \frac{A}{4\xi B\pi} \sin\left(\frac{t}{4\xi B}\left((V_x - c_x)^2 + (V_z - c_z)^2\right)\right) d\xi, \tag{C.71}$$

which can be rearranged to

$$h(x,z,t) = \frac{A}{4B\pi}\left(\frac{\pi}{2} - \int_0^{\frac{\hat{V}t}{4B}} \frac{1}{u}\sin(u)du\right),$$

$$\hat{V} = \sqrt{(V_x - c_x)^2 + (V_z - c_z)^2}. \tag{C.72}$$

Note that, when (C.72) is written in terms of $\Phi = \hat{V}^2 t$, the result is (IV.12a).

C.3.4 Evaluation of $\mathcal{Q}$ and $\mathcal{W}$ integrals

According to (C.10), the $\mathcal{Q}$ and $\mathcal{W}$ integrals consist of the product of an integral in x and an integral in z. Each sub-integral is handled separately in the following sections.

C.3.4.1 Evaluation of $\mathcal{Q}_x$ sub-integral

Working from the analysis in C.1.2, the integrals in the following expression

$$\mathcal{Q}_x = \lim_{R\to\infty}\left[-\int_{C_2} e^{i\Phi t}dk_x - \int_{C_3a} e^{i\Phi t}dk_x - \int_{C_4} e^{i\Phi t}dk_x - \int_{C_3b} e^{i\Phi t}dk_x\right] \tag{C.73}$$

need to be evaluated. Because the angles depicted in Figure C.1 are limited to be in the intervals

$$\gamma_1 \in \left[0, \frac{\pi}{2}\right], \quad \gamma_2 \in \left[\pi, \frac{3\pi}{2}\right], \tag{C.74}$$

the integral along contours C_2 and C_4 go to zero as R goes to infinity as Jordan arcs. The process for evaluating the two remaining contours is the same for both C_{3a} and C_{3b} (differing only in the direction of integration and value of γ). Therefore, only the evaluation

along C_{3a} will be transcribed below. The integrand is rotated and shifted through the substitution of $k = k_s + re^{i\gamma}$, $dk = e^{i\gamma}dr$ to yield

$$\int_{C_3a} e^{i\Phi t}dk_x = \int_{\infty}^{0} e^{\left(-i\frac{(c_x-V_x)^2}{4\xi B}\right)t} e^{\left(i\xi Br^2e^{2i\gamma_1}\right)t} e^{i\gamma_1}dr. \tag{C.75}$$

The value of γ_1 in (C.74) is chosen to be $\pi/4$, to obtain

$$\int_{C_3a} e^{i\Phi t}dk_x = -e^{i\frac{\pi}{4}} e^{\left(-i\frac{(c_x-V_x)^2}{4\xi B}\right)t} \int_{0}^{\infty} e^{\left(-\xi Br^2\right)t}dr, \tag{C.76}$$

$$\int_{C_3a} e^{i\Phi t}dk_x = -\frac{1}{2}e^{i\frac{\pi}{4}} e^{\left(-i\frac{(c_x-V_x)^2}{4\xi B}\right)t} \sqrt{\frac{\pi}{\xi Bt}}. \tag{C.77}$$

Applying the same process to the other contour yields

$$\mathcal{Q}_x = e^{i\frac{\pi}{4}} e^{\left(-i\frac{(c_x-V_x)^2}{4\xi B}\right)t} \sqrt{\frac{\pi}{\xi Bt}}. \tag{C.78}$$

C.3.4.2 Evaluation of $\mathcal{Q}_z$ sub-integral

The structure of the integral $\mathcal{Q}_z$ is identical to that of $\mathcal{Q}_x$ with z instead of x. Therefore,

$$\mathcal{Q}_z = e^{i\frac{\pi}{4}} e^{\left(-i\frac{(c_z-V_z)^2}{4\xi B}\right)t} \sqrt{\frac{\pi}{\xi Bt}}. \tag{C.79}$$

C.3.4.3 Evaluation of $\mathcal{W}_x$ sub-integral

The sub-integral $\mathcal{W}_x$ is

$$\mathcal{W}_x = \int_{-\infty}^{\infty} e^{\left(-i\xi Bk_x^2 + i\left(\frac{x}{t}-c_z\right)k_x\right)t}dk_x. \tag{C.80}$$

The integrand of (C.80) is expressed in the following form,

$$\mathcal{W}_x = \int_{-\infty}^{\infty} e^{i(\Phi(k_x))t}dk_x \tag{C.81}$$

where

$$\Phi = -\xi B k_x^2 + (V_x - c_x)k_x, \quad V_x = \frac{x}{t}. \tag{C.82}$$

The derivatives of Φ are

$$\frac{d\Phi}{dk_x} = -2\xi B k_x + (V_x - c_x), \tag{C.83}$$

$$\frac{d^2\Phi}{dk_x^2} = -2\xi B. \tag{C.84}$$

The function Φ has a second order saddle point, k_s, at

$$k_s = \frac{(V_x - c_x)}{2\xi B}, \qquad V_x = \frac{x}{t}. \tag{C.85}$$

Note that, for any velocity ray, the saddle point is purely real. A typical integration contour takes the form of Figure C.6 centered on the saddle point k_s.

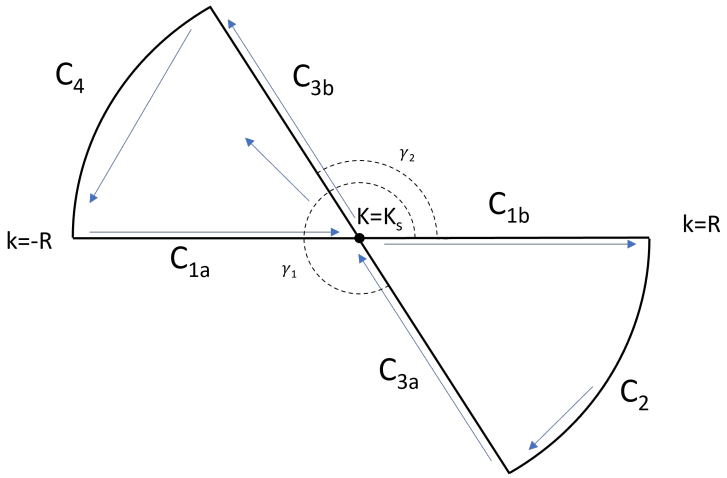

Figure C.6: Integration path for $\mathcal{W}_x$. Note that, through equation (C.85) the saddle point k_s always lies on the real axis.

Because there are no poles enclosed in either contour, the following must be true from

Cauchy's theorem:

$$0 = \int_{C_{1a}} e^{i\Phi t} dk_x + \int_{C_3 a} e^{i\Phi t} dk_x + \int_{C_4} e^{i\Phi t} dk_x, \tag{C.86}$$

$$0 = \int_{C_{1b}} e^{i\Phi t} dk_x + \int_{C_2} e^{i\Phi t} dk_x + \int_{C_3 b} e^{i\Phi t} dk_x. \tag{C.87}$$

Additionally,

$$\mathcal{W}_x = \lim_{R\to\infty} \left[\int_{C_{1a}} e^{i\Phi t} dk_x + \int_{C_{1b}} e^{i\Phi t} dk_x \right]. \tag{C.88}$$

Therefore, $\mathcal{W}_x$ can be evaluated as

$$\mathcal{W}_x = \lim_{R\to\infty} \left[-\int_{C_2} e^{i\Phi t} dk_x - \int_{C_3 a} e^{i\Phi t} dk_x - \int_{C_2} e^{i\Phi t} dk_x - \int_{C_3 b} e^{i\Phi t} dk_x \right]. \tag{C.89}$$

The evaluation of (C.89) is done with the same process as applied in Section C.3.4.1, except that the angles γ_1 and γ_2 in Figure C.6 lie in the ranges of

$$\gamma_1 \in \left[\frac{\pi}{2}, \pi \right], \quad \gamma_2 \in \left[\frac{3\pi}{2}, 2\pi \right]. \tag{C.90}$$

Applying the same method as for $\mathcal{Q}_x$, the integrals evaluate to

$$\mathcal{W}_x = -e^{i\frac{3\pi}{4}} e^{i\frac{(V_x - c_x)^2}{4\xi B} t} \sqrt{\frac{\pi}{\xi B t}}. \tag{C.91}$$

C.3.4.4 Evaluation of $\mathcal{W}_z$ sub-integral

The structure of the integral $\mathcal{W}_z$ is identical to that of $\mathcal{W}_x$ with z instead of x. Therefore,

$$\mathcal{W}_z = -e^{i\frac{3\pi}{4}} e^{i\frac{(V_z - c_z)^2}{4\xi B} t} \sqrt{\frac{\pi}{\xi B t}}. \tag{C.92}$$

C.4. Supplemental Material: 2D-CMH: Analysis

C.4.1 The effect of initial conditions on the stability of 2D-CMH solutions

Following the same steps as in Section C.4.2, the following is obtained for the solution to (IV.22) in the algebraic domain (the inverse Laplace transform is not necessary for this step),

$$\hat{H} = \frac{(A + U_0) + sH_0 + \eta H_0}{s^2 + \eta s + \eta^2}, \quad \eta = k_x^2 + k_z^2. \tag{C.93}$$

Note that the forcing amplitude A and the initial height disturbance U_0 have the exact same effect.

C.4.2 Development of the Fourier Inversion Integral for 2D-CMH operator

Taking Fourier transforms in x and z are taken of the 2D-CMH operator (IV.22) yields a second order ordinary differential equation of the Fourier transformed variable, $\hat{\hat{h}}_{xz}(t)$.

$$\frac{d^2\hat{\hat{h}}_{xz}}{dt^2} + \Big(\eta + B\Big)\frac{d\hat{\hat{h}}_{xz}}{dt} + \Big(\eta^2 + B^2\Big)\hat{\hat{h}}_{xz} = A\delta(t). \tag{C.94}$$

$$\hat{\hat{h}}_{xz}(0) = 0, \quad \frac{d\hat{\hat{h}}_{xz}}{dt}(0) = 0, \quad \eta = k_x^2 + k_z^2. \tag{C.95}$$

Note that, in this construction, η is always real and non-negative.

Equation (C.94) is evaluated through a Laplace transform to yield the Fourier inversion integrals:

$$h(x,z,t) = \frac{A}{2\pi^2\sqrt{3}} \int_{-\infty}^{\infty}\int_{-\infty}^{\infty} \Big(e^{-\frac{\eta}{2}t}\Big)\frac{\sin\Big(\frac{\eta}{2}\sqrt{3}t\Big)}{\eta} e^{ik_xV_xt}e^{ik_zV_zt}dk_zdk_x,$$

$$\eta = k_x^2 + k_z^2, \quad V_x = \frac{x}{t}, \quad V_z = \frac{z}{t}. \tag{C.96}$$

C.4.3 Transformation of inversion integral into polar coordinates

Equation (C.96) is converted into polar coordinates using the following definitions:

$$\xi = \sqrt{k_x^2 + k_z^2}, \quad k_x = \xi\cos(\theta), \quad k_z = \xi\sin(\theta), \quad dk_x dk_z = \xi d\xi d\theta. \tag{C.97}$$

Letting $\mathcal{B} = \cos(\theta)V_x + \sin(\theta)V_z$ gives us

$$h(x,z,t) = \frac{A}{2\pi^2\sqrt{3}} \int_0^\infty \frac{\sin\left(\frac{\sqrt{3}}{2}\xi^2 t\right)}{\xi} e^{-\frac{\xi^2}{2}t} \left(\int_0^{2\pi} e^{i\mathcal{B}\xi t} d\theta \right) d\xi. \tag{C.98}$$

Once the equation is in this form, the inner integral in θ can be evaluated followed by that of the outer integral in ξ.

C.4.3.1 Evaluation of θ integral for the special case of $V_z/V_x = 0$

In order for the saddle points (C.27) to lie on the ends of the integration contour, $V_z/V_x = 0$. This is the case when either V_z is zero and V_x is non-zero or when V_x goes to infinity for finite V_z. Note here that, in this limit, the term $\hat{V} = \sqrt{V_x^2 + V_z^2}$ is equivalent to V_x.

For the following analysis, the contours are represented schematically as two triangles as shown below.

Because there are no poles in or on the contours, each closed contour A and B can be written as

$$0 = \mathcal{I}_{A_A} + \mathcal{I}_{A_B} + \mathcal{I}_{A_C}, \tag{C.99}$$

$$0 = \mathcal{I}_{B_A} + \mathcal{I}_{B_B} + \mathcal{I}_{B_C}. \tag{C.100}$$

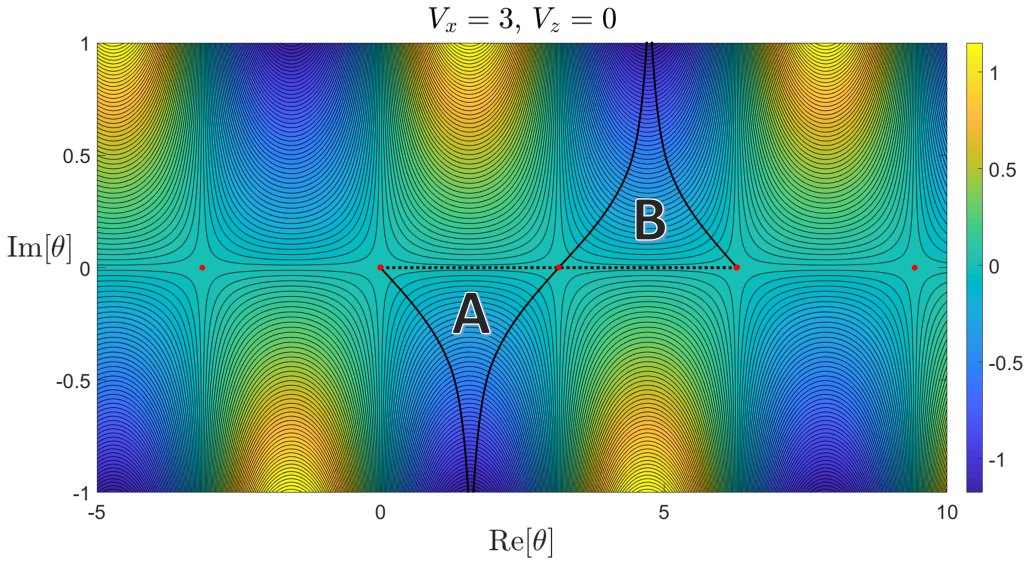

Figure C.7: Re[$i\Phi$] vs Re[θ] and Im[θ]. The integral of interest is marked with a dotted line running between $\theta = 0$ and $\theta = 2\pi$. Saddle points at $\theta_s = 0, \pi, 2\pi$ are marked with (•). Two closed contours are established which each contain a portion of the integral of interest. Each saddle point is at the maximum value of the contour, with each contour closing as Im[θ] $\to \pm\infty$ which equates to Re[$i\Phi$] $\to -\infty$. Each contour will be generalized as two triangles in Figure C.8.

Unlike the case in C.2.2, none of the contours can be neglected as time gets large. The integral $\mathcal{I}_\theta$ can be evaluated as

$$\mathcal{I}_\theta \sim -\mathcal{I}_{A_B} - \mathcal{I}_{A_C} - \mathcal{I}_{B_B} - \mathcal{I}_{B_C} \quad \text{as } t \to \infty. \tag{C.101}$$

Equation (C.101) is evaluated through the same method as (C.33). Doing so yields

$$\mathcal{I}_\theta \sim 2\left(\cos\left(V_x\xi t - \frac{\pi}{4}\right)\right)\sqrt{\frac{2\pi}{V_x\xi t}}, \tag{C.102}$$

which is equivalent to (IV.25).

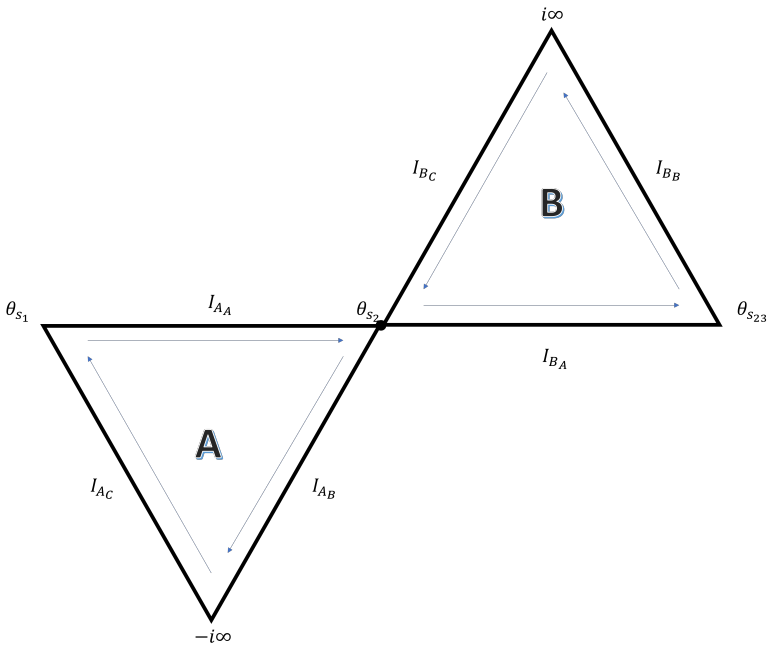

Figure C.8: Simplified schematic of Figure C.7. The integration contour for equation (C.24) is given by the sub-contours I_{A_A}, I_{B_A}. The remaining sub-contours serve to form two closed contours, A and B. The points θ_{S_1}, θ_{S_2}, and θ_{s_3} are three saddle points which lie on the integration contour. Note that the saddles lie at $\theta = (0, \pi, 2\pi)$ when $V_z/V_x = 0$ as per equation (C.27) .

C.4.3.2 Conversion of ξ integral into alternative integral J for evaluation

From (IV.27), we have

$$h\Big|_{\hat{V}\neq 0} \sim \frac{A}{2\pi^2\sqrt{3}} \int_0^\infty \frac{\sin\left(\frac{\sqrt{3}}{2}\xi^2 t\right)}{\xi} e^{-\frac{\xi^2}{2}t} \left(2\cos\left(\xi\hat{V}t - \frac{\pi}{4}\right)\sqrt{\frac{2\pi}{\hat{V}\xi t}}\right) d\xi \qquad \text{as } t\to\infty, \tag{C.103}$$

where $\hat{V} = \sqrt{V_x^2 + V_z^2}$. Let $U = \xi^2 t$, $dU = 2\xi t d\xi$, and thus

$$h\Big|_{\hat{V}\neq 0} \sim \left(\frac{(2\pi)^{\frac{1}{2}}}{\hat{V}^{\frac{1}{2}} t^{\frac{1}{4}}}\right) \int_0^\infty \frac{\sin\left(\frac{\sqrt{3}}{2}U\right)}{U^{\frac{5}{4}}} e^{-\frac{U}{2}} \cos\left(\hat{V}(Ut)^{\frac{1}{2}} - \frac{\pi}{4}\right) dU \qquad \text{as } t\to\infty. \tag{C.104}$$

Rewriting the cosine as the real part of a complex exponential, we obtain

$$h\Big|_{\hat{V}\neq 0} \sim \left(\frac{(2\pi)^{\frac{1}{2}}}{\hat{V}^{\frac{1}{2}}t^{\frac{1}{4}}}\right)\int_0^\infty \frac{\sin\left(\frac{\sqrt{3}}{2}U\right)}{U^{\frac{5}{4}}}e^{-\frac{U}{2}}\,Real\left[e^{\left(i\hat{V}(Ut)^{\frac{1}{2}}-\frac{i\pi}{4}\right)}\right]dU \qquad \text{as } t\to\infty, \quad \text{(C.105)}$$

which can be rearranged as

$$h\Big|_{\hat{V}\neq 0} \sim \left(\frac{(2\pi)^{\frac{1}{2}}}{\hat{V}^{\frac{1}{2}}t^{\frac{1}{4}}}\right) Real\left[e^{\left(-i\frac{\pi}{4}\right)}\int_0^\infty \frac{\sin\left(\frac{\sqrt{3}}{2}U\right)}{U^{\frac{5}{4}}}e^{-\frac{U}{2}}e^{\left(i\hat{V}(Ut)^{\frac{1}{2}}\right)}dU\right] \qquad \text{as } t\to\infty. \quad \text{(C.106)}$$

The result is (IV.31) and (IV.32), and is transcribed below for completeness.

$$h\Big|_{\hat{V}\neq 0} \sim \frac{A}{2\pi^2\sqrt{3}}\left(\frac{(2\pi)^{\frac{1}{2}}}{\hat{V}^{\frac{1}{2}}t^{\frac{1}{4}}}\right) Real\left[e^{\left(-i\frac{\pi}{4}\right)}J(\hat{V},t)\right] \qquad \text{as } t\to\infty, \quad \text{(C.107)}$$

$$J(\hat{V},t) = \int_0^\infty \frac{\sin\left(\frac{\sqrt{3}}{2}U\right)}{U^{\frac{5}{4}}}e^{-\frac{U}{2}}e^{\left(i\hat{V}(Ut)^{\frac{1}{2}}\right)}dU. \quad \text{(C.108)}$$

C.4.3.3 Evaluation of integral J

Starting from (C.108), we complexify the sine and separate it into two integrals, J_1 and J_2, according to (IV.33), but transcribed here for reference,

$$J_1 = \int_0^\infty \frac{\sin\left(\frac{\sqrt{3}}{2}W^2\right)}{W^{\frac{3}{2}}}e^{-\frac{W^2}{2}}\cos(WS)dW, \quad \text{(C.109)}$$

$$J_2 = \int_0^\infty \frac{\sin\left(\frac{\sqrt{3}}{2}W^2\right)}{W^{\frac{3}{2}}}e^{-\frac{W^2}{2}}\sin(WS)dW, \quad \text{(C.110)}$$

where $W=\sqrt{U}$ and $S=\sqrt{\hat{V}^2 t}$. In order to evalute (C.109), it is first differentiated with respect to S, complexified, and broken into two integrals

$$\frac{dJ_1}{dS} = -\frac{(\mathcal{I}_1-\mathcal{I}_2)}{2i}, \quad \text{(C.111)}$$

$$\mathcal{I}_1 = \int_0^\infty \frac{e^{i\left(\frac{\sqrt{3}}{2}W^2\right)}}{W^{\frac{1}{2}}}e^{-\frac{W^2}{2}}\sin(WS)dW, \quad \text{(C.112)}$$

$$\mathcal{I}_2 = \int_0^\infty \frac{e^{-i\left(\frac{\sqrt{3}}{2}W^2\right)}}{W^{\frac{1}{2}}} e^{-\frac{W^2}{2}} \sin(WS) dW. \tag{C.113}$$

From WolframAlpha [42]

$$\mathcal{I}_1 = \frac{\pi S^{\frac{1}{2}} e^{-\frac{S^2}{8A_1}} I_{\frac{1}{4}}\left(\frac{S^2}{8A_1}\right)}{2\sqrt{2A_1}}, \tag{C.114}$$

$$\mathcal{I}_2 = \frac{\pi S^{\frac{1}{2}} e^{-\frac{S^2}{8A_2}} I_{\frac{1}{4}}\left(\frac{S^2}{8A_2}\right)}{2\sqrt{2A_2}}, \tag{C.115}$$

where

$$A_1 = \frac{1}{2} - i\frac{\sqrt{3}}{2}, \qquad A_2 = \frac{1}{2} + i\frac{\sqrt{3}}{2}. \tag{C.116}$$

Therefore,

$$\frac{dJ_1}{dS} = -\frac{\pi S^{\frac{1}{2}}}{4i\sqrt{2}} \left(\frac{e^{-\frac{S^2}{8A_1}} I_{\frac{1}{4}}\left(\frac{S^2}{8A_1}\right)}{\sqrt{A_1}} - \frac{e^{-\frac{S^2}{8A_2}} I_{\frac{1}{4}}\left(\frac{S^2}{8A_2}\right)}{\sqrt{A_2}} \right). \tag{C.117}$$

The solution J_1 can be extracted from (C.117) by integration as

$$J_1 = \int_\infty^S \frac{dJ_1}{dS}\Big|_{S=\Omega} d\Omega. \tag{C.118}$$

Note that, in order to evaluate this integral, the modified Bessel functions of the first kind are replaced with their asymptotic expansions for large arguments given by (IV.34). The resulting integrand is then integrated by parts to yield the asymptotic behavior of J_1 at large S. In order to evaluate (C.110), it is compexified and broken into two integrals

$$J_2 = \frac{J_{2_1} - J_{2_2}}{2i} \tag{C.119}$$

$$J_{2_1} = \int_0^\infty \frac{e^{\left(i\frac{\sqrt{3}}{2}W^2\right)}}{W^{\frac{3}{2}}} e^{-\frac{W^2}{2}} \sin(WS) dW, \tag{C.120}$$

$$J_{2_2} = \int_0^\infty \frac{e^{-\left(i\frac{\sqrt{3}}{2}W^2\right)}}{W^{\frac{3}{2}}} e^{-\frac{W^2}{2}} \sin(WS) dW. \tag{C.121}$$

From WolframAlpha [43],

$$\int_0^\infty \xi^{-\frac{3}{2}} e^{-A\xi^2} \sin(B\xi) d\xi = \frac{\pi B^{\frac{3}{2}} e^{-\frac{B^2}{8A}} \left(I_{-\frac{1}{4}}\left(\frac{B^2}{8A}\right) + I_{\frac{3}{4}}\left(\frac{B^2}{8A}\right)\right)}{2\sqrt{2A}}. \tag{C.122}$$

As before, we write

$$A_1 = \frac{1}{2} - i\frac{\sqrt{3}}{2}, \qquad A_2 = \frac{1}{2} + i\frac{\sqrt{3}}{2}. \tag{C.123}$$

The solutions to (C.120) and (C.121) are

$$J_{2_1} = \frac{\pi S^{\frac{3}{2}} e^{-\frac{S^2}{8A_1}} \left(I_{-\frac{1}{4}}\left(\frac{S^2}{8A_1}\right) + I_{\frac{3}{4}}\left(\frac{S^2}{8A_1}\right)\right)}{2\sqrt{2A_1}}, \tag{C.124}$$

$$J_{2_2} = \frac{\pi S^{\frac{3}{2}} e^{-\frac{S^2}{8A_2}} \left(I_{-\frac{1}{4}}\left(\frac{S^2}{8A_2}\right) + I_{\frac{3}{4}}\left(\frac{S^2}{8A_2}\right)\right)}{2\sqrt{2A_2}}. \tag{C.125}$$

Equations (C.124) and (C.125) are combined in (C.119) to yield

$$J_2 = \frac{\pi S^{\frac{3}{2}}}{4i\sqrt{2}} \left(\frac{e^{-\frac{S^2}{8A_1}} \left(I_{-\frac{1}{4}}\left(\frac{S^2}{8A_1}\right) + I_{\frac{3}{4}}\left(\frac{S^2}{8A_1}\right)\right)}{\sqrt{A_1}} - \frac{e^{-\frac{S^2}{8A_2}} \left(I_{-\frac{1}{4}}\left(\frac{S^2}{8A_2}\right) + I_{\frac{3}{4}}\left(\frac{S^2}{8A_2}\right)\right)}{\sqrt{A_2}} \right). \tag{C.126}$$

C.4.3.4 Cancellation of leading order terms of Bessel expansion in evaluation of J integral

Equations (C.118) and (C.126) are evaluated using just the leading order terms of the Bessel expansion (IV.34) leading to the following result

$$J \sim \frac{2}{\sqrt{2\pi}} \left(C_1 S^{-\frac{3}{2}} + C_2 S^{-\frac{7}{2}} + C_3 S^{-\frac{15}{2}} \right) \text{ as } S \to \infty. \tag{C.127}$$

The solution J is written in terms of the aggregate constants

$$C_1 = \frac{\sqrt{2}}{3} b\mathcal{F}_1 + ib(\mathcal{F}_1 + \mathcal{G}_1), \tag{C.128}$$

$$C_2 = -\frac{2\sqrt{2}}{7} b\mathcal{F}_2 - 2iab(\mathcal{F}_2 + \mathcal{G}_2), \tag{C.129}$$

$$C_3 = -\frac{4\sqrt{2}}{15}(a^3b - ab^3)\mathcal{F}_4 - i(4a^3b - 4ab^3)(\mathcal{F}_4 + \mathcal{G}_4), \tag{C.130}$$

$$a = \frac{1}{2}, \quad b = \frac{\sqrt{3}}{2}, \tag{C.131}$$

where the coefficients $\mathcal{F}_n$ and $\mathcal{G}_n$ are defined recursively as:

$$\mathcal{F}_1 = (\frac{1}{4} - 1), \quad \mathcal{F}_2 = \mathcal{F}_1\frac{(\frac{1}{4} - 9)}{2}, \quad \mathcal{F}_3 = \mathcal{F}_2\frac{(\frac{1}{4} - 25)}{3}, \quad \mathcal{F}_4 = \mathcal{F}_3\frac{(\frac{1}{4} - 49)}{4}, \tag{C.132}$$

$$\mathcal{G}_1 = (\frac{9}{4} - 1), \quad \mathcal{G}_2 = \mathcal{G}_1\frac{(\frac{9}{4} - 9)}{2}, \quad \mathcal{G}_3 = \mathcal{G}_2\frac{(\frac{9}{4} - 25)}{3}, \quad \mathcal{G}_4 = \mathcal{G}_3\frac{(\frac{9}{4} - 49)}{4}. \tag{C.133}$$

As a note, the terms which contained just $\mathcal{F}_3$ and $\mathcal{G}_3$ cancel out exactly. As stated in IV.36,

$$Real\left[e^{-i\frac{\pi}{4}}C_1\right] = Real\left[e^{-i\frac{\pi}{4}}C_2\right] = Real\left[e^{-i\frac{\pi}{4}}C_3\right] = 0. \tag{C.134}$$

Therefore, we can conclude that $Real[e^{-i\frac{\pi}{4}}J] = 0$ if only the leading order terms are considered.

C.4.3.5 Relevant terms of Bessel expansion to evaluate of J integral

Equations (C.118) and (C.126) are evaluated using just the sub-dominant terms of the Bessel expansion (IV.34), and substituted into (IV.33) to yield

$$J \sim \sqrt{2\pi}e^{i\frac{\pi}{4}}\left(\sin\left(\frac{\sqrt{3}}{8}S^2\right) + \sqrt{3}\cos\left(\frac{\sqrt{3}}{8}S^2\right) - i\cos\left(\frac{\sqrt{3}}{8}S^2\right) + i\sqrt{3}\sin\left(\frac{\sqrt{3}}{8}S^2\right)\right)S^{-\frac{3}{2}}e^{-\frac{S^2}{8}} + O\left(S^{-\frac{5}{2}}e^{-\frac{S^2}{8}}\right) \text{ as } S \to \infty, \tag{C.135}$$

where $S = \sqrt{\hat{V}^2 t}$ and $\hat{V} = \sqrt{V_x^2 + V_z^2}$.